The properties of discrete X-ray sources in star-forming galaxies

JACKSON, FLOYD,EMMANUEL

The properties of discrete X-ray sources in star-forming galaxies

Floyd Jackson

A Thesis presented for the degree of
Doctor of Philosophy

X-ray Sub-Group

Extragalactic Astronomy and Cosmology
Department of Physics
University of Durham
United Kingdom

February 2012

Dedicated to

Naveena, who has been a fantastic support and a wonderful friend throughout my time in Durham. Thank you so much.

The properties of discrete X-ray sources in star-forming galaxies

Floyd Jackson

Submitted for the degree of Doctor of Philosophy
February 2012

Abstract

Observations of starburst galaxies have revealed a large number of point-like X-ray sources located within these systems, including active galactic nuclei (AGN), X-ray binaries (XRBs), and utraluminous X-ray sources (ULXs). In this thesis we investigate the physical properties of a variety of these objects using both their X-ray emission characteristics and their optical counterparts, in order to better understand the accretion physics of such objects, and the environments in which they are found.

This work begins with a study of 3 moderate-redshift ($z \sim 0.1$) X-ray bright ($> 10^{42}$ erg s^{-1}) galaxies, all of which display no clear signs of the presence of an AGN in the optical band. Given the high X-ray luminosities of these objects, they must either be the most X-ray luminous starburst galaxies known; or they must harbour a hidden AGN. We use new, pointed observations of the galaxies to determine their detailed X-ray characteristics, and demonstrate that each X-ray source is consistent with an AGN. The most likely explanation for the lack of AGN signatures in the optical spectra of these galaxies is that the AGN emission lines are being diluted by star formation signatures from within the host galaxies.

Next, we present age constraints on 13 bright XRBs located within the high-metallicity drop-through ring galaxy NGC 922. While less than half the X-ray sources are located close to recent star formation as traced by Hα emission, the majority of sources are associated with star clusters, that we are able to age on the basis of their optical colours. We find that the sources that are closest to clusters tend to also have the youngest counterpart clusters and, in most cases, are

close to Hα emission, placing a limit of < 10 Myrs on their age, while those with greater distances to star clusters are also significantly older. We also investigate the possibility that the X-ray sources were ejected from their parent clusters, either by dynamical interactions, or by supernova kicks. An important caveat to the results of this work is that the a number of sources may have associated clusters that are highly extinguished and are therefore undetectable in the optical band.

Finally, we present a study of the 8 brightest X-ray point-sources in the prototypical starburst galaxy M82, using the rich data set afforded to us by a ~ 480 ks *Chandra* observation of the galaxy. From our investigation, we find that the sources with X-ray luminosities $< 10^{39}$ erg s^{-1} are heterogeneous, but all display X-ray properties that are typically observed in canonically accreting back hole binaries. A possible bi-modality is seen in accretion states between the more luminous and less luminous sources in this subset of our sample. The majority of these sources show significant long-term variability, with one of the sources being identified as a transient candidate. The three brightest sources in our sample, all of which are known ULXs, display long-term variability and spectral characteristics consistent with previous observations. This work demonstrates the rich potential for future studies of the diverse X-ray binary populations in nearby galaxies.

Declaration

The work in this thesis is based on research carried out by the author between 2008 and 2012 under the supervision of Dr. Timothy Roberts and Prof. Chris Done in the Department of Physics at the University of Durham. No part of this thesis has been submitted elsewhere for any other degree or qualification at the University of Durham.

Portions of this work have appeared in the following papers:

- Jackson F. E,. Roberts T. P., Alexander D. M., Gelbord J. M., Goulding A. D., Ward M. J., Wardlow J. L., Watson M. G. 2012, MNRAS, in press

Acknowledgements

First of all, I would like to thank my supervisors, Dr. Timothy Roberts and Prof. Christine Done, for their unwavering support and guidance throughout the course of my PhD studies at Durham. I would not be where I am today if it weren't for their constant support.

I also wish to express my gratitude to all my friends, colleagues, and collaborators, who have made this experience so interesting and enjoyable. In particular, I would like to thank Dr. Andrea Prestwich, Dr. Matthew Middleton, Dr. Angese Del-Moro, Prof. Dave Alexander, Andy Sutton, Mari Kolehmainen, and Adam Ingram for the numerous interesting and helpful discussions that we have had on the various aspects of X-ray astronomy. I would also like to thank Dr. Rupali Chandar, Prof. Martin Ward, Blagoy Rangelov, and Stephen Hamer for sharing with me their valuable expertise in optical astronomy. Thanks must go out to my collaborators at the Harvard-Smithsonian CfA and the University of Toledo for giving me the fantastic opportunity of experiencing life as an astronomer in the US.

Finally, I would like to say that I am very grateful for all the support and encouragement that my family have given me throughout my academic career.

Contents

Chapter 1

Introduction

In this thesis, the nature of X-ray emitting point-like sources in active star forming galaxies are investigated. Among these sources are accreting black hole (BH) and neutron star (NS) binary systems, ultraluminous X-ray sources (ULXs), and active galactic nuclei (AGN). This chapter, which will give an overview of the observed physical properties of these accreting systems, as well as those of starburst galaxies, is structured as follows: Section 1.1 will give a summary of the properties of starburst galaxies, including observed morphologies, and sources of optical and X-ray emission. X-ray binaries (XRBs) will be discussed in Section 1.2. The physics of accretion will be discussed in Section 1.3. This section will include an overview of BH binaries (BHBs) and their accretion states, as well as the properties of accreting NSs. Section 1.4 will outline the observed properties of ULXs. A description of the observed properties of AGN, as well as AGN taxonomy and unification, will be presented in Section 1.5. Section 1.6 will give a present a brief description of the optical and X-ray instruments (i.e., instruments on board the *HST*, *Chandra*, and *XMM-Newton* observatories) used in the collection of data used in this thesis. Finally, the aims of this thesis will be outlined in Section 1.7.

1.1 Starburst galaxies

By definition, starburst galaxies are galaxies that have bolometric luminosities dominated by objects formed in ongoing star formation activity (e.g., Moorwood 1996).

These galaxies were first recognised in the mid-1970s due to their notably high infrared (IR) luminosities (Harwit & Pancini 1975; Rieke & Low 1975; Rieke & Lebofsky 1979). An explanation for these high levels of IR emission was first presented by Rieke et al (1980). Using an evolutionary stellar model developed for the stellar population of the starburst galaxies M82 and NGC 253, the authors deduced that the IR luminosity can be explained by the heating of dust by recently formed hot giant stars. This result was subsequently supported by observational evidence indicating that the stellar populations of starburst galaxies are dominated by massive OB stars (e.g., Conti 1991; Aitken et al. 1982), and red supergiants that have evolved from OBA stars (e.g., Oliva et al. 1995).

It has been observed that starburst galaxies are rich in molecular hydrogen, with gas masses of $M_{\rm gas} \sim 2$ – $60 \times 10^9\ M_\odot$ (Moorwood 1996), with more luminous starbursts containing larger amounts of gas (Sanders et al. 1988). Although this is the case, starburst galaxies are recognised for having high $L_{\rm IR}/M_{\rm gas}$ ratios, with values raging from 20 – 200 (Harwit & Pancini 1975; Rieke & Low 1975; Rieke & Lebofsky 1979). These values are too high to be sustainable throughout the lifetimes of starburst host galaxies, implying that the duration of starburst episodes are short lived. The most convincing explanation for the short lifetimes of starbursts is the rate at which molecular gas is consumed during the formation of stars. In starbursts, the process of star formation occurs within giant molecular gas clouds (GMCs); such clouds form either by the coming together of smaller molecular clouds (Kwan 1979; Combes & Gerin 1985), or through magnetic, thermal, or gravitational instabilities (Elmegreen 1990). Scoville & Young (1983) estimated the rate at which stars are formed, and therefore gas depleted, in a starburst episode to be $SFR = 7 \times 10^{-11}(L_{\rm IR}/L_\odot)[M_\odot\ {\rm yr}^{-1}]$. Given the luminosities of starburst galaxies as observed by *IRAS*, this implies that starbursts with moderate $L_{\rm IR}$ values produce stars at a rate of ~ 3 – $30\ M_\odot\ {\rm yr}^{-1}$, and those with very high $L_{\rm IR}$ values produce stars at a rate of $> 1000\ M_\odot\ {\rm yr}^{-1}$. If all of the molecular gas in a starburst is invested in the formation of stars, then the lifetime of the starburst will be $\sim 10^9$ yrs for a moderately IR-bright episode, and $\sim 10^7$ yrs for a very IR-bright episode. These numbers agree with the starburst durations that were predicted by the continuous

star formation models of Leitherer & Heckman (1995).

Starburst galaxies may be recognised in the optical band by nebular emission lines (including those of the Balmer series) in their spectra that indicate the presence of hot young stars (Moorwood 1996). It has been observed in a number of galaxies that a large proportion of the young stellar populations are located within blue clusters that have masses similar to those of globular clusters observed in our Galaxy (e.g., Meurer et al. 1995; Melo et al. 2005). High resolution images taken with *HST* have indicated that the population of these super star clusters (SSC) located within M82 possess masses within the range of 10^4 – 10^6 $M_\odot$, and radii between 3 and 9 pc (Melo et al. 2005). Although many SSCs have been observed in a number of starburst galaxies, optical observations are hindered by the high levels of dust that are typically found within these galaxies, which extinguishes the blue light that is emitted by young stellar populations.

Observations of starbursts in the IR and optical bands have revealed that these phenomena display a number of distinct galaxy-wide morphologies (e.g., Smith 1996; Lester 1995; Wang et al. 1995). These morphologies, as well as the mechanisms that caused them to occur, are discussed below.

1.1.1 Starburst mechanisms and morphologies

The process of star formation occurs during the collapse of giant molecular clouds (GMCs) due to either gravitational perturbation or wind pressure from existing stellar clusters (e.g., Elmegreen 1994a). In the case of a starburst episode, high concentrations of GMCs are necessary to convert gas efficiently into stars. Generally, the highest levels of star formation in starburst galaxies are located in the central $\sim$ kpc of the host galaxy (Smith 1996; Lester 1995; Wang et al. 1995), thus implying that the highest concentration of GMCs must be found in these regions. A number of mechanisms have been recognised to transport gas from the outer parts of host galaxies to the centre. Among these mechanisms is the funnelling of gas from the outer parts of the galaxy to the central region by stellar bars in the galactic disc (Athanassoula 1992, 1994). In this scenario, if a Lindblad Resonance (LR) exists within the host galaxy, the gas being funnelled by the stellar bars will be halted by

Figure 1.1: A optical image of NGC 1365 taken using the 8.2 m *VLT* telescope in February 1999. This galaxy is an example of barred ring starburst galaxy (e.g., Phillips et al. 1983). The bars in this galaxy extend to 12 kpc from the galactic nucleus, and funnel gas from the outer regions of the galaxy to a 1.3 kpc diameter ring where an LR is located. Image credited to ESO FORS team. Taken from `http://apod.nasa.gov/apod/`.

the LR and will form a ring at this location. If 2 LRs (i.e., an inner and an outer LR) exist, then the gas being funnelled by the bars will be confined between them (Combes 1991; Telesco 1993). Several starburst ring galaxies have been detected in a number of bands, an example of which can be seen in Figure 1.1. Rings in starburst galaxies also form as a result of drop-through galaxy collisions. This topic will be discussed in a later chapter.

If gas being transported by bars from the outer regions of a galaxy is not halted by the presence of LRs, a disc is expected to form within the central $\sim$ kpc galactic region. The gas in this disc, which may contain a large fraction of the dynamical mass of the galaxy, may collapse further, thus causing an episode of star formation to occur (Shlosman et al. 1990). A significant number of starburst galaxies that do not host LRs have been detected, and thus display nuclear star formation activity.

Figure 1.2: An optical image of IC 342, taken with the Mayall 4 m telescope in late 2006. This nuclear starburst shows evidence of star formation in the central $\sim$ 100 pc region of the galaxy (e.g., Telesco et al. 1993). Image credited to T.A. Rector/University of Alaska Anchorage, H. Schweiker/WIYN and NOAO/AURA/NSF. Taken from `http://www.noao.edu`.

One such starburst galaxy can be seen in Figure 1.2. However, it is possible that a number of galaxies that display apparent nuclear star formation activity may actually have star forming rings that are undetectably small (Moorwood 1996).

In the case of both nuclear and ring starbursts, it is assumed that the stellar bars in the galactic discs are formed either by tidal interactions between galaxies, or by self-gravity within the galactic disc itself (Combes & Elmegreen 1993; Gerin et al. 1990). However stellar bars may also form through tidal forces acting on galactic discs as a result of galaxy mergers (Barnes & Hernquist 1991). Galaxy mergers are expected to produce the most luminous starburst episodes, since the merging causes the gas to become largely concentrated within the central galactic regions (Barnes & Hernquist 1992). As with ring and nuclear starburst galaxies, many galaxy mergers have been observed in multiple bands. An example of a merging starburst galactic system can be seen in Figure 1.3.

Figure 1.3: An optical image of NGC 3256, taken with the *HST*. This galaxy system is an example of 2 merging galaxies resulting in a bright starburst. The star formation within this system is confined to a $\sim$ 4 kpc region close to the centre, but is seen to peak within the nuclei of both galaxies (Kotilainen et al. 1996; Moorwood & Oliva 1994a). Image credited to NASA, ESA, the Hubble Heritage Team (STScI/AURA)-ESA/Hubble Collaboration and A. Evans (University of Virginia, Charlottesville/NRAO/Stony Brook University). Taken from `http://www.spacetelescope.org/`.

1.1.2 The X-ray emission from starburst galaxies

Although starburst galaxies display a peak in luminosity in the far IR band (Rodriguez-Pascual et al. 1993), they also emit a considerable amount of radiation in the form of X-rays, with the most luminous local star forming galaxies displaying X-ray luminosities of the order $\sim 10^{42}$ erg s^{-1} (e.g., Moran et al. 1999; Ptak et al. 2003). X-ray observations have revealed that the emission from starburst galaxies is caused by a number of physical mechanisms, many of which are the direct (or indirect) result of supernova (SN) explosions. If the SN rate within a galaxy is high enough (> 0.1 yr^{-1}), the interaction of hot material from SNe with ambient ISM will cause the formation of a 'superbubble' within the galactic disc. This superbubble will eventually break through the disc and form a high velocity outflow of material from the galaxy known as a 'superwind' (Tomisaka & Ikeuchi 1988; Heckman, Aramus, & Miley 1990). Diffuse wind-related X-ray emission has been detected in a number of galaxies, including M82 (Fabbiano 1988; Strickland & Heckman 2009), NGC 3628 (Fabbiano et al. 1990), and NGC 253 (Pietsch 1993). Figure 1.4 shows a Hα image of NGC 253 overlaid with 0.1 – 2 keV *ROSAT* HRI contours. The Hα emission traces the material being blown away from the galactic disc by the superwind. The figure shows an obvious correlation between X-ray contours and the Hα emission, indicative of a relationship between the soft X-ray emission and the superwind.

In a study of the central regions of the prototypical starburst galaxy M82, Read & Stevens (2002) reported the spectrum of the wind-related diffuse X-ray emission to be comprised of a complex array of lines over a large range of temperatures, which could be best fitted with a multi-temperature (0.2 – 1.6 keV) plasma model. The high resolution emission line spectrum used in this analysis can be seen in Figure 1.5. A similar multi-temperature plasma model was found to best fit the spectrum of the wind-related diffuse emission from the star forming galaxies NGC 3256 and NGC 3310 (Jenkins et al. 2004). They suggest that the hottest diffuse emission arises from SN-heated plasma, while the colder emission is arising as a result of the interaction between outflowing winds and ambient ISM. Similar multi-temperature plasma models have been found to best fit the spectra of diffuse emission in star forming galaxies that are not experiencing superwinds, such as the emission from

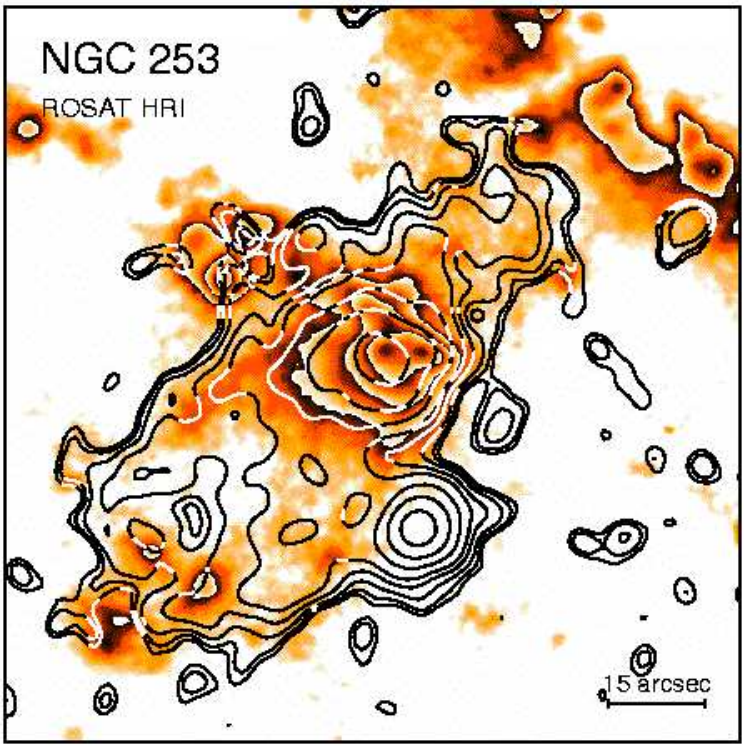

Figure 1.4: A Hα image of the starburst galaxy NGC 253 overlaid with 0.1 – 2 keV *ROSAT* HRI. Image credited to Max-Planck-Institut für Extraterrestrische Physik. Taken from `http://www.mpe.mpg.de`.

the galaxies M101 (Warwick et al. 2007), and the 6 late-type star forming spiral galaxies investigated by Owen & Warwick (2009).

As well as the detection of diffuse X-ray emission, X-ray point sources are seen to be present within starburst galaxies (e.g. Fabbiano & White 2006). Among these point sources are SNR, which are observed in the hard X-ray band as a result of inverse-Compton scattering of far-IR photons by relativistic electrons produced in SNe.

Another indirect product of SNe provides a significant fraction of hard X-ray emission seen in starburst galaxies, in the form of massive X-ray binaries (XRBs) (e.g., Fabbiano & White 2006). Figure 1.6 shows a *VLT* optical and *Chandra* 3-colour image of the starburst galaxy M83. A large number of point-like X-ray sources in this image have been identified through spectral and timing analysis as XRBs, with the majority though to be HMXBs (Soria & Wu 2003). The remaining sources have been identified as either background AGN or SN remnants.

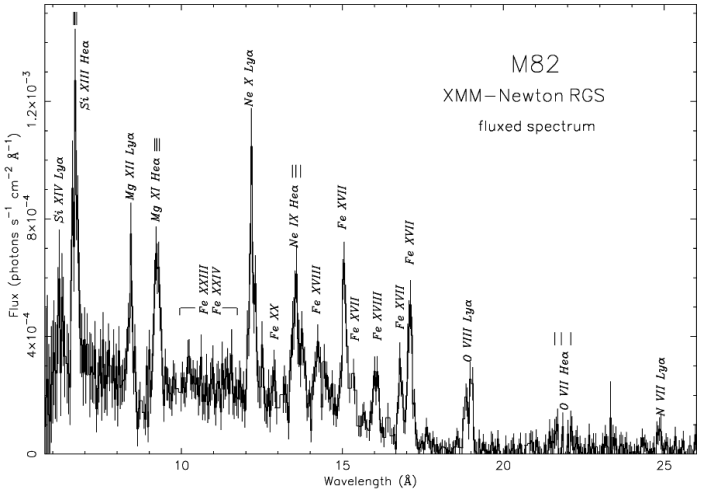

Figure 1.5: The high resolution *XMM-Newton* RGS spectrum of the prototypical starburst galaxy M82. The spectrum is comprised of emission lines from abundant low-Z elements, the Fe-L series, and the OIII line complex. Taken from Read & Stevens (2002).

Figure 1.6: *Upper:* An optical image of the starburst galaxy M83, taken using the *VLT* telescope. Image credited to *ESO* FORS team. *Lower:* An *Chandra* X-ray 3-colour image of the same galaxy, taken from Soria & Wu (2003). The X-ray point sources that were analysed in this work are clearly visible in this image. $\sim 1/2$ the detected point sources were identified as XRBs by their spectral and temporal properties. Taken from `http://www.mpa-garching.mpg.de/`.

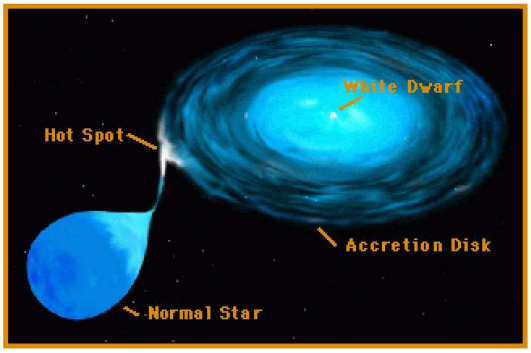

Figure 1.7: An artist's impression of a CV XRB system. As with LMXB and HMXB systems, it is the angular momentum of the matter being accreted by the white dwarf from the stellar companion that causes the formation of the accretion disc. Taken from `http://imagine.gsfc.nasa.gov`.

1.2 X-ray binaries

XRBs are orbiting binary systems comprised of a compact stellar object and a companion donor star. First reported by Giacconi et al. (1962), the physical properties of these sources offer unique insight into the evolution of post main-sequence stars. It is X-ray emission, which is the result of mass being accreted from the companion star by the compact object, that gives astronomers the means of probing the physical properties of these sources. XRBs fall into 3 categories: Cataclysmic variables (CVs), high mass XRBs (HMXBs), and low mass XRBs (LMXBs). In the case of CVs, the compact object is a white dwarf star (Figure 1.7). The compact object in the latter 2 systems is either a NS or BH. In the following sections, focus will be given to the accretion mechanisms that power HMXB and LMXB systems.

1.2.1 HMXBs

By definition, a HMXB system is an XRB system with a companion star of mass $\geq 10M_{\odot}$. Because such massive stars have short lifetimes due to the rapid consumption of fuel within the star, the lifetime of a typical HMXB is of the order 10^5 – 10^7 years (Tauris & van den Heuvel 2006) and they are therefore associated with starburst galaxies. There are $\sim$ 130 known HMXBs in the Galaxy (Liu, van Paradijs, & van den Heuvel 2000), most of which are located in the Galactic plane (Grimm et

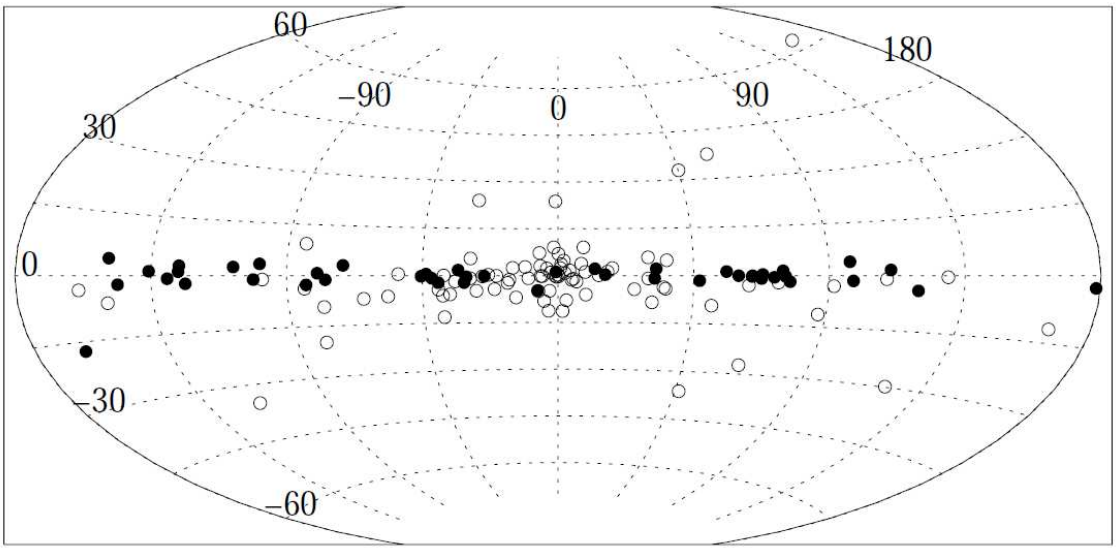

Figure 1.8: The distribution of HMXBs (filled circles) and LMXBs (open circles) in our Galaxy. Taken from Grimm et al. (2002).

al. 2002; c.f., Figure 1.8). The orbital separations of these accreting systems are typically wide, and therefore lead to long orbital periods ($\gtrsim$ 187 days, van Paradijs & McClintock 1995).

In HMXBs, the compact object typically accretes mass via Bondi-Hoyle accretion (Hoyle & Lyttleton 1941; Bondi 1952; Mestel 1954), when passing through material that is being ejected from the massive companion star via a strong stellar wind. In this scenario, only a small fraction of the material in the wind is affected by the compact object. The affected material forms a cylinder with a critical radius $r_{crit} = 2GM/v_w^2$, where G is Newton's gravitational constant, M is the mass of the compact object, and v_w is the velocity of the wind (see Figure 1.9). The material outside this radius is not accreted, but instead is perturbed into what is known as an accretion wake. Once the material in the cylinder comes close to the compact object, conservation of its angular momentum will likely cause it to form an accretion flow around the compact object.

1.2.2 LMXBs

If a compact stellar object is accreting material from a star with mass $\leq 1\ M_\odot$, resulting in the emission of X-rays, then the system is defined as a LMXB (van

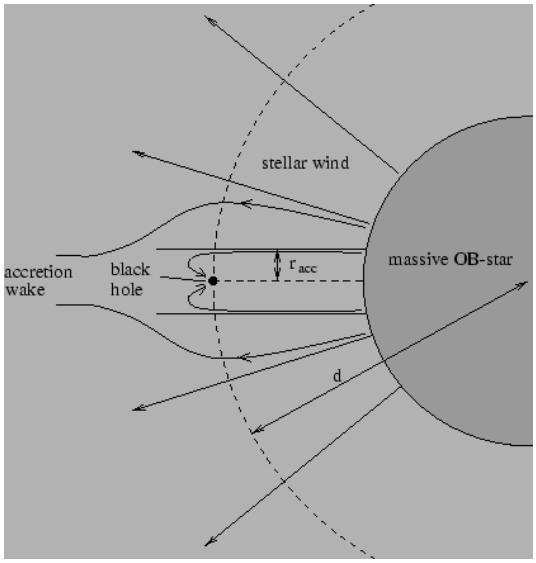

Figure 1.9: A cartoon of wind-fed accretion from a massive (OB) star onto a compact object. Taken from `tt.astro.su.se`

Paradijs & McClintock 1995). Such systems have lifetimes that range from 10^7 – 10^9 years (Tauris & van den Heuvel 2006; Psaltis 2006). Like HMXBs, many LMXBs have been detected in the Galaxy, with the highest concentration of these binary systems located in the Galactic bulge (Grimm et al. 2002; c.f., Figure 1.8). Significantly shorter orbital periods have been observed in these systems compared to those observed in HMXBs (0.19 – 389 hrs, van Paradijs & McClintock 1995).

Because the companion stars in LMXBs are not massive enough to produce strong stellar winds like those in HMXBs, Bondi-Hoyle accretion is not possible. Instead, accretion occurs if the compact object and the companion star are within close enough proximity to cause the surface of the star to expand and fill its Roche-lobe (e.g., Psaltis 2006). When this occurs, material from the star flows from the inner Lagrange point towards the compact object in the form of a stream. Due to the conservation of angular momentum of this material, an orbital accretion flow will form around the compact object. Figure 1.10 shows a cartoon of a LMXB accreting matter via Roche-lobe overflow.

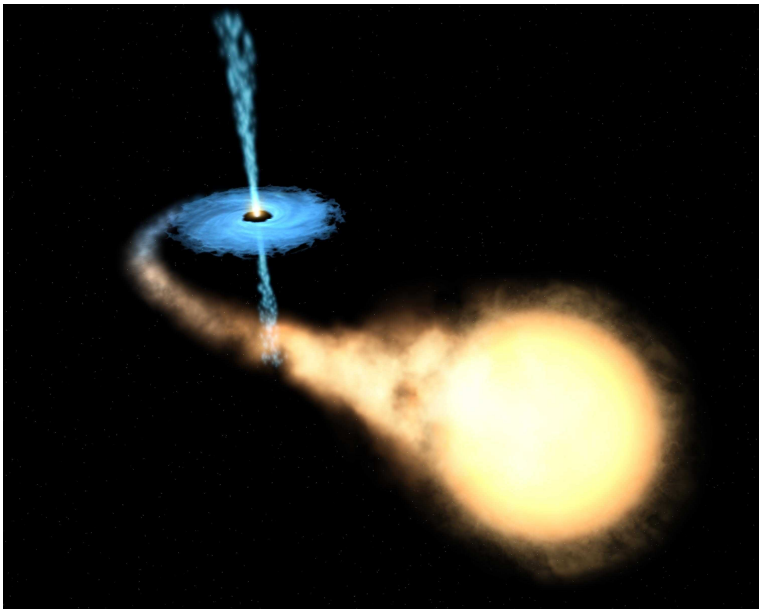

Figure 1.10: An artist's impression of a LMXB undergoing Roche-lobe overflow. Taken from `en.wikipedia.org`.

1.2.3 X-ray binary populations in starburst galaxies

The study of XRB populations in active star forming galaxies is one of great importance, since it should lead to a better understanding of the connection between XRBs and the galactic environments which they inhabit. To this end, a number of stellar population synthesis models have been developed (e.g., Belczynski et al. 2004), spurred by observational evidence that intense star forming galaxies have large populations of HMXBs (including many ULXs) that induce flatter slopes in their X-ray luminosity function (XLF). An example of this is seen in the Antennae galaxy, where a number of ULXs have been detected (Fabbiano, Zezas, & Murray 2001). Figure 1.11 is the *Chandra* image of the Antennae galaxy taken from Fabbiano et al. (2004), in which the bright X-ray point source population is clearly visible. A study of the XLF of the Antennae galaxy conducted by Zezas et al. (2007) yielded a slope of ~ 0.5, after averaging slope values from 7 *Chandra* observations of the galaxy. An example of an XLFs that was used in this calculation is shown in Figure 1.12.

An important result, that has encouraged further investigation of XRB populations in active starburst galaxies, was reported by Grimm, Gilfanov, & Sunyaev

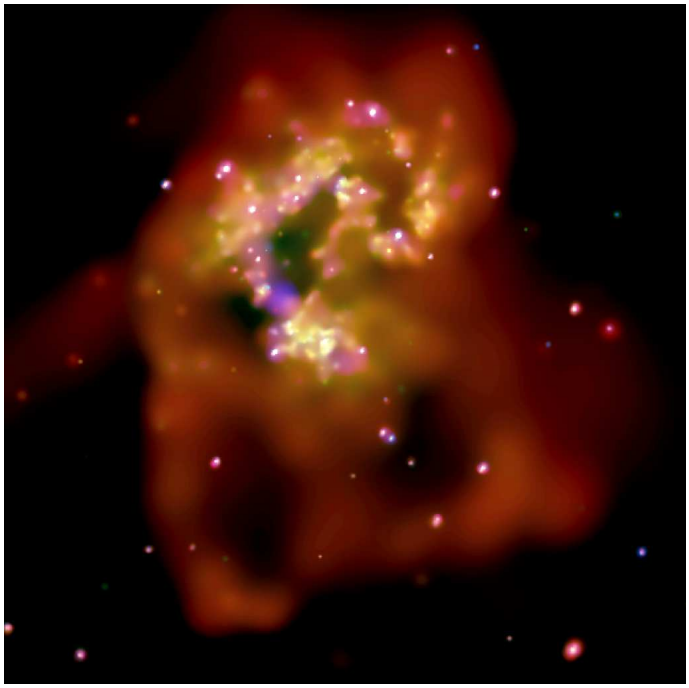

Figure 1.11: A smoothed red (0.3 – 0.65 keV), green (0.65 – 1.5 keV), and blue (1.5 – 6 keV) image of the Antennae galaxy, created using composite data from 7 *Chandra* ACIS observations of the galaxy taken between December 1999 and July 2002. Taken from Fabbiano et al. (2004).

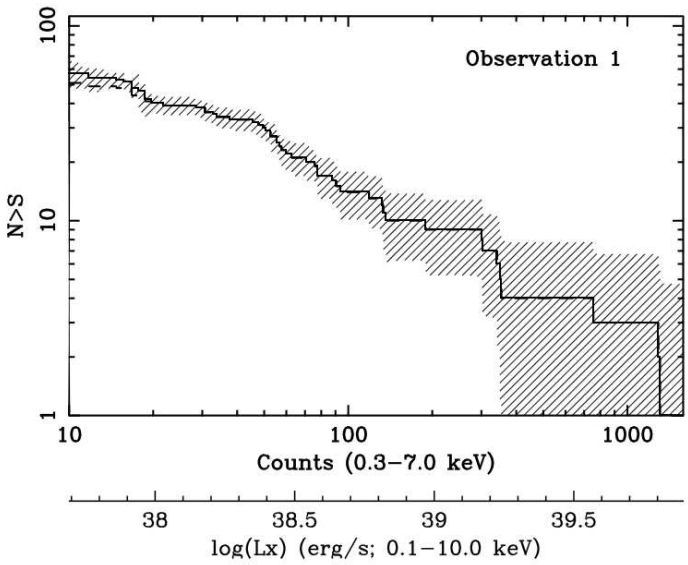

Figure 1.12: One of the XLFs used by Zezas et al. (2007) to calculate the averaged XLF slope of the point-like X-ray source population in the Antennae galaxy. The solid line represents the luminosity function while the hatched region represents the 1σ uncertainty of the function. The upper and lower x-axes indicate 0.3 – 7 keV photon counts and corresponding luminosity, assuming a best fitting absorbed power-law model with a photon index of $\Gamma = 1.7$, and a column density of $N_{\rm H} = 3.24 \times 10^{20}$ cm^{-2}, respectively. The slope of this particular XLF is $0.43^{+0.09}_{-0.15}$. Taken from Zezas et al. (2007).

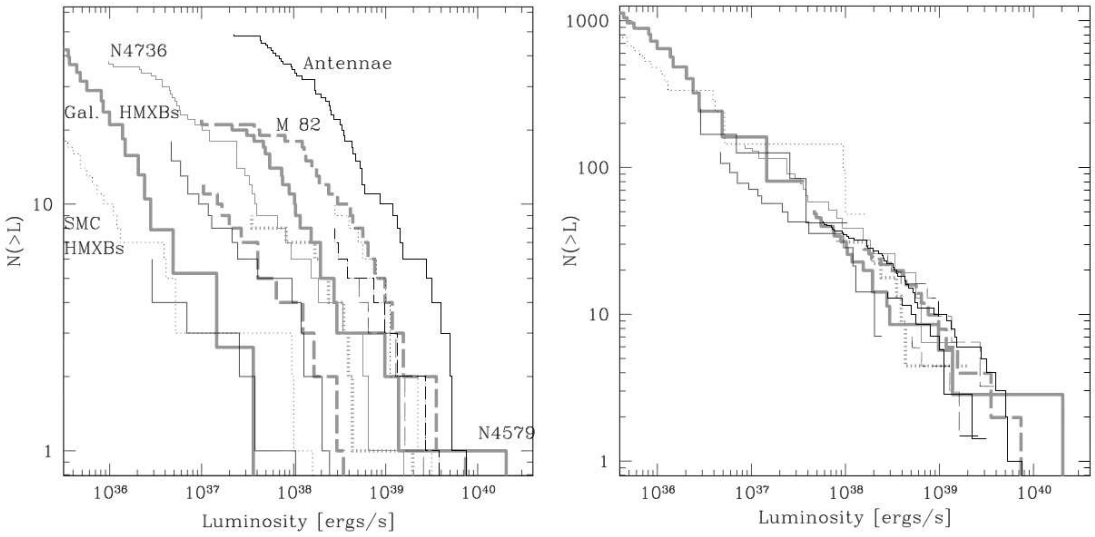

Figure 1.13: *Left:* The XLF of compact X-ray sources in a number of nearby active star forming galaxies. *Right:* The same luminosity functions, scaled by the ratio of SFR to that of the Antennae galaxy. Taken from Grimm, Gilfanov, & Sunyaev (2003).

(2003). The authors found that the XLF slopes of a relatively large sample of starburst galaxies had the same value (~ 0.6), within the errors, and that the luminosity functions themselves scaled with SFR (see Figure 1.13). This result lead the authors to suggest that a universal HMXB XLF exists between galaxies with high SFRs, with a slope of ~ 0.6 and a cut-off luminosity of a few $\times\ 10^{40}$ erg s^{-1}. On the other hand, observations have indicated that older populations of X-ray point sources have a considerably steeper XLF slopes (e.g., Kim & Fabbiano 2003; Kim & Fabbiano 2004; Colbert et al. 2004). This is consistent with populations losing HMXBs at older ages, thus resulting in the domination of the XLFs by LMXBs (e.g., Kim & Fabbiano 2004).

1.3 Accretion physics and phenomenology of XRBs

1.3.1 Accretion flows

The formation of an accretion flow in XRBs occurs if the matter being accreted from the companion star has enough specific angular momentum J to prevent it from falling directly into the compact object. Initially, the accreted matter orbits

the compact object at a radius of $R = J^2/GM$, where M is the mass of the compact object, thus forming a ring. The accretion disc is then formed when the angular momentum in the ring of matter is dissipated outwards, likely by viscous stresses (Balbus 2005).

It has been recognised that there are 2 forms of accretion flow, namely the geometrically thin, optically thick Shakura-Sunyaev disc (Shakura & Sunyaev 1973), and the optically thin, geometrically thick accretion flow (e.g., Narayan & Yi 1995). In the case of the geometrically thin disc, it is the transportation of angular momentum outward from the centre of the accretion disc that ultimately allows the matter within the disc to be accreted by the central compact object. Viscous stresses cause the dissipation of angular momentum in the disc to convert gravitational potential into thermal energy (Balbus 2005). This means that at a given radius r ($= R/R_{\rm G}$, where $R_{\rm G}$ is the gravitational radius of the compact object, GM/c^2), the disc emits thermal radiation in the form of a quasi-blackbody, with a temperature $T_R \approx r^{-3/4}$. The spectrum of the disc as a whole is comprised of a number of different spectra for different disc radii, and is thus known as the multi-coloured (or multi-temperature) disc blackbody spectrum.

An optically thin, geometrically thick accretion flow may form if mass is being accreted below a certain critical rate. In this case, the inflowing matter may not be dense enough for thermalisation of electrons with protons to occur. This will lead to the formation of a 2-temperature electron-proton plasma. Since protons have more mass then electrons, they gain most of the gravitational potential energy in the flow. Because protons are inefficient radiators, most of the gravitational potential energy in the flow is advected towards the BH (e.g., Narayan & Yi 1995). Such a flow has been named an advection-dominated accretion flow (ADAF, Narayan & Yi 1995). A very small amount of energy is transferred from the protons to the electrons via Coulomb collisions. Since electrons are efficient radiators (Sharpio, Lightman, & Eardley 1976; Ichimaru 1977; Narayan & Yi 1995), this energy is radiated in the form of inverse-Comptonisation, bremsstrahlung, and/or cyclo-synchrotron emission.

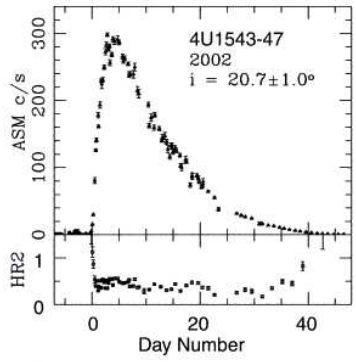

Figure 1.14: The lightcurve of the BHB 4U1542-47, a transient BHB displaying a typical FRED lightcurve profile. Taken from Narayan & McClintock (2004).

1.3.2 BHBs

BHBs are accreting XRBs in which the compact object is a BH. BHs have been identified as the compact object in both LMXB and HMXB systems (e.g., McClintock & Remillard 2006; Psaltis 2006). Observations have indicated that there are 2 classes of BHBs: persistent HMXBs and transient LMXBs. The behaviours in X-ray emission from both class of object are a result of the accretion processes which power the sources, that lead to very different behaviours in X-ray variability. While persistent BHBs display variability in photon counts of several factors of 2 over time periods ranging from milliseconds to months (Psaltis 2006), transient sources can experience extended periods of time (months to decades) with very little X-ray activity, separated by short outbursts with increases in flux by up to several orders of magnitude (Bradt et al. 2000). The lightcurve of 4U1542-47 can be seen in Figure 1.14. This source is a typical BHB transient, and displays a classic fast-rise-exponential-decay (FRED) lightcurve profile.

The most prevalent model that explains the behaviour of transient BHBs (and NS, see below) is one that is based on the instability of Shakura-Sunyaev accretion discs as a result of hydrogen ionisation (e.g., Lasota 2001). In this model, the fast rise in X-ray emission is initially caused by a rapid increase in mass accretion by the BH due to thermal and viscous instabilities in the accretion disc. This occurs when a cool quiescent disc steadily accretes mass from the binary companion star until, at a certain radius, the disc becomes hot enough for hydrogen ionisation to

occur (i.e., $\sim 10^4$ – 10^5 K). At this temperature, the opacity of the material at this radius increases rapidly, and thus all irradiating photons are retained within the disc. This causes the temperature of the hydrogen to increase further, eventually causing the remaining hydrogen to ionise. The increase in temperature causes the mass accretion rate at this radius to increase, which in turn causes the mass accretion at the next radius within the disc to increase. The increase in mass accretion at the new radius causes a thermal instability similar to what was seen at the original radius. This process causes a heat wave to propagate through the disc, causing the accretion rate, and hence the luminosity, of the entire disc to increase (Lasota 2001; Kato, Fukue, & Mineshige 1998). The subsequent exponential decay of luminosity is caused by the accretion disc being consumed by the BH at a rate that is faster than the build-up of material in the disc. That is, as the BH consumes the disc, both the temperature and mass accretion rate decreases.

1.3.3 BHB accretion states

For the last ~ 4 decades, Galactic BHBs have been know to display certain spectral and temporal characteristics (e.g., Tananbaum et al. 1972; van der Klis 1994; Tanaka & Lewin 1995; Tanaka & Shibasaki 1996; McClintock & Remillard 2006). These characteristics manifest themselves in 5 distinct observationally-defined accretion states: the quiescent state, the hard state, the thermal dominant (TD) state, the steep power-law (SPL) state, and the intermediate (IM) state (see Figure 1.15). The spectral and timing properties of each state depend on the accretion rate of the system, which in turn depends on the extension/truncation of the accretion disc to/from the innermost stable circular orbit (ISCO) of the BH. Below is a description of the spectral, temporal, and geometric properties of each of the 5 accretion states.

The Quiescent State

A Galactic BHB in the quiescent state displays a very low X-ray luminosity of $\sim 10^{30.5-33}$ erg s^{-1}, and a power-law spectrum with a best fitting photon index of ~ 1.7 – 2.1 (McClintock & Remillard 2006). Both the hard spectral shape and low luminosity of such a source can be explained by a highly truncated accretion disc

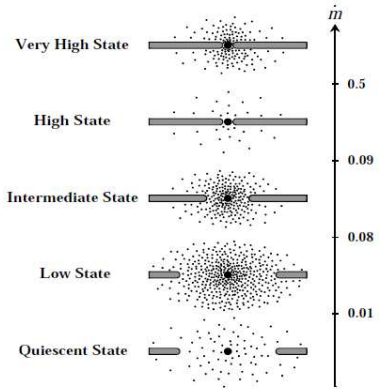

Figure 1.15: A schematic of accretion flow geometry in the 5 spectral states as a function of mass accretion rate. The dots represent the ADAF, and the horizontal bars represent the thin disc. Note that the names of the accretion states in the diagram are taken from Esin et al. (1997), and are therefore not all the same as those that have been adopted in this thesis (i.e., those used by McClintock & Remillard 2006). The regions labelled the 'Low State', 'High State', and 'Very High State' correspond to what McClintock & Remillard (2006) define as the hard state, TD state, and SPL state, respectively. The 'Quiescent State' and 'Intermediate State' are labelled similarly in both the diagram and in McClintock & Remillard (2006). Taken from McClintock & Remillard (2006).

(e.g., Esin et al. 2001), and an interior region between the disc and the ISCO of the BH filled with a hot ($T_e \sim 100$ keV) ADAF (Narayan & Yi 1994, 1995; Narayan et al. 1996; Quataert & Narayan 1999). The lowest panel in Figure 1.15 shows the accretion flow geometry of a BHB in the quiescent state. The majority of emission in these systems originates from the non-thermal ADAF, thus implying the hard spectrum (Narayan et al. 1996, 1997; Hameury et al. 1997; Garcia et al. 2001). The radiative efficiency of an ADAF is very low (~ 0.1 – 1%, e.g., Narayan et al. 1997), which accounts for the low luminosity of quiescent BHBs.

The Hard State

Like the quiescent state, the spectrum of the hard state is best fit with a hard ($\Gamma \sim 1.7$) power-law model (McClintock & Remillard 2006). The addition of a cool ($kT_{\rm in} \sim 0.1$ – 0.2 keV) disc component has been reported in a number of hard spectra (Wilms et al. 1999; Takahashi et al. 2001), thus indicating the presence of a cool, truncated ($\geq 100\ R_{\rm S}$), accretion disc. However, this disc only contributes $\leq 20\%$ of

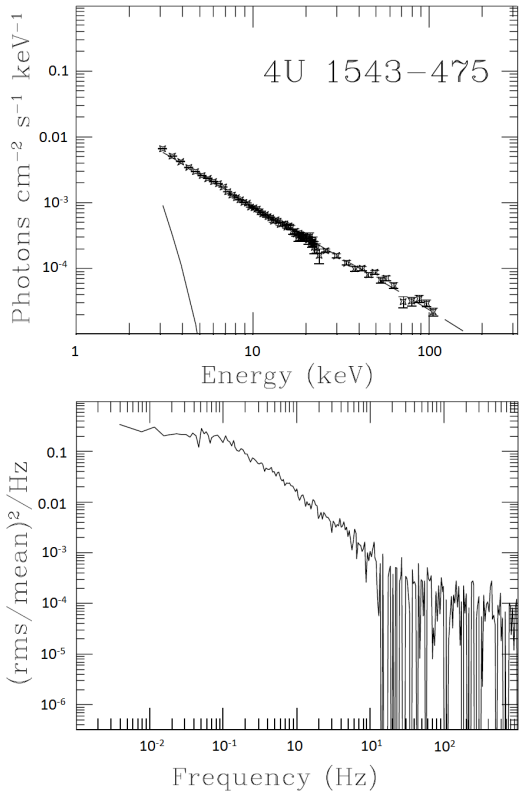

Figure 1.16: *Top:* A spectrum of the BHB 4U 1543-475 in the hard state. A relatively flat power-law component, which is represented by the dashed line, dominates the spectrum of the source above 1 keV. *Bottom:* The PDS of 4U 1543-475 in the same accretion state. This PDS clearly shows the elevated power that is typically displayed by sources in the hard state. Both images were taken from McClintock & Remillard (2006).

the overall 2 – 20 keV X-ray flux. An example of a hard state spectrum of the BHB 4U 1543-475 can be seen in the top panel of Figure 1.16. To this day, the source of the majority of emission is a matter of debate. One physical interpretation is that the accretion flow is an ADAF, similar to that seen in the quiescent state (Narayan & Yi 1995; Done, Gierlinski, & Kubota 2007). The geometry of this interpretation can be seen in the region of Figure 1.15 labelled 'Low State'. An alternative interpretation is that the disc at lower radii is entrained within a jet (e.g., Markoff et al. 2001). Indeed, the presence of a radio jet appears an ubiquitous trait of the hard state (see Fender 2006 for a review of this topic).

As well as a predominantly hard energy spectrum, the hard state displays a significant level of short term variability. The 0.1 – 10 Hz power density spectrum

(PDS) of a BHB in the hard state is seen to have an integrated continuum in the typical range of $0.1 < r < 0.3$ (McClintock & Remillard 2006). A hard state PDS of the BHB 4U 1543-475 can be seen in the bottom panel of Figure 1.16.

The Thermal Dominant State

The TD state is dominated by emission from the optically thick, geometrically thin Shakura-Sunyaev accretion disc (McClintock & Remillard 2006; Done, Gierlinski, & Kubota 2007). It has been observed that BHBs in this state display an inner disc temperature of $kT_{\rm in} \sim 0.7$ – 1.5 keV, and very little, if any, short-term temporal variability (integrated PDS of ≤ 0.06, root mean squared (rms) fractional variation of $\leq 1\%$ between 0.1 – 10 Hz, McClintock & Remillard 2006). Very little non-thermal emission has been observed in BHBs in the TD state, with a maximum of $\leq 25\%$ in the 2 – 20 keV band. This emission is the result of magnetic reconnection within a thin corona sitting above the accretion disc (Done 2002). The spectrum of this emission is best fit with a power-law model with a photon index of $\Gamma \sim 2.1$ – 4.8. The geometry of the accretion disc plus corona can be seen in the region of Figure 1.15 labelled 'High State'. An enery spectrum and PDS of the BHB 4U 1543-475 can be seen in the top and bottom panel of Figure 1.17.

The Steep Power-Law State

The SPL state has been reported as the brightest accretion state in a number of BHBs (e.g., Miyamoto & Kitamoto 1991; Miyamoto et al. 1993). The emission from this state is a combination of a thermal and non-thermal component, with the non-thermal component contributing ~ 40 – 90 % of flux in the 2 – 20 keV band. The spectrum of the SPL is best fit with a power-law model of photon index ≥ 2.4 (McClintock & Remillard 2006). A spectrum of the BHB 4U 1543-475 accreting in the SPL state is shown in Figure 1.18. Geometrically, the SPL state consists of an accretion disc covered by a corona of Comptonising material (e.g., Gierlinski et al. 1999; Zdziarski et al. 2001), and can be seen in the region of Figure 1.15 labelled 'Very High State'.

The SPL state is seen to display a very high level of short-term temporal vari-

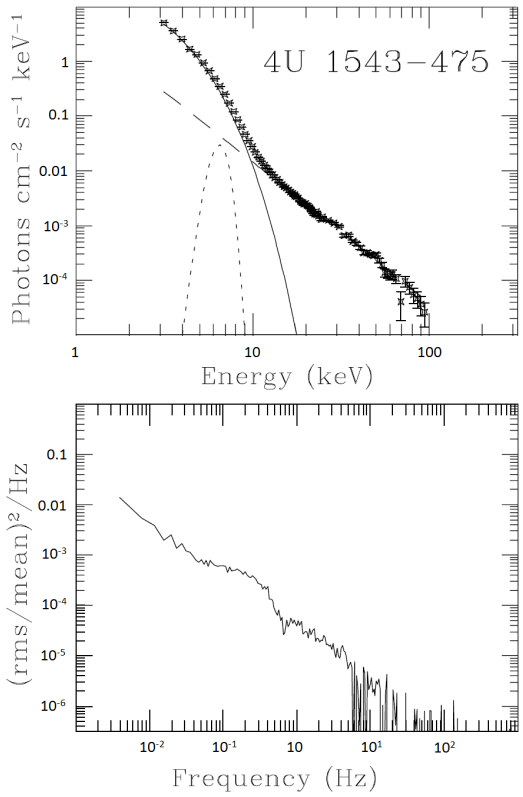

Figure 1.17: *Left:* An energy spectrum of the BHB 4U 1543-475 accreting in the TD state. This spectrum is dominated by a disc component below 10 keV, which is represented by the solid line. A faint power-law component, which is represented by the dashed line, is also present in the spectral model. The dotted curve represents an Fe line component. *Right:* The corresponding PDS of the sources accreting in the same state. As is typical for sources accreting in the TD state, very little power is observed in this sources. Both images were taken from McClintock & Remillard (2006).

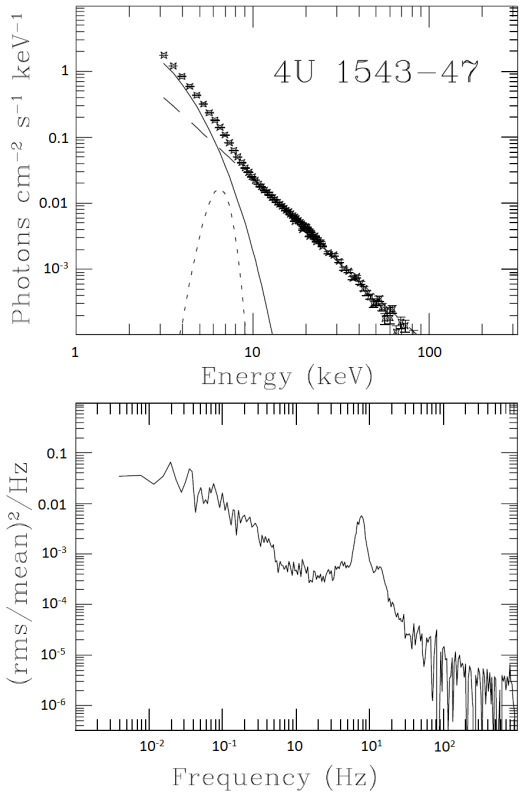

Figure 1.18: *Top:* A spectrum of the BHB 4U 1543-475 accreting in the SPL state, which is characterised by a steep power-law component. *Bottom* The PDS of the same source accreting in the SPL state. A QPO is clearly visible in the PDS. Both images taken from McClintock & Remillard (2006).

ability, depending on the contribution of 2 – 20 keV flux from the non-thermal component. If the flux is mostly thermal (i.e., 50 – 80%), quasi-periodic oscillations (QPOs) are detected in both low (0.1 – 30 Hz) and high (40 – 450 Hz) frequency bands, whereas if the flux is mostly non-thermal (> 50%), no QPOs are detected (McClintock & Remillard 2006).

Like the hard state, observations have indicated a correlation between the SPL state and the presence of radio jets (e.g., Hannikainen et al. 2001). Unlike the hard state, these jets are seen to be explosive and non-persistent. Note, however, that there have also been observations of BHBs accreting in this state where the presence of a radio jet was not detected (e.g., Tomsick et al. 1999).

The Intermediate States

The majority of observed Galactic BHBs can be explained by the 4 accretion states outlined above. However, some BHBs have been seen to exhibit spectral and/or timing properties from both hard and TD states, such as simultaneous band-limited PDS noise and soft disc emission (e.g., Mendez & van der Klis 1997). It has been suggested that such a BHB is accreting in an intermediate state between the hard and TD states. Other observations have indicated that BHBs accrete in a state indicative of a transition between hard and SPL accretion (McClintock & Remillard 2006). Such hybrids of accretion states have been interpreted as IM states, although it has been recognised that it is important to specify which of the 4 accretion states can be combined to exhibit observed X-ray properties (McClintock & Remillard 2006).

1.3.4 An alternative definition for accretion states

In the previous section, we described the quantitative characteristics of the accretion states of BHBs as defined by McClintock & Remillard (2006). An alternative definition for accretion states has been developed, one that is based on the model presented by Fender et al. (2004). This model describes the coupling of accretion discs and radio jets in BHBs. A hardness-intensity diagram (HID) representing this

model is shown in Figure 1.19. In this diagram, X-ray hardness[1] increases from left to right, and intensity from bottom to top. The track in the upper panel of the figure represents the hardness and intensity of a sample of 9 sources observed by *RXTE* as they evolve through the hard (LS in the diagram), SPL/IM (VHS/IS), and TD (HS) states. The dashed lines represent the borders between the states, and the solid line represents the line which defines the hardness at which a jet is no longer observed. In this scenario, the SPL and IM states is recognised as the same state, and has subsequently been divided into the hard intermediate and soft intermediate state (Belloni et al. 2005). The solid arrows represent the spectral evolution of a typical BHB transient. The bottom panel shows how inner disc radius and Lorentz factor of a BHB jet varies with hardness. In a transient source, a steady radio jet with a Lorentz factor of < 2 is observed in the hard and hard intermediate states. As the luminosity of the source increases, the accretion state transits from the hard state, through the hard intermediate state, and eventually reaches a peak intensity in the soft intermediate state. At this point, the Lorentz factor increases rapidly and produces a shock in the outflow, after which the jet is no longer produced, and the transient has evolved into the TD state. Fender et al. (2004) observed that a number of sources did not complete the full evolutionary cycle described above, but instead harden repeatedly, thus tracing the 'loop' and track that can be seen in the softer regions of the HID. Both of these alternative evolutionary paths repeatedly cross the jet line, thus indicating that these sources emit short radio outbursts.

1.3.5 NS binaries

A characteristic that distinguishes NSs from BHs is the presence of a physical surface. This surface acts as an anchor for the magnetic field which can be detected in NSs. NSs are seen to have the most powerful magnetic fields in existence, with field strengths reaching $\sim 10^{15}$ G (Psaltis 2006). Strong magnetic fields (i.e., magnetic

[1]The hardness of an X-ray emitting source is a measurement of the number of high energy X-rays that are being emitted by the sources compared to the number of low energy X-rays being emitted. A source is referred to as being 'hard' if it is emitting a larger number of high energy photons than it is low energy photons, and 'soft' if it is emitting a larger number of low energy photons than photons with higher energies.

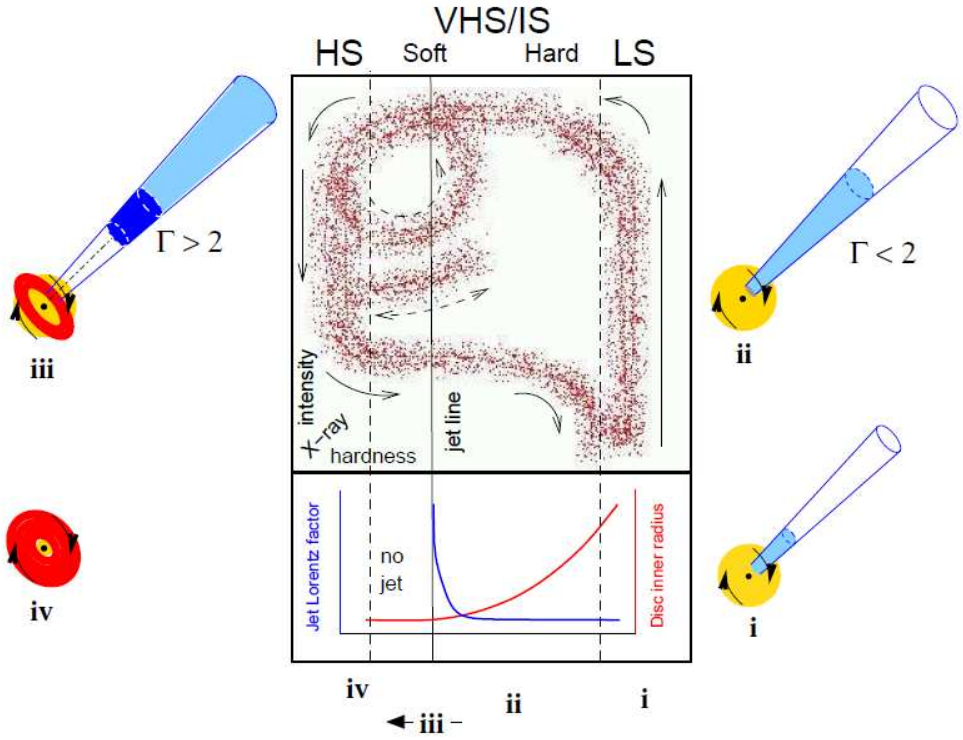

Figure 1.19: A schematic of the disc-jet coupling model of Fender et al. (2004). The top and bottom panels are described in the text. The sketches outside the 2 panels represent the physical conditions of the accretion disc (red), corona (yellow), and jet (blue) of transient BHBs as they evolve from state to state.

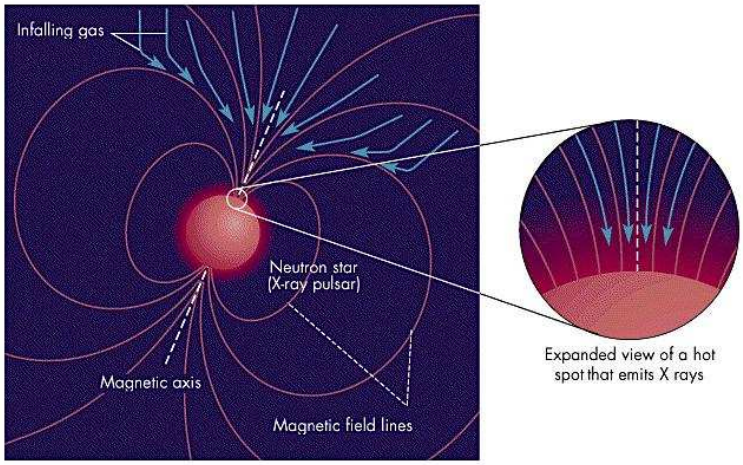

Figure 1.20: A cartoon of the accretion process X-ray pulsar systems. Taken from `http://www.mhhe.com/`.

fields with a strength range of $> 10^8$ G) are evident in the observation of pulsations in accreting NS binaries. These pulsations are caused by the interaction between accreted matter and the magnetic field, depending on the orbital frequency of the material when it reaches the Alfvén radius (i.e., the radius at which the magnetic field interacts with the matter being accreted) of the NS (e.g., Ghosh & Lamb 1991). If this orbital frequency exceeds the rotational frequency of the NS, the material is forced into co-rotation with the star, and is channelled along the magnetic field lines to the magnetic poles. X-ray emission from the hot magnetic poles of the NS are observed in modulation with the spin frequency of the NS, and is thus seen to be pulsating. This accretion process is illustrated in Figure 1.20. Such accreting NS are known as pulsars. There are 2 known class of X-ray pulsar: those that display pulsations of order a second, and those that display millisecond pulsations[2].

Several accreting NSs have been seen to display both weak magnetic field strengths ($< 10^8$ G) and rapid flashes of X-ray flux. These bursts of X-ray emission, which are known as Type-I X-ray bursts, are caused by the compression of material being accreted onto the surface of the NS to temperatures and densities that cause the

[2]For further reading on the topic of pulsating NSs, see Psaltis (2006).

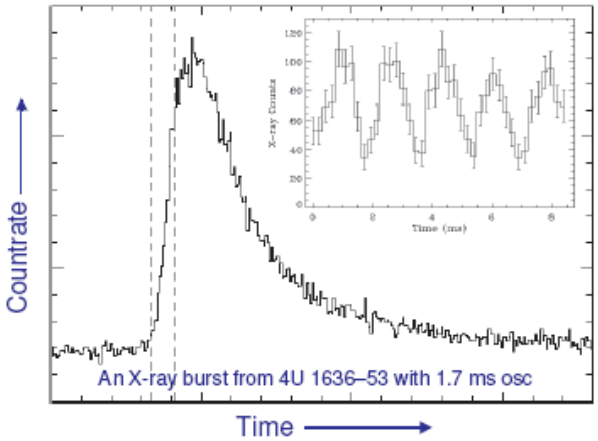

Figure 1.21: An X-ray lightcurve of the accreting NS 4U 1636-53, created using data from an *RXTE* observation of the source. Each time interval on the x-axis represents the passage of 2 seconds. The profile of this lightcurve is one that is typical of a Type-I X-ray burst. The inset panel displays the detected 1.7 ms oscillations in photon count rate during the burst. Taken from `http://hera.ph1.uni-koeln.de/`.

thermonuclear burning of helium (Lewin et al. 1996). The subsequent ignition of helium results in a rapid ($\sim$ 1 s) increase in flux, which is followed by a slower (a few $\times$ 10 s) cooling of the NS surface, resulting in a similar decay in flux. An example of a typical Type-I burst lightcurve can be seen in Figure 1.21. If such a burst is energetic enough, the force of the radiation will cause the surface of the NS to expand rapidly. During this expansion, the radiation from the source will be emitted at a rate close to the Eddington limit, and the remaining energy will be distributed within the expanding outer layer of the NS as potential and kinetic energy (Kato 1983; Nobili et al. 1994). These Eddington-limited bursts can be used to constrain the distance, mass, and radius of NSs (e.g., Kuulkers et al. 2003; Galloway et al. 2003). Observations have indicated that many sources that display Type-I bursts also display oscillations in flux that are highly coherent (e.g., Strohmayer et al. 1996; Strohmayer & Bildsten 2006). These oscillations have been interpreted as non-uniform burning of hydrogen on the surface of NSs (Strohmayer et al. 1996).

A number of accreting NSs have been seen to display emission similar to that of BHBs, i.e., persistent and transient emission. This is evidence that the NS in such an accreting system does not have a magnetic field strong enough to disrupt the material accreted by the star. As with transient BHBs, the outbursts in X-

ray emission seen in low magnetic field accreting NSs are likely to be the result of accretion disc instabilities (see above for more details). Although low magnetic field strength NS binaries and BHBs share similar attributes, a number of differences between them have been identified. For example, transient BHBs display periods of quiescence that are both significantly fainter and longer than those seen in their NS equivalents. This is likely due to mass differences between the 2 types of accreting compact objects, as well as the presence of an event horizon in BHs (Psaltis 2006).

Certain spectral similarities have been observed between the most luminous accreting NSs and BHBs, the most obvious being that these NSs display distinct hard and soft spectral shapes (e.g., Gierlinski & Done 2002; Maccarone & Coppi 2003). Figure 1.22 shows an X-ray colour-colour and colour-luminosity plot, displaying the colour evolution of a luminous ($L_{\rm peak} > 0.5L_{\rm Edd}$) subset of NSs known as atolls (e.g., van Straaten, van der Klis, & Wijnands 2005). The atolls can clearly be seen to transit between the hard 'island' and soft 'banana' regions of the colour-colour plot while increasing in luminosity (e.g., Hasinger & van der Klis 1989). Even though BHBs display a similar accretion state transition, differences have been noted between the evolution of accretion states in NSs and BHBs. These differences, which are illustrated in Figure 1.23, can be explained by the presence of a solid surface on NSs that add an additional hard component to the spectra (Gierlinski & Done 2002; Done & Gierlinski 2003)[3].

1.4 ULXs

ULXs are non-nuclear point-like X-ray emitting sources with luminosities $> 10^{39}$ erg s^{-1} in the 0.3 – 10 keV band. Although this definition is physically ambiguous, as it can encompass a diverse range of objects such as bright SNe (Immler & Lewin 2003) and young X-ray pulsars (Perna et al. 2008), the majority of the evidence implies that ULXs are a class of accreting BH system. For example, high levels of short-term and long-term variability have been reported in a large number of ULXs (e.g., Strohmayer & Mushotzky 2003; Heil et al. 2009; Feng & Kaaret 2009; Feng et al.

[3]For further reading on the topic of NS accretion states, see Done, Gierlinski, & Kubota (2007).

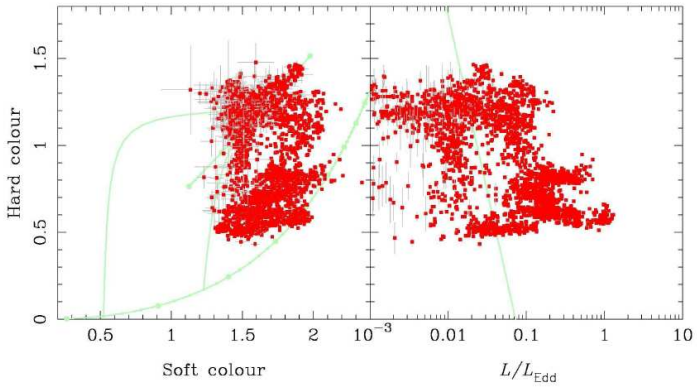

Figure 1.22: X-ray colour-colour and colour-luminosity plots of the sample of atolls studied by Gladstone et al. (2007). Taken from Done, Gierlinski, & Kubota (2007).

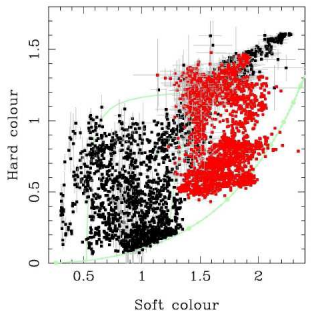

Figure 1.23: A plot comparing the colour-colour evolution of atolls (red dots) and BHBs (black dots). This plot clearly indicated a difference in the spectra of these sources. Taken from Done, Gierlinski, & Kubota (2007).

2010; Kong et al. 2010; Grisé et al. 2010), supporting a compact accretion-driven nature for these sources.

Although ULXs have been observed in a variety of galaxies, including ellipticals, spirals and irregulars, the majority of observed ULXs are seen to be associated with star formation (Feng & Soria 2011), and are therefore likely to be accreting HMXBs. On the other hand, it is possible that $\geq 2/3$ of the population of ULXs in elliptical galaxies can be explained as the upper end of their LMXB distribution (Feng & Soria 2011). However, even though these sources are most likely accretion powered XRBs, they are emitting X-rays at luminosities that exceed those of isotropically-emitting stellar mass BHs at the Eddington limit. The simplest explanation for such high luminosities is that the sources are powered by sub-Eddington accretion of matter by intermediate mass BHs (IMBHs): BH with a mass of $10^2 - 10^4\ M_\odot$ (e.g., Colbert & Mushotzky 1999; Miller & Colbert 2004). It has been suggested that such objects may be the remnants of massive, metal-free population III stars (Madau & Rees 2001). Another possibility is that IMBHs are formed by the direct collapse of 'superstars' built up by mergers in the cores of young, dense stellar clusters (e.g., Portegies Zwart et al. 2004). The most likely scenario is that these sources are BH nuclei of stripped dwarf galaxies that have been captured by the halos of more massive galaxy companions (King & Dehnen 2005; Bellovary et al. 2010). The most convincing evidence for the existence of IMBHs is seen in the extremely high luminosities and peculiar characteristics of a small number of ULXs, including M82 X-1 (e.g., Kaaret et al. 2001; Strohmayer & Mushotzky 2003) and HLX-1 in ESO 243-49 (Farrell et al. 2009; Davis et al. 2011).

Even though IMBHs are the simplest explanation for the high luminosities observed in ULXs, there are problems with the formation of large enough numbers of IMBHs necessary to power the observed ULXs in the local Universe (Madhusudhan et al. 2006), and in particular in starburst galaxies such as the Cartwheel (King 2009; Mapelli et al. 2008). Alternative explanations to what is powering the emission from ULXs have been suggested, including relativistic beaming, similar to that which is seen in microblazars (Fabrika & Mescheryakov 2001; Körding et al. 2002). Alone, strong relativistic beaming of ULX emission has presented a number of prob-

lems, such as the lack of ULXs with radio counterparts and/or X-ray variability (Feng & Soria 2011), and has therefore been discounted as a universal solution to ULX emission. Another possibility is that ULXs are powered by super-critical accretion, without collimation of emission (Begelman 2002). In this case, it is possible that inhomogeneities in radiation pressure-powered accretion discs cause ULXs to radiate at a rate ~ 10 times that of the Eddington limit for a stellar mass BH. The third and most favoured possibility is a combination of mild relativistic beaming with super-Eddington accretion. In this scenario, emission from the source is scattered and collimated in the direction perpendicular to the plane of the accretion disc by a radiation-powered outflow with a base located in the central regions of the accretion disc (King 2009; Poutanen 2007; Begelman et al. 2006).

ULXs have been reported to display spectra that are best fit with a combined multi-coloured disc blackbody plus power-law model, with best fitting inner disc temperatures of ~ 0.2 keV (e.g., Miller et al. 2003; Kaaret et al. 2003; Miller, Fabian & Miller 2004). These low disc temperatures indicate that the sources are powered by BHs with masses in the intermediate range. However, the best fitting parameters yielded when fitting the spectra of BHBs (and therefore also ULXs) with a disc blackbody model cannot be trusted, unless the sources are dominated by disc emission (Done & Kubota 2006). It has been observed that the spectra of ULXs are not likely to be dominated by disc emission, but rather by the presence of a strong tail (Miller et al. 2004; Stobbart, Roberts, & Wilms 2006). Also, certain characteristics in high quality spectra of ULXs have been discovered, such as a break in the hard spectral component above ~ 3 keV (Stobbart, Roberts, & Wilms 2006), that cannot be explained by models used to describe standard sub-Eddington accretion. It was suggested by Roberts (2007) that the emission from ULXs may not be interpereted as that from sub-Eddington accretion systems, but instead may be emission from a new 'ultraluminous state' regime. The existence of the 'ultraluminous state' was investigated by Gladstone, Roberts, & Done (2009), in which the accretion of a ULX is assumed to be super-Eddington, and the spectrum of the source is best fit with an accretion disc plus Comptonisation model. This model best describes the power-law shape of the spectrum that rolls over at ~ 3 keV. The physical interpretation for the

ultraluminous state is an accretion disc being obscured at low radius by a corona more extreme than those that are expected in the SPL state. Gladstone, Roberts, and Done (2009) reported that when the spectra of 12 ULXs were fit with this model, the best fitting inner disc temperatures indicated that the accretion of these sources was not necessarily explained by the presence of IMBHs. Further investigation into the nature of the ultraluminous state has since been conducted (e.g., Middleton et al. 2011b), thus expanding on the work of Gladstone, Roberts, and Done (2009).

1.5 Active Galactic Nuclei

An active galaxy is a galaxy that contains a highly energetic compact nuclear region, whose spectral and temporal characteristics cannot be attributed to stellar activity alone. The high bolometric luminosities that active galactic nuclei (AGN) display have instead been attributed to the accretion of matter by super-massive BHs (SMBHs, e.g., Zel'dovich & Novikov 1964; Salpeter 1964). In this scenario, the source of radiation is an accretion disc that has formed around a BH of mass $\gtrsim 10^5$ $M_\odot$ in the centre of the galaxy (e.g., Blandford 1985; Begelman 1985).

The first observation of an AGN was undertaken by E. A. Fath in 1908 with the Lick Observatory. In his doctoral dissertation, Fath noted the optical spectrum of the observed AGN, NGC 1068 (= M77), to display distinctively strong emission lines. In a later study of a sample of similarly bright objects, Seyfert (1943) noted the presence of both strong narrow and broad emission lines in the optical spectra of the galaxies. An optical spectrum of one of the galaxies in the sample (NGC 5548) is shown in Figure 1.24, where the prominent emission lines are labelled. Such strong emission lines have been attributed to the presence of a broad line region (BLR) and a narrow line region (NLR) within AGN. BLRs are dense ($N_e \sim 10^9$ – 10^{11} cm^{-3}, Ferland et al. 1992) regions of photoionised material located within the nucleus of active galaxies, with a typical spatial extent of 10 – 100 light-days. The widths of the broad lines emitted by these regions are assumed to be the result of Doppler broadening, and typically infer a velocity of a few $\times$ 10^4 km s^{-1} for the material emitting the radiation. Due to the density of material in these regions, forbidden

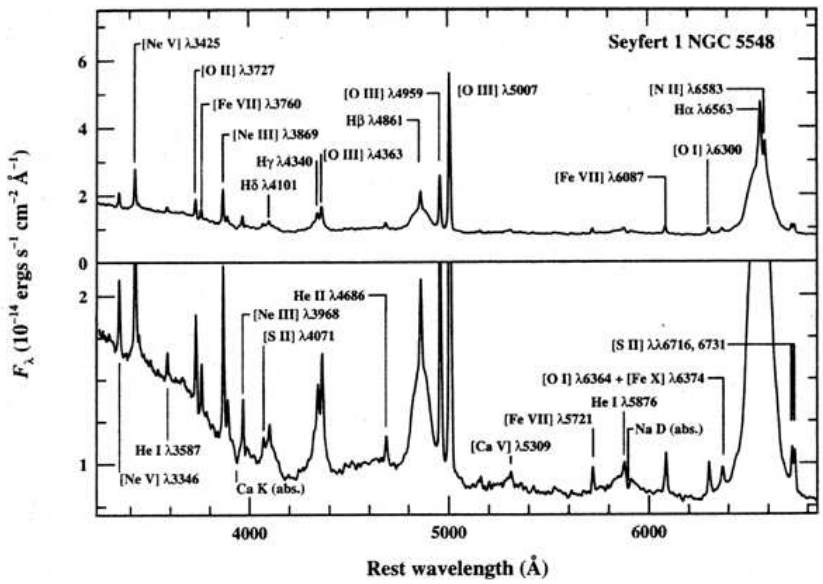

Figure 1.24: The optical spectrum of NGC 5548, one of the galaxies in the sample studies by Seyfert (1943). The strong broad and narrow lines are clearly indicated. Taken from Peterson (1996).

line emission is collisionally suppressed. However, spectral analysis has indicated the absence of a BLR in a number of AGN (e.g., Khachikan & Weedman 1974). This is believed to be the result of obscuration of the region by a thick dusty torus surrounding the AGN (Krolik, Madau, & Zycki 1994). It is the torus which forms the basis of the unification model of AGN (see below). Unlike BLRs, NLRs are regions of ionised material within AGN that display spatial extents of a few $\times$ 100 pc. The density of material within these regions is significantly lower than that in BLRs ($N_e \sim 10^3$ - 10^6 cm^{-3}), and hence allows for emission of forbidden optical lines. The widths of these lines infer velocities of a few $\times$ 100 km s^{-1}, significantly lower than those inferred from BLRs. Figure 1.25 shows a cartoon diagram of the anatomy of an AGN[4].

Although AGN are bolometrically bright, they are particularly noted for high luminosities in the X-ray band (Elvis et al. 1978). The study of the X-ray emission from AGN is one of great importance, as it is X-rays that can provide a probe into the central regions of these accreting systems. Although the X-ray emission from

[4]For a more detailed review of the BLR and NLR of AGN, see Peterson (1996).

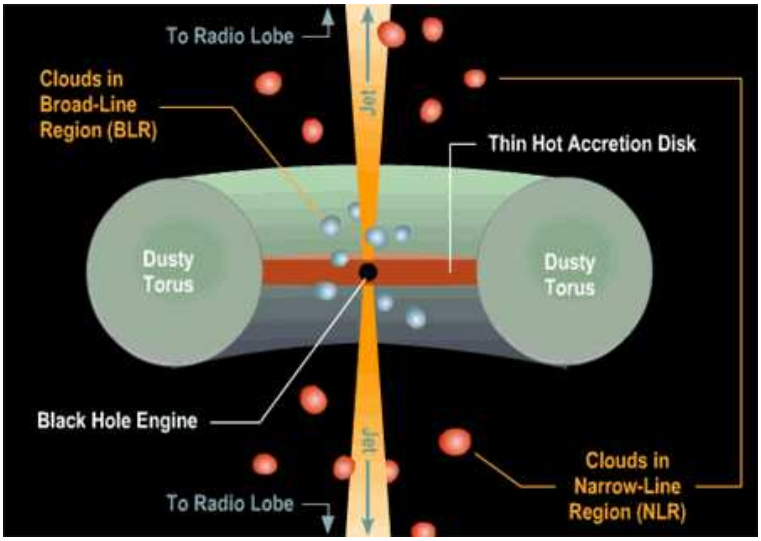

Figure 1.25: A cartoon diagram of the anatomy of an AGN. The constituent parts of the AGN are clearly labelled. Taken from `http://astronomyonline.org/`

AGN is not well understood, it has been modelled with relative success by inverse-Compton scattering of UV/optical photons from the accretion disc off hot electrons located in a corona surrounding the disc (e.g., Haardt & Maraschi 1993). Other complexities in the X-ray emission of AGN have been reported, particularly in the soft X-ray band, such as warm absorbers (Reichert et al. 1985; Blustin et al. 2005), and a soft excess (Arnaud et al. 1985; Turner & Pounds 1989; Gierlinski & Done 2004). Blustin et al. (2005) suggested the warm absorbers they encountered in the spectra of their sample of 23 AGN to be a result of torus outflows. The apparent soft excess seen in the large sample of AGN studied by Gierlinski & Done (2004) was suggested by the authors to be relativistically smeared, partially ionised absorption. Even though the emission from AGN can be particularly complex, lesser quality spectra (such as those of distant AGN detected in deep surveys) can generally be fit with a simple power-law model with a photon index of $\Gamma \sim 1.8$ (e.g., Alexander et al. 2005). As well as studies of the X-ray emission spectra of AGN, studies have been performed on the temporal properties of these sources (e.g., McHardy 1988; Markowitz et al. 2003; Uttley & McHardy 2004; Uttley, McHardy, & Vaughan 2005; Smith & Vaughan 2007; Sobolewska & Papadakis 2009; Vaughan et al. 2011). These studies have indicated that AGN are variable in the X-ray band both on short and

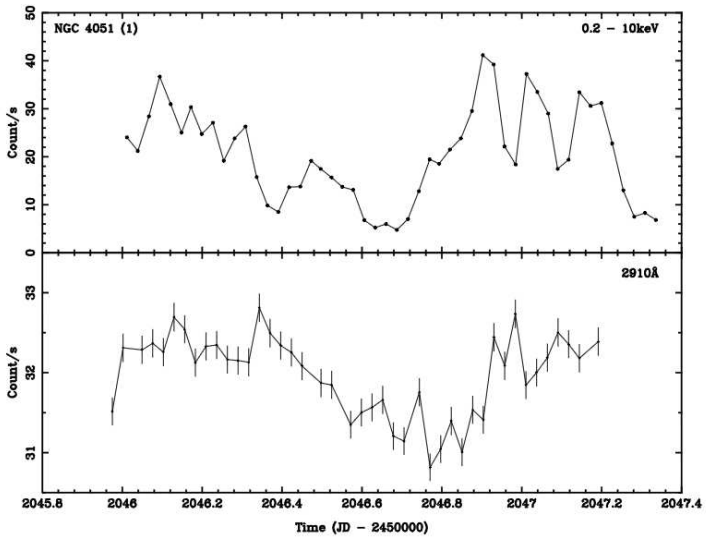

Figure 1.26: An X-ray (top) and optical (bottom) lightcurve of the AGN NGC 4051, created using data from an *XMM-Newton* EPIC and OM observation of the galaxy. Both X-ray and optical short-term variability can be seen in the galaxy. Taken from Smith & Vaughan (2007).

long time scales. An example of an AGN X-ray lightcurve can be seen in Figure 1.26. A contemporaneous optical lightcurve is also shown in the figure. It is suspected that a correlation between X-ray and optical variability exists within AGN (e.g., Peterson et al. 2000; Shemmer et al. 2001; Shemmer et al. 2003).

It has been recognised for a long time that AGN are a very heterogeneous class of object. Several sub-classifications of AGN have been identified, the most prominent being Seyfert galaxies and quasars. Other sub-classes have also been identified, including low ionisation nuclear emitting regions (LINERS), broad and narrow line radio galaxies (BLRGs and NLRGs), BL Lacs, and optically violent variables (OVVs). Below is a summary of the characteristics of these AGN sub-classes.

1.5.1 The taxonomy of AGN

Seyfert galaxies

Seyferts were first recognised to be a class of object by Seyfert (1943), due to their high nuclear surface brightness and unusual spectral properties. The definition of Seyfert galaxies has since evolved to include the emission of high ionisation lines.

Figure 1.27: An optical image of the Seyfert galaxy NGC 4051, taken using the 20 inch RC Optical systems telescope. This galaxy was among the first to be studied by Seyfert (1943). Image credited to George Seitz/Adam Block/NOAO/AURA/NSF. Taken from http://www.lunarplanner.com/.

Unlike quasars (see below), the hosts of Seyfert nuclei are clearly detectable. Observational studies have indicated that the majority of these host galaxies are spirals (e.g., Adams 1977). Figure 1.27 shows an optical image of NGC 4051, one of the sample of Seyfert galaxies studied by Seyfert (1943).

Seyfert galaxies can be divided into 2 distinct sub-classes: type 1 and type 2 Seyferts (Khachikian & Weedman 1974). The distinguishing factor between type 1 and type 2 Seyferts is the presence or absence of broad spectral emission lines. Type 1 Seyferts display spectra that contain the both broad and narrow emission lines superimposed onto one another, while type 2 Seyferts only display spectra with narrow emission lines (see previous section for more details on broad and narrow line emission). The differences between these 2 types of Seyfert galaxy may be explained by AGN unification (see below). A further sub-classification of type 1 Seyferts was introduced by Osterbrock (1981), based on relative strength of broad emission lines

to narrow emission lines. However, caution should be used in applying these sub-classifications, since emission line strengths in Seyfert spectra are known to vary (e.g., Penston & Pérez 1984).

Quasars

With extremely bright nuclei (M_V < -21.5 + log(h_0[5]), Schmidt & Green 1983), quasars are the brightest sub-class of AGN observed. As well as being extremely bright, quasars have a number of other observed characteristics, including a time variable flux continuum, a large UV flux, broad emission lines, and high redshifts (Schmidt 1969). Because of these high redshifts, the morphology of quasar host galaxies were initially observationally unresolvable, and so quasars are described as star-like. Figure 1.28 demonstrates this for 3C 273, which is a nearby quasar located at a redshift of $z \sim 0.16$ (Strauss et al. 1992). Recent observations of quasars with high spatial resolution instruments, such as those on board *HST*, indicate that these sources are surrounded by a 'fuzz' or low surface brightness halo. These halos are attributed to emission from stars within the host galaxies. Spectrally, quasars are very similar to Seyfert galaxies, the only differences being weaker relative narrow line/broad line strengths due to the Baldwin effect (Baldwin 1977; Baldwin, Wampler, & Gaskelll 1989), and weaker stellar absorption features in the spectra of quasars.

Quasars were originally defined as a class through detection in the radio band (e.g., Edge et al. 1959; Ekers 1969; Hazard, Gulkis, & Bray 1967; Ehman, Dixon, & Kraus 1970). Even though radio brightness was the original defining characteristic of these sources, it is now known that only $\sim 5 - 10\%$ of quasars display strong radio emission (Peterson 1996). The radio morphology of quasars (and other radio galaxies) is typically comprised of 3 components: compact and extended emission, and radio jets. The extended emission can be further divided into 2 sub-catagories: Fanaroff Riley I (FRI) and Fanaroff Riley II (FRII) emission (Fanaroff & Riley 1974). FRI sources are weaker, with the brightest emission coming from the central source

[5] h_0 is the Hubble constant in units of 100 km s^{-1} Mpc^{-1}.

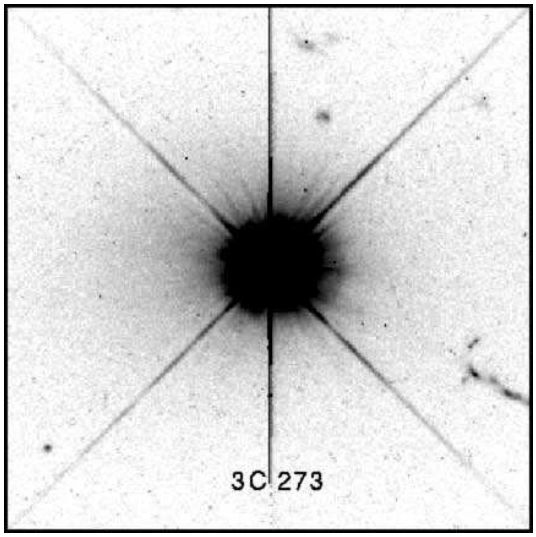

Figure 1.28: A *HST* optical image of the quasar 3C 273. The star-like appearance of quasars is clearly represented in this image. Image credited to John Bahcall. Taken from `http://www.alicesastroinfo.com`.

regions, becoming less bright towards the edges. FRII sources are considerably brighter than FRI sources, with emission being enhanced either at the edges of the extended radio structure, or within the structure itself. A radio image of the quasar 3C 175 is shown in Figure 1.29. This source is an example of a radio-extended jet-emitting quasar.

BLRGs and NLRGs

As well as quasars, other radio galaxies have been seen to display emission characteristics of AGN. BLRGs and NLRGs are among these sources, with optical emission analogous to that of type 1 Seyferts and type 2 Seyferts, respectively.

LINERS

LINERs are characterised by strong emission of low ionisation lines such as [OI]λ6300 and [NII]$\lambda\lambda$6548,6583 (Heckman 1980). Excluding this characteristic, the spectra of LINERs are very similar to those of type 2 Seyfert galaxies. Although the connection between these objects and other AGN classes is unclear, it has been suggested that LINERs may be low luminosity Seyfert galaxies (e.g., Peterson 1996). Another possibility is that the spectra emitted by LINERs could be produced by starburst-

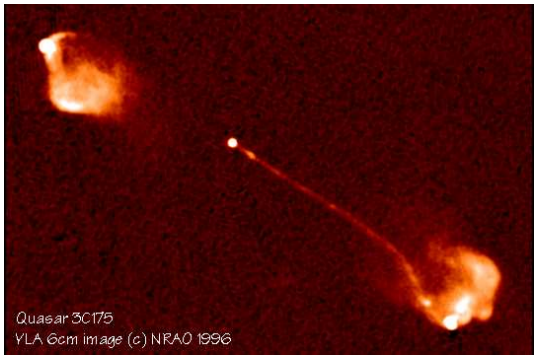

Figure 1.29: A 5cm radio image of the quasar 3C 175 taken using the *VLA* telescope. This source is clearly exhibiting both extended and jet emission. The extended emission can be seen in the presence of the lobes. Compact emission is also visible, originating at the active nucleus of the galaxy. Image credited to NROA/AUI. Taken from `http://images.nrao.edu/`

driven winds and shock-heated gas (Heckman 1987; Filipenko 1992). Figure 1.30 shows an example of a 'Baldwin, Phillips, & Terlevich' (BPT) diagram (Baldwin, Phillips, & Terlevich 1981) displaying the [NII]/Hα vs. [OIII]/Hβ line ratios of a sample of star forming regions (open circles), narrow-line AGN (closed circles), and LINERs (triangles). This diagram clearly shows that LINERs can be set apart from other AGN (and star forming regions) on the basis of emission line ratios.

BL Lacs and OVVS

Both BL Lacs and OVVs are characterised by high levels of variability and high luminosities in the radio band. A distinguishing factor between the 2 types of AGN is the absence of strong absorption and emission lines in the spectra of BL Lacs. Collectively, these sources are known as 'blazars' (e.g., Burbidge & Hewitt 1992), and are suspected to display strong relativistically beamed emission in the observed line of sight (Peterson 1996). The lightcurves of the blazar 3C 729 shown in Figure 1.31 are an example of the high levels of variability that can be seen in both the optical and X-ray emission from blazars.

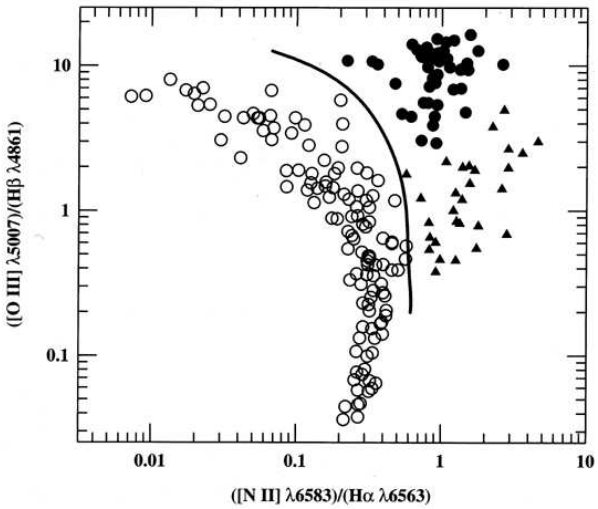

Figure 1.30: A BPT diagram displaying the [NII]/Hα vs. [OIII]/Hβ line ratios of a sample of star forming regions, narrow-line AGN, and LINERs. The ratios of the star forming regions, narrow-line AGN, and LINERs are represented by the open circles, closed circles, and triangles, respectively. The solid line represents an empirical division between AGN and star forming regions. Taken from Peterson (1997).

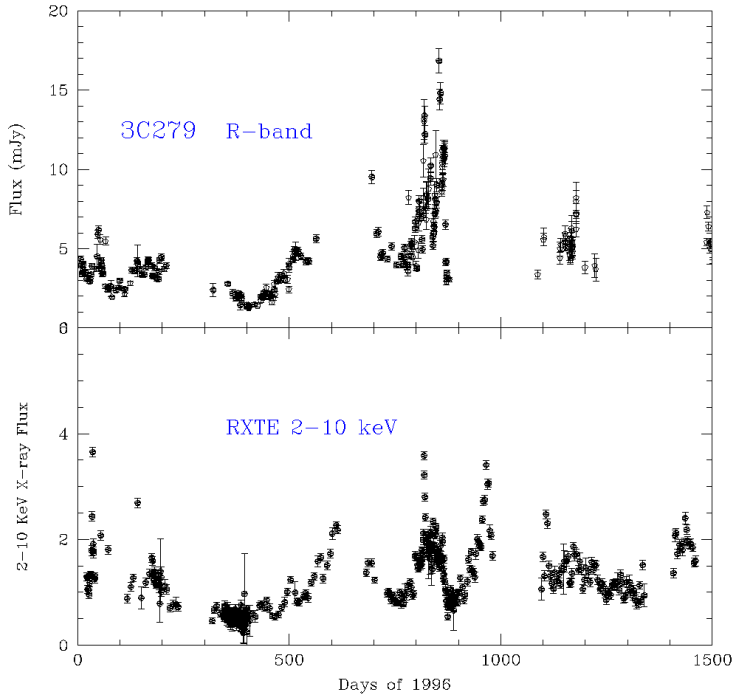

Figure 1.31: An R-band (*upper panel*) and 2 – 10 keV X-ray (*lower panel*) lightcurve of the blazar 3C 729. Taken from `www.astro.soton.ac.uk/`.

Table 1.1: A general AGN unification scheme

Radio properties	Orientation	
	Face-On	Edge-On
Radio Quiet	Seyfert 1	Seyfert 2
	QSO	FIR galaxy?[(1)]
Radio Loud	BL Lac	FR I
	BLRG	NLRG
Quasar/OVV	FR II	

Notes: [(1)] FIR galaxies are extremely IR-luminous galaxies that display luminosities similar to those of quasars, and narrow-line optical spectra (e.g., Jannuzi et al. 1994). This unification scheme was taken from Peterson 1996.

1.5.2 AGN unification

The basic idea of AGN unification is that all AGN are physically similar but display different characteristics when viewed from different perspectives (e.g., Rowan-Robinson 1977; Lawrence 1991; Antonucci 1993; Urry & Padovani 1995). Two essential elements in unification are the presence of a dusty torus within the central regions of AGN host galaxies and, in the case of radio sources, the presence of a synchrotron-emitting jet. The basic aspects of a general unification scheme are outlined in Table 1.1, and Figure 1.32. According to this scheme, if the observer is viewing the dusty torus face on, the central regions of the AGN are visible, and both broad and narrow emission lines can be detected. In the case of radio sources, the jets are parallel to the line of sight, thus making the sources appear radio-bright. On the other hand, if the observer is viewing the torus edge-on, then the central regions of the AGN are obscured, resulting in the lack of detection of broad emission lines. In this case, radio jets appear perpendicular to the line of sight of the observer. More generally, the inclination of an AGN between edge-on and face-on determines the amount of observable broad line emission and the brightness/inclination of the radio jet. It is worth noting that evidence for the unification of AGN is has been reported in the hidden broad lines in polarised light within of Seyfert 2 emission spectra (e.g., Antonucci & Miller 1985; Code et al. 1993), and in statistical testing (e.g., Goodrich et al. 1994; Peréz Garcia et al. 1998). However, a number of problems have been identified in AGN unification, one of which is the lack of narrow-line

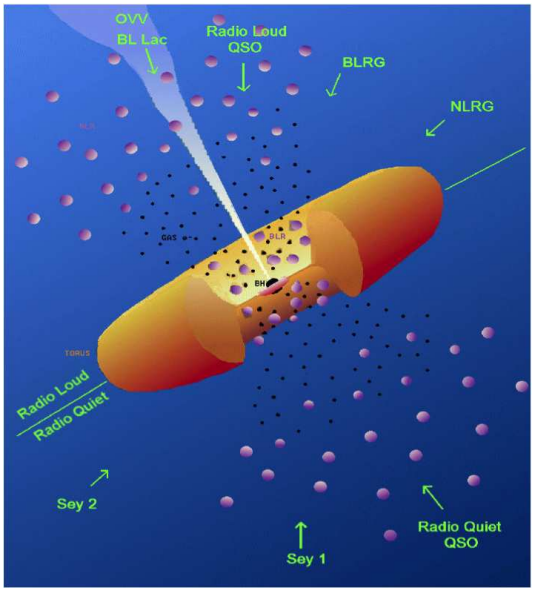

Figure 1.32: A cartoon of a general AGN unification scheme. The green arrows indicate the viewing angle of the observer. Taken from `http://www.integral.soton.ac.uk/`

quasars (e.g., Peterson 1996). Nevertheless, the idea of AGN unification is a very useful tool in the study of this class of object.

1.6 Observing the optical and X-ray sky

The results of this thesis are based on the analysis of optical and X-ray data from observations taken using the *Hubble Space Telescope*, *Chandra X-ray Observatory*, and *XMM-Newton*. The following sections summarise the instruments on board these 3 space telescopes that were used to observe the AGN and XRBs that are the focus of this thesis.

1.6.1 *The Hubble Space Telescope*

For over 2 decades, the *Hubble Space Telescope* (*HST*) has been providing astronomers with a large and amazingly clear view of the universe. The mission was launched on April 25 1990 as part of NASA's "Great Observatories" fleet, the only one of which to be put in an orbit that made it serviceable by Space Shuttle astronauts. The *HST* has been serviced 4 times over the last 20 years, with instru-

Table 1.2: Properties of the ACS and WFC3

	FOV[(1)] (arcsec)	Scale[(2)] (arcsec pix^{-1})	Response[(3)] (Å)
ACS			
WFC	202 × 202	∼ 0.05	∼ 3500 – 11000
HRC	29 × 26	∼ 0.028 × 0.025	∼ 1700 – 11000
SBC	34.6 × 30.8	∼ 0.034 × 0.030	∼ 1150 – 1700
WFC3			
UVIS	162 × 162	0.04	2000 – 10000
IR channel	126 × 138	0.13	850 – 17000

Notes: [(1)] Detector field of view; [(2)] Pixel scale; [(3)] Detector electromagnetic band response range.

ments being replaced and upgraded each time. Currently on board the *HST* are 6 scientific instruments, including 3 cameras, 2 spectrographs, and a fine guidance sensor. Among the cameras on board the observatory is the Advanced Camera for Surveys (ACS) and the Wide Field Camera 3 (WFC3), both of which were used extensively in the work of this thesis. Below is a summary of these 2 instruments.

The ACS

The ACS was designed to provide the *HST* with the capability to perform deep, wide-field surveys in a band ranging from the UV to the near-IR. The ACS is comprised of 3 detectors: a Wide Field Channel (WFC), a High Resolution Camera (HRC), and a Solar Blind Channel (SBC). The properties of the camera can be seen in Table 1.2. While the WFC and HRC are charge-coupled devices (CCDs) designed for observing a band ranging from the near-UV to the near-IR, the SBC is a multi-anode microchannel array (MAMA) that was created for UV observation. At 202 × 202 arcseconds, the WFC has the widest field of view among the 3 detectors. However, the HRC and the SBC both have superior spatial resolution, at ∼0.028 × 0.025 arcseconds pix^{-1}, and ∼ 0.034 × 0.030 arcseconds pix^{-1}, respectively. In order to obtain images in specific bands within the wavelength range of the camera, the ACS has been equipped with a large number of narrow and wide band filters.

The WFC3

The Wide Field Camera 3 (WFC3) is another state of the art instrument designed for wide-field imaging. This camera has been equipped with 2 channels, one for optimal detection in the UV (the UVIS channel) and the other for the near-IR (the IR channel), but also both provide capability in the optical band, thus endowing the *HST* with panchromatic science capabilities. The properties of these detectors can be seen in Table 1.2. The UVIS channel has both excellent spatial resolution and a large field of view. Although the resolution of the IR channel is not as high as that of most of the detectors on board the *HST*, the field of view of this channel is considerable. As with the ACS, a large number of wide and narrow band filters have been given to the WFC3, so that observations can be taken in specific bands within the UV, optical, and IR wavelengths.

1.6.2 *The Chandra X-ray Observatory* and *XMM-Newton*

In 1999, the launch of NASA's *Chandra Space Telescope* (*Chandra*, Weisskopf 1999) and ESA's *XMM-Newton* (Jansen et al. 2001) gave rise to a significant development in the fields of astronomical X-ray imaging and spectroscopy. While the instruments on board *XMM-Newton* provide X-ray astronomers with both an excellent field of view and high throughput spectroscopy, those on board *Chandra* provide superb high resolution X-ray imaging capabilities. Chief among these instruments are the *XMM-Newton* European Photon Imaging Camera (EPIC) and *Chandra* Advanced CCD Imaging Spectrometer (ACIS), both of which have been used extensively in the work of this thesis. Both of these instruments are discussed in more detail below.

ACIS

ACIS is an array of 10 charge couple device (CCD) chips that have been designed for both X-ray imaging and spectroscopy. The ACIS array is divided into 2 sub-arrays, the ACIS-S and ACIS-I, which are comprised of an array of 4 and 6 CCDs, respectively. The layout of the ACIS array is shown in Figure 1.33. The aimpoints of each array are marked by a cross symbol. Note that 8 of the 10 chips are front illuminated

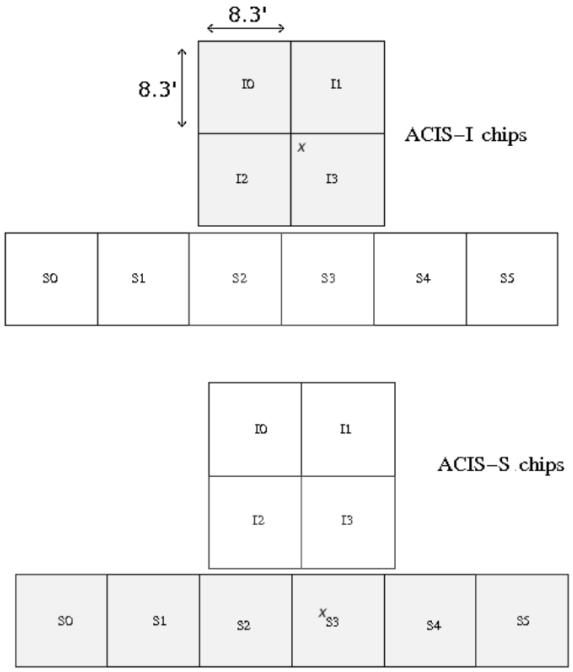

Figure 1.33: The layout of ACIS on the focal plane of the *Chandra X-ray Observatory*, with the different components of the instrument labelled accordingly. The top part of the diagram has the ACIS-I array highlighted, while the bottom part has ACIS-S highlighted. The aimpoint of each of the arrays is marked by a cross symbol. Taken from `http://cxc.harvard.edu/`.

(FI), while the remaining 2 (S1 and S3, see Figure 1.33) are back illuminated (BI).

With a spatial resolution of $\sim$ 0.5 arcseconds, and a reasonable field of view (16.9 $\times$ 16.9 arc minutes for ACIS-I, and 8.3 $\times$ 50.6 arc minutes for ACIS-S), the greatest asset the ACIS array possesses is its imaging capabilities in the 0.2 – 10 keV band. Spectroscopy can be performed using this instrument, although the detector has a limited sensitivity at higher energies (which is illustrated in Figure 1.34). Also pile-up, which is the loss of photon counts as the result of the detection of 2 or more photons as a single event[6], is an issue for objects brighter than $\sim 10^{-12}$ erg cm^{-2} s^{-1}.

[6]For more detailed information on pile-up, see Davis 2001.

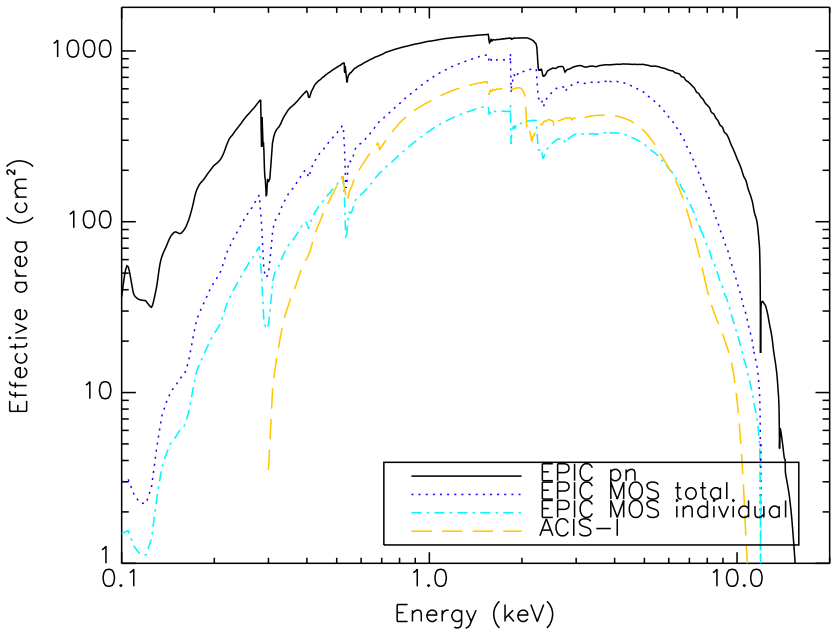

Figure 1.34: A plot of the effective area of the *XMM-Newton* MOS and pn and *Chandra* ACIS-I arrays. The legend highlights the corresponding colours of the effective area curves for each of the arrays.

EPIC

The EPIC instrument is comprised of 3 cameras, namely the Metal Oxide Semiconductor 1 (MOS1), MOS2, and pn CCD arrays. Both MOS detectors are comprised of 7 FI CCDs, located in the focal plane of each of the cameras. The CCDs in both of the cameras are configured so that there is 1 central CCD which is surrounded by the remaining 6, which are stepped outwards to approximate the focal curvature of the telescope. On the other hand, the pn camera is a uniform fabrication of 12 (3×1 cm) BI pn-CCDs in a single wafer. For redundancy reasons, the wafer is sub-divided into 4 quadrants. Overall, the configuration of the MOS and pn arrays, which can be seen in Figure 1.35, has been designed for an optimally large collecting area.

The collecting area of both EPIC cameras, particularly those of the pn array, are superior to those of the ACIS array (see Figure 1.34). Also, the field of view of the MOS and pn arrays is considerably greater than that of ACIS ($\sim$ 30 arc minute diameter circular field-of-view for MOS for both MOS and pn cameras). However,

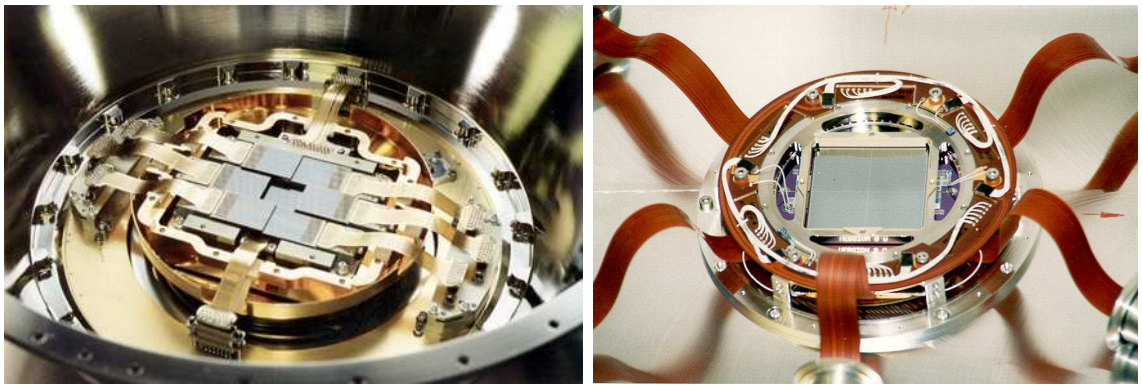

Figure 1.35: *Left:* An image of 1 of the 2 MOS CCD arrays. *Right* An image of the pn CCD array. Taken from `http://xmm.esac.esa.int/`.

with a spatial resolution of $\sim$ 6 arcseconds, the imaging capabilities of the EPIC cameras are considerably more limited than those of ACIS.

1.7 Aims of this work

The array of point-like X-ray emitting sources that have been detected in active star forming galaxies is large, and includes objects such as XRBs (e.g., Fabbiano & White 2006), ULXs (e.g., Fabbiano & White 2006) and AGN (e.g., Peterson 1997). The work in this thesis investigates the properties of a number of such sources with 3 specific aims: to determine whether the X-ray emission from luminous ($L_{\rm X} > 10^{42}$ erg s^{-1}), optically ambiguous galaxies is due to AGN or starbursts; to constrain the ages of the XRB population located within the metal-rich starburst galaxy NGC 922; and to investigate the X-ray properties of the most luminous X-ray point sources in the archetypal starburst galaxy M82. To these ends, Chapter 2 provides a detailed study of the X-ray spectral, timing, and extent of 3 X-ray bright mid-redshift (z $\sim$ 0.1) *SDSS* galaxies that display optical spectra ambiguous to the presence of AGN activity. Then, a detailed description of a study undertaken to constrain the ages of the luminous XRB population of the drop-through ring galaxy NGC 922, using the presence of young stellar clusters close to the XRBs, is given in Chapter 3. Chapter 4 describes the X-ray spectral and temporal analysis of the 8 brightest X-ray sources in the starburst galaxy M82, using data from several deep

observations obtained as part of the $\sim$ 480 ks total observations that comprise the *Great NASA Observatory M82 Extended Survey* (*GNOMES*). We conclude this thesis in Chapter 5 with a summary of the main results of this work, and possible directions for future studies.

Chapter 2

On the nature of high X-ray luminosities in *SDSS* galaxies

2.1 Introduction

Deep and wide area X-ray surveys (e.g., Alexander et al. 2003; Lehmer et al. 2005; Kim et al. 2007; Elvis et al. 2009; Watson et al. 2009; Xue et al. 2010) have resolved up to $\approx 90\%$ of the X-ray background into discrete sources over the 0.5–8 keV band (e.g., Lumb et al. 2002; Moretti et al. 2003; Bauer et al. 2004; Worsley et al. 2005; Hickox & Markevitch 2006). The majority of the objects detected in these surveys are luminous X-ray sources at $z \approx 0.2$–5 with $L_{\rm X} \geq 10^{42}$ erg s^{-1} (e.g., Hornschemeier et al. 2001; Barger 2003; Brandt & Hasinger 2005; Treister et al. 2005; Silverman et al. 2010). Many of these luminous X-ray sources are clearly AGN, as demonstrated by the detection of either optical AGN signatures (i.e., broad emission lines and/or narrow high-excitation emission lines; e.g., Barger et al. 2002; Szokoly et al. 2004) or hard X-ray spectra ($\Gamma \leq 1$; Mushotzky et al. 2000; Giacconi et al. 2001). However, a significant fraction of these luminous X-ray sources display optical spectroscopic signatures consistent with star formation (e.g., Barger et al. 2002; Szokoly et al. 2004; Eckart et al. 2006; Trouille et al. 2008). The luminous X-ray emission could be due to either AGN activity where the optical spectroscopic signatures are extinguished or diluted (e.g., Moran et al. 2002; Maiolino et al. 2003; Goulding & Alexander 2009), or star formation activity.

These objects are distinct from the population of X-ray dim, 'normal', star forming galaxies now being revealed in deep high-Z surveys (e.g., Lehmer et al. 2008).

If confirmed as star forming galaxies, then these luminous X-ray sources will be the most powerful starburst galaxies known (with $L_{\rm X} \approx 10^{42}$–$10^{43}$ erg s^{-1}), exceeding the X-ray luminosity of the brightest star forming galaxies in the local Universe by over an order of magnitude (e.g., Moran et al. 1999; Zezas et al. 2001; Lira et al. 2002; Ptak et al. 2003). However, accurately characterising the X-ray emission from these distant luminous X-ray sources is challenging due to their faint fluxes and therefore limited X-ray photon statistics. Greater insight into their nature can be gained by selecting the rare nearby ($z < 0.15$) examples of these luminous X-ray sources where the photon statistics are much improved (e.g., Horschemeier et al. 2005). The advantages of this approach are twofold; firstly the accurate characterisation of the X-ray emission via X-ray spectral and variability analyses, and secondly the accurate characterisation of the optical spectroscopic signatures.

In this work we present *XMM-Newton* data and detailed analyses of three X-ray luminous galaxies at $z \approx 0.1$. These targets were selected from the ≈ 80 deg^2 overlap between the pre-release version of the source catalogue of the *XMM-Newton* Serendipitous survey (2XMMp-DR0)[1] and the Sloan Digital Sky Survey data 5 (*SDSS*-DR5)[2]. The aim of this study is simply to determine whether the X-ray emission is powered by tar formation, or by AGN activity. This chapter is structured as follows: in section 2, we give details about the source selection criteria. The X-ray observations used in this study are described in section 3, along with the data reduction details. In section 4, we describe the results of the spatial, spectral, and timing analyses performed on the X-ray data for each source. In section 5, we discuss the results, and finally, we conclude the chapter in section 6. Throughout this work, we assume the values $H_0 = 71$ km s^{-1} Mpc^{-1}, $\Omega_{\rm M} = 0.27$ and $\Omega_{\rm Vac} = 0.73$. Throughout this work, and the work of this thesis, RA and Dec coordinates from the J2000 epoch will be used.

[1]The 2XMMp catalogue (http://xmmssc-www.star.le.ac.uk/Catalogue/2XMMp/) is a subset of the full 2XMM catalogue (Watson et al., 2009). Most of the details of its production are very similar to the full 2XMM catalogue, as described by Watson et al. (2009).

[2]`http://www.sdss.org/dr5`

2.2 Source selection

As an initial step, we cross-correlated the *SDSS*-DR5 and 2XMMp-DR0 catalogues. From the large number of cross-matches we then selected X-ray sources that were identified with galaxies possessing star formation dominated *SDSS* optical spectra, with no clear AGN signature. The criteria used included, for example, strong narrow emission lines, low [SII]/Hα and [OIII]/Hβ ratios, and underlying continua dominated by young stars.

These serendipitous X-ray bright starburst galaxy candidates were then further filtered to provide a small sample of objects for follow-up observations in order to conduct a more detailed investigation. The main criteria were: (i) unusually high apparent X-ray luminosity for a starburst galaxy, $L_{\rm X} > 10^{42}$ erg s^{-1}, and (ii) an estimated on-axis EPIC-pn count rate in excess of 0.01 ct s^{-1} for better photon statistics. Nineteen sources were found to match the first criterion. Of these sources, three were identified matching the second criterion: 2XMMp J082042.4+205715, 2XMMp J123719.3+114915, and 2XMMp J140052.5-014510. The characteristics of these three objects are presented in Table 2.1. Figure 2.1 shows the emission-line diagnostic diagrams representing the [SII]/Hα versus [OIII]/Hβ ratios of a large sample of galaxies, selected from the *SDSS*-DR7 catalogue. Included in this sample are the ratios of our three galaxies, represented by the three filled squares in both panels. All three of the sources' flux ratios lie well within the starburst region of the diagram. We also looked at the case of the [NII]/Hα versus [O III]/Hβ diagnostic, and found that the three sources' ratios lie within the diagram's Transition region. This, however, does not indicate a definite presence of AGN activity. For example, a number of pure star forming galaxies such as NGC 7714, Mrk 711, and UM 304 have flux ratios that pertain to those of Transition sources (Terlevitch et al. 1991). No evidence has been reported on the presence of AGN activity within these galaxies. The filled circles represent the remaining 16 sources that were selected from the *SDSS* catalogue based on high X-ray luminosity.

We obtained *SDSS* optical data for the objects from the *SDSS*-DR7 catalogue[3].

[3]The observations were taken in 2002 and are associated with the *SDSS*-DR5 release. The reduc-

Table 2.1: Catalogued properties of the X-ray luminous starburst galaxies

Source ID		Mag [a]	z	F_{25} [b]	R_{25} [c]	$A_{\rm B}$ [d]	$N_{\rm H}$ [e]	Notes [f]
2XMMp...	*SDSS*...			(arcsec)		(mag)	(10^{20} cm^{-2})	
J082042.4+205715	J082042.46+205714.9	16.6g	0.114	9.6	1.28	0.213	4.25	(1)
J123719.3+114915	J123719.34+114915.9	18.3g	0.108	3.6	1.09	0.183	2.56	
J140052.5-014510	J140052.57-014510.0	17.7g	0.149	5.4	1.13	0.232	3.89	(2)

Notes: [a] Observed *SDSS* magnitude and filter; [b] Semi-major axis of the D_{25} isophotal ellipse; [c] Ratio of D_{25} major and minor axes; [d] Galactic foreground extinction according to Schlegel et al. (1998); [e] Galactic neutral absorbing column from COLDEN ; [f] Additional notes: (1) This source was previously detected in the 0.2 – 2 keV X-ray band by *ROSAT*, at a flux of 7.6×10^{-14} erg cm^{-2} s^{-1}. It was also detected as an infra-red source by the 2MASS survey with a J-band magnitude of 14.33, and as a radio source in the FIRST and NVSS surveys at a 1.4 GHz flux density of 4 mJy. (2) Also detected in the 2dF Galaxy Redshift Survey (Colless et al. 2001) as 2dFGRS TGN272Z262, confirming the above redshift measurement. Data for the galaxy properties are taken from the *SDSS* catalogue, and the notes result from searches in the NED (http://nedwww.ipac.caltech.edu/) and SIMBAD (http://simbad.u-strasbg.fr/simbad/) databases.

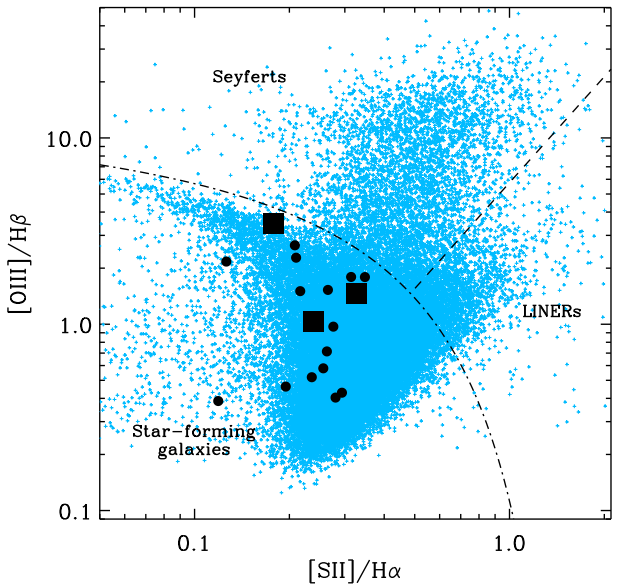

Figure 2.1: Emission-line diagnostic diagram displaying the [SII]/Hα versus [OIII]/Hβ line ratios of a large sample of galaxies, selected from the *SDSS* catalogue. Among these galaxies are the three sources being studied in this work, whose flux ratios are represented by the filled squares. The filled circles represent the flux ratios of the 16 remaining sources from the cross-correlation of *SDSS* and 2XMMp that were selected for their high X-ray luminosity (i.e., a luminosity $> 10^{42}$ erg s^{-1}). The dot-dash curves represent the Kewley et al. (2001) theoretical maximum starburst line. The dashed line represents the Kauffman et al. (2003) border between the diagrams' LINER and Seyfert regions. The blue dots represent the line ratios of a large sample of galaxies, selected from the *SDSS*-DR7 catalogue.

The sources' optical spectra can be seen in Figure 2.2. Optical AGN signatures (i.e., emission lines from broad and narrow line regions near to an AGN) are lacking in these spectra. However, signs of star formation, such as the presence of strong Hα and Hβ lines, are seen. Along with the optical data, radio data were obtained from the NRAO *VLA* Sky Survey (NVSS)[4] and the *VLA* Faint Images of the Radio Sky at Twenty-Centimeters (FIRST) survey[5] for each source. Using both the optical and radio data, we estimated the sources' Hα and 1.4 GHz radio fluxes, and converted them to star formation rates as per Doherty et al. (2006) and Bressan et al (2002), respectively. We also estimate the sources' X-ray star formation rates as per Grimm et al. (2003). Estimated star formation rates can be seen in Table 2.2. In all three sources, a moderate Hα star formation rate is seen, ranging from ~ 6 to ~ 30 $M_\odot$ yr^{-1}. Two of the three radio star formation values are calculated using conservative 3σ upper limits to radio flux, and therefore only represent upper limits to star formation rates, with $SFR_{1.4GHz} < 95$ and < 50 $M_\odot$ yr^{-1} for J123719.3+114915 and J140052.5-014511, respectively. The one remaining star formation rate is relatively high, at 110 $M_\odot$ yr^{-1} for J082042.4+205715. The X-ray estimates are a lot higher than these values, at 400, 200, and 1000 $M_\odot$ yr^{-1}. These extremely high values were calculated on the assumption that the X-ray emission from these galaxies is powered by star formation alone. This suggests that non-stellar activity is dominating the X-ray emission. We investigate this possibility in later sections of the chapter.

Because the sources are off-axis in the serendipitous observations, these data are not good enough to yield high quality photon statistics. Therefore, new *XMM-Newton* observations were sought and obtained for two of the objects (PI: Roberts); two of the three were also awarded new observations on *Chandra* (PI: Gelbord) with the third already being observed at the edge of the NGC 2563 group field-of-view. Details of the full set of *XMM-Newton* and *Chandra* observations of the three objects are presented in Table 2.3.

---

tion of the spectra was done in 2008, and is associated with *SDSS*-DR7 (http://www.sdss.org/dr7/)

[4] `http://www.cv.nrao.edu/nvss/`

[5] `http://sundog.stsci.edu/`

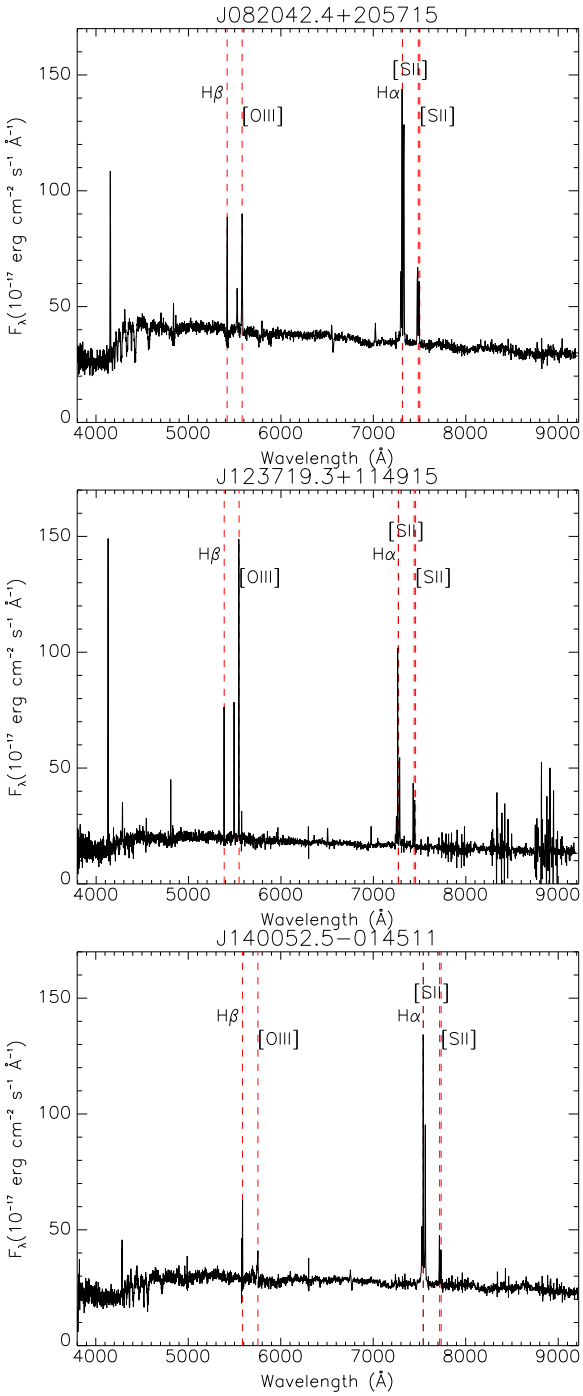

Figure 2.2: *SDSS*-DR7 optical spectra of J082042.4+205715 (top), J123719.3+114915 (middle), and J140052.5-014511 (bottom). None of the spectra show strong signs of AGN activity. Also, signatures for star formation, such as the presence of dominant narrow Hα and Hβ emission lines, can be seen within these spectra, indicating the existence of star forming activity within the sources' nuclei.

Table 2.2: Estimated star formation rates for the target galaxies

Source ID (2XMMp...)	Balmer Decrement	A_V [a] (mag)	$L_{H\alpha}$ [b] (10^{42} erg s^{-1})	$SFR_{H\alpha}$ [c] ($M_\odot$ yr^{-1})	$F_{1.4\ GHz}$ [d] (mJy)	$SFR_{1.4\ GHz}$ [e] ($M_\odot$ yr^{-1})	L_X [f] (10^{42} erg s^{-1})	SFR_X [g] ($M_\odot$ yr^{-1})
J082042.4+205715	6.55	2.40	3.55	28.1	4.5[i]	110	5.4	400
J123719.3+114915	4.20	1.11	0.70	5.6	< 4.4[ii]	< 95	2.8	200
J140052.5-014510	7.68	2.86	4.21	33.4	< 1.1[i]	< 50	13.9	1000

Note: [a] V-band extinction, calculated with the assumption that the non-reddened Balmer ratio should be 2.86; [b] De-reddened Hα luminosity; [c] Hα star formation rate as per Doherty et al (2006); [d] 1.4 GHz radio flux; [e] 1.4 GHz radio star formation rate as per Bressan et al (2002). Note that the radio fluxes recorded in this table for both J123719.3+114915 and J140052.5-014511 are conservative 3σ upper limits; [f] Initial 0.3 – 10.0 keV X-ray luminosity measurement based on the 2XMMp catalogue; [g] X-ray star formation rates calculated as per Grimm et al. (2003). [[i] as observed by the NVSS; [ii] as observed by the FIRSTsurvey.]

Table 2.3: Summary of the observational data used in this chapter.

Source ID (2XMMp...)	Obs ID	Observation date [a]	Instrument [b]	Off-axis angle [c] (arcmins)	Exposure [d] (ks)	Detected source counts	lightcurve bin size [e] (s)
J082042.4+205715	0108860501[1]	15-10-2001	EPIC	7.1	16.3	625±61	2500
J082042.4+205715	7925[1]	18-09-2007	ACIS-I	9.7	48.8	278±19	5000
J082042.4+205715	0505930301*[2]	04-04-2008	EPIC	0	36.6	4405±133	1500
J123719.3+114915	0112840101[1]	12-06-2003	EPIC	4.7	14.7	185±55	2500
J123719.3+114915	9558[2]	29-02-2008	ACIS-S	0	49.3	134±12	12500
J140052.5-014510	0200430901[1]	02-07-2004	EPIC	11.0	7.5	571±41	500
J140052.5-014510	0505930101*[2]	18-10-2007	EPIC	0	21.4	3743±99	1000
J140052.5-014510	0505930401*[2]	10-01-2008	EPIC	0	16.4	1760±91	500
J140052.5-014510	9557[2]	11-03-2008	ACIS-S	0	49.4	1780±42	2500

Notes: [a] Date in dd-mm-yyyy. [b] EPIC=*XMM-Newton* EPIC-MOS and pn cameras; ACIS-S = *Chandra* ACIS-S camera; ACIS-I = *Chandra* ACIS-I camera. [c] Angular distance between the pointing axis for the observation (for *XMM-Newton* this is taken from the pn detector axis) and the source. [d] The flaring-compensated exposure time. [e] The timing analysis lightcurve bin sizes. * The targets of these observations are recorded in the archive as 2XMMp J082042.5+205715, and 2XMMp J140052.6-014511, as a result of rounding errors by the proposers. [1] Observations from which the data are archival. [2] Observations from which the data was obtained especially for this study.

2.3 Observations and data reduction

A total of nine X-ray observations are examined in this analysis. The archival data sets were either downloaded from the *XMM-Newton* Science Archive[6] or the *Chandra* Data Archive[7]. The three targets were initially identified at a variety of off-axis angles in three separate serendipitous *XMM-Newton* detections (see Table 2.3). J082042.4+205715 and J140052.5-014510 were subsequently observed on-axis as the target of follow-up *XMM-Newton* observations, with the latter observed on two separate occasions. All observations were taken in a full frame imaging mode, although in the *XMM-Newton* observation 0505930101, only the pn and MOS1 detectors obtained sufficient data for the analysis. This is because the pn had a full active buffer during the observation, which resulted in the data begin lost from the MOS2 detector. The overall exposure of MOS2 was $\sim$ 5 ks as a result, thus yielding a net photon count of $\sim$ 20.

Reduction of the *XMM-Newton* data was performed using *XMM-Newton* SAS version 8.0.0 software. Contamination by background flaring was present in all observations. In order to remove this, good time interval (GTI) files were created by excluding periods during which the count rate in the 10 - 15 keV full field pn lightcurves exceeded 1 ct s^{-1}, and the data were filtered to remove these periods in the subsequent analyses.

Spectral data were extracted from circular regions of radius 45 arcseconds, centred on each of the source positions, with only two exceptions. In observation 0112840101, J123719.3+114915 is located immediately adjacent to a chip gap in the MOS1 data, forcing us to obtain the data in an aperture of only 12.5 arcseconds radius. The resulting aperture encircled only 50% the energy of the source. This loss of area was compensated for by the corresponding source ancillary matrix file (see below). In the case of the 0505930301 data, J082042.4+205715 was sandwiched between a nearby source – not present in the 0108860501 data – and a pn chip gap, causing the aperture to be shrunk to 30 arcseconds radius (a slight offset of

[6] `http://xmm.esac.esa.int/xsa/`
[7] `http://cxc.harvard.edu/cda/`

the aperture allowed a full 45 arcsecond radius region to be used in the MOS data). Corresponding background files were extracted from source-free circular regions with radii at least 1.5 times greater than source extraction regions, or multiple regions with a summed area equivalent to this. They were positioned on the same chip as, and in close proximity to, the source regions. The spectral data files were extracted with FLAG = 0 and either PATTERN $\leq$ 4 for pn or PATTERN $\leq$12 for MOS, using standard *XMM-Newton* tasks. Response matrix and ancillary response files were also created as part of these tasks. In all but one of the resulting spectral files the data were grouped into bin sizes of at least 20 counts per bin. The spectra from 0112840101 were left unbinned as the overall number of photon counts (185 $\pm$ 55 cts) was too low to be compatible with model fitting via standard χ^2 analysis. Instead, Cash statistical analyses (Cash 1979) were utilised on the spectral data (see Section 2.4.3).

Source and background lightcurves were extracted in the standard manner to facilitate timing analysis of the *XMM-Newton* data. This used the same regions from which the spectral files were extracted. For the analysis of this data, we set a minimum signal to noise ratio (S/N) requirement of $\geq$ 5 per bin. In order to accommodate this, the lightcurve bin sizes were set according to the source photon count rate. Table 2.3 contains details of the temporal binning corresponding to individual observations. In order to correct for GTI gaps (due to background flaring) that left substantial time periods missing within individual lightcurve bins - and hence gave erroneous count rates - we created new GTI files on the same binning as the lightcurves. These were used when extracting the lightcurves, and effectively removed the time bins associated with flaring, leaving only bins containing reliable count rates.

Unlike the *XMM-Newton* observations, only one of the three sources was detected serendipitously with *Chandra* (again, see Table 2.3). This source, J082042.4+205715, was detected off-axis by the ACIS-I instrument with the camera in the full frame, timed exposure mode. The remaining two sources were observed by the ACIS-S instrument in two separate on-axis follow-up observations, again with the camera in a full frame, timed exposure mode. All of the data were obtained in the very faint

telemetry format.

The *Chandra* data was reduced using CIAO software (version 4.1.1), adopting standard methods. Spectra were extracted using the CIAO SPECEXTRACT routine. In the subsequent spectral analysis the spectral data files for observations 7925 and 9558 were left unbinned due to the low quality of the data and, as with the lower quality *XMM-Newton* data, Cash statistical analysis was performed. The one remaining observation, 9557, possessed sufficient source counts to permit binning to at least 20 counts per bin and model fitting using χ^2 statistics. As per the timing analysis with *XMM-Newton* data, *Chandra* lightcurves were extracted from apertures similar to those used to extract the spectra. The bin sizes for the lightcurves were again set using the S/N $\geq$ 5 requirement (also see Table 2.3 for the *Chandra* lightcurve binning).

2.4 Results

2.4.1 Point source analysis

A first, key test of whether the X-ray emission of the selected objects originates in an AGN or a starburst region, is whether the X-ray emission appears point-like at the highest available spatial resolution. If extension is present, this would confirm that there is a spatially extended X-ray emission region, consistent with at least part of the X-ray emission originating in a large starburst region. Such a test is possible for our objects as high spatial resolution ($<$ 1 arcsec/pixel) *Chandra* data are available for all three of them. We show both the identification of the counterpart starburst galaxy on an *SDSS* R-band field, and a close-up of the individual galaxy with *Chandra* X-ray emission contours overlaid, in Figure 2.3. Note that the obvious extension of the contours to J082042.4+205715 can, to first order, be explained by point spread function (PSF) degradation due to its off-axis location in the *Chandra* ACIS-I field-of-view (cf. Table 2.3). The other objects appear compact, consistent with a point-like source on axis.

In order to best determine whether the sources are truly point-like or extended, it is necessary to undertake a detailed analysis of the PSF of each of the sources. In

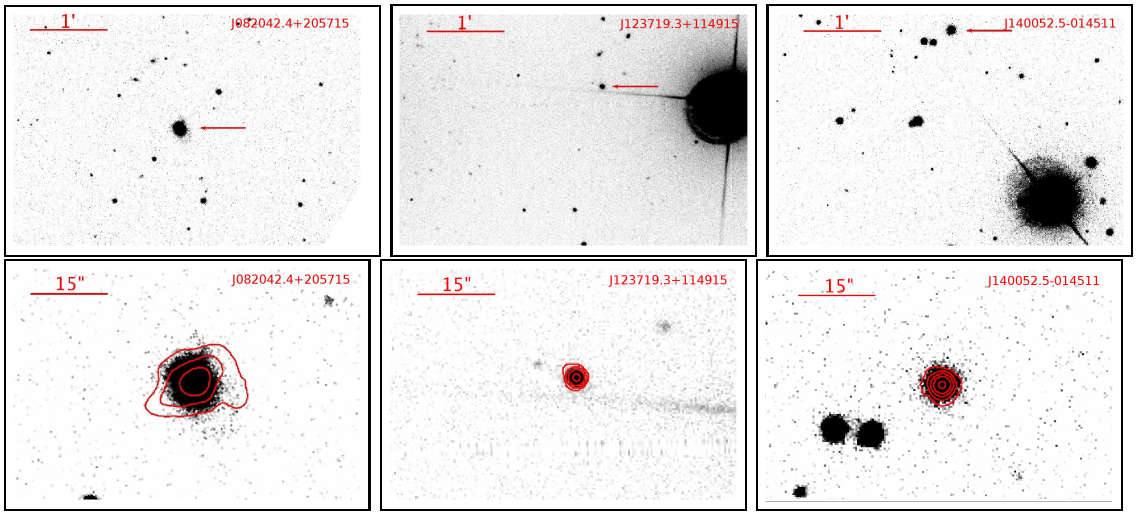

Figure 2.3: *Top row*: From left to right, *SDSS* R-band images containing the three sources J082042.4+205715, J123719.3+114915, and J140052.5-014510 respectively. The objects that are the focus of this chapter are indicated. J082042.4+205715 is located $\sim$ 7 arc minutes to the south of NGC 2563, the central galaxy of the NGC 2563 group of galaxies (e.g. Mulchaey et al. 2003), although our object is clearly located in the background to this nearby ($d \sim 60$ Mpc) group. The other objects are in emptier fields, although both are located close to the line-of-sight to nearby, bright K0 stars. J123719.3+114915 is $\sim$ 1.5 arc minutes east of the $m_V \sim 8$ star HD 109771, and J140052.5-014510 $\sim$ 2.5 arc minutes north-east of the $m_V \sim 9.4$ star HD 122238. The double source to the immediate south-east of J140052.5-014510 is a pair of point-like objects with equal magnitudes ($g = 17.2$), recorded as J140053.49-014520.6 and J140053.97-014519.6 in the *SDSS* catalogue. According to the *SDSS*-DR7 catalogue, these two objects have photometric redshifts of $\sim 3\times 10^{-4}$ and 1×10^{-3}, respectively. *Bottom row*: Close up images of the three sources, in the same order as above, overlaid with X-ray contour plots. The contour levels start at 0.09 count pixel^{-1}, with each successive contour representing a count density a factor $\sim 2.6, 4$ and 5.2 higher than the last (left – right across the three images). The optical data are displayed as above, and the X-ray data has been smoothed with a 1-pixel gaussian kernel for display purposes.

order to do this, we first simulated the PSF of point-like sources with the same flux and off-axis angles as our objects. These simulations require the use of both the *Chandra* ray tracer, CHART [8], and the MARX [9] simulator. Firstly, we use CHART to produce a series of simulated monochromatic PSFs, ranging over the 0.3 – 10 keV range, with appropriate fluxes and positions with respect to the detector axis. These PSFs are the result of ray-tracing through the *Chandra* HRMA X-ray optics, and still require projecting onto the detector plane (taking account of the detector response). This functionality is provided by MARX, which we therefore use to complete the simulation process. We then compare these simulated PSFs to the actual data using the CIAO SRCEXTENT script[10]. This uses a Mexican Hat Optimisation algorithm to determine a 'size' – effectively an average radius – for each PSF, and directly compares the two. We show the results from SRCEXTENT in Table 2.4 for the real data, and the simulated monochromatic PSF at 1 keV.

As Table 2.4 shows, the observational data does not appear extended with respect to the simulated data at 1 keV (chosen as an illustrative example as it is close to the peak of the *Chandra* effective area). Indeed, none of the simulated PSFs (over the typical ACIS energy range) appeared significantly narrower than the observational data. [In fact, we note that in most cases the simulated PSFs appeared slightly broader, although the PSFs generally agreed at about the 90% error level.] From the measured extents, we have deduced that the physical sizes of the X-ray sources are constrained to within ~ 6.5 kpc for J082042.4, and to within ~ 1.2 kpc for both J123719.3 and J140052.5. It is worth noting that the compact nature of at least two of these sources does not rule out the presence of star formation within the galaxies' nuclei. It is possible for compact nuclear star formation to be occurring on less than kpc scales, given the distances of the sources.

[8] `http://cxc.harvard.edu/chart`
[9] `http://space.mit.edu/CXC/MARX/`
[10] `http://cxc.harvard.edu/ciao/threads/srcextent/`

Table 2.4: Observed source PSF and simulated (1 keV) PSF details from SRCEXTENT.

Source ID (2XMMp...)	Obs. ID	PSF size[a] (arcsec)	Source size[a] (arcsec)	Source size (kpc)
J082042.4+205715	7925	2.91±0.35	$2.55^{+0.29}_{-0.30}$	$6.49^{+0.74}_{-0.76}$
J123719.3+114915	9558	0.49±0.04	$0.47^{+0.06}_{-0.07}$	$1.20^{+0.15}_{-0.18}$
J140052.5-014510	9557	$0.50^{+0.01}_{-0.02}$	0.45±0.03	1.15±0.08

Note: [a] The Mexican hat optimisation algorithm employed by SRCEXTENT fits a 2-D elliptical Gaussian to the PSF; the 'size' quoted is calculated as $\sqrt{(1/2)(a^2+b^2)}$, where a and b are the semi-major and semi-minor axes of the elliptical Gaussian respectively. The errors are quoted at the 90% confidence level.

2.4.2 Intra-observational variability

A second key distinction between AGN activity and large star formation regions can be made on the basis of their short-term variability. A large, spatially extended region composed of many individual X-ray sources will not vary coherently on short timescales (i.e. within a single X-ray observation, typically less than a day). A compact object like an AGN, on the other hand, may readily vary on timescales of hours (e.g. Lawrence et al. 1987; Markowitz et al. 2003; Smith & Vaughan 2007). We therefore analysed the lightcurve of each observation to search for short-term variability.

Using the background-subtracted lightcurves, we employed a χ^2 fit to test whether the X-ray data are variable against a constant count rate hypothesis. To improve statistics, the EPIC-pn and MOS data were co-added for each observation before testing. All but one of the datasets were found to show no strong evidence for short-term variability, consistent with a constant count rate during each observation. The exception was observation 9557 for J140052.5-014510, which returned a null hypothesis probability of < 0.001 for a constant count rate. We show the lightcurve for this observation in the upper panel of Figure 2.4. In it, the count rate can be seen to drop by a factor of ~ 2 and then rise back to its previous value within a matter of ~ 6 hours. This implies that at least 50% of the X-ray emission from this source originates in a region that is no more than ~ 6 light-hours across, consistent with the central regions of an AGN.

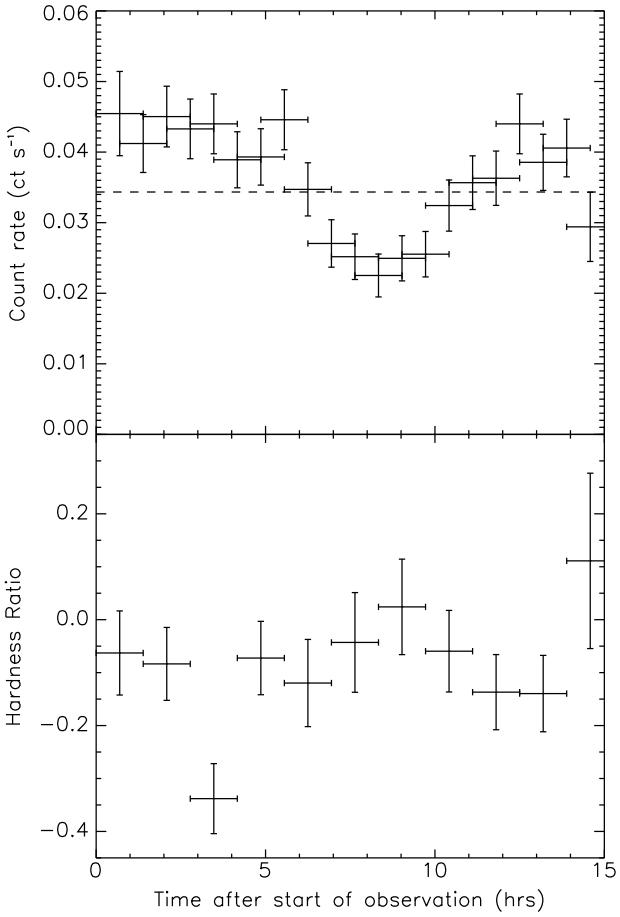

Figure 2.4: *Upper panel:* Lightcurve of the ACIS-S observation of J140052.5-014510 (Obs ID 9557). The horizontal dashed line represents the best fitting constant count rate over the whole observation. A 'dip' in the count rate is clearly visible between $\sim$ 20 and 40 ks into the observation. *Lower panel:* Hardness ratio as a function of time after the start of the observation, for the same observation.

We investigate the nature of this 'dip' in the lightcurve further in the lower panel of Figure 2.4, where we display the evolution of the hardness ratio during the count rate dip. To calculate this, we split the data into two bands, a 0.3 – 1.2 keV soft band (S) and a 1.2 – 10 keV hard band (H), and derived lightcurves in both, on twice the binning of the original lightcurve to maintain good statistics. We then combined these into a hardness ratio as $HR = (H - S)/(H + S)$, with errors calculated as per Ciliegi et al. (1997). The figure shows that, other than a significant softening in one bin (between 10 and 15 ks into the observation), the hardness of the data remains roughly constant. This includes the period of the dip (roughly 20 - 40 ks) – although the data points suggest a slight hardening in this period, it is not statistically significant. This lack of strong spectral hardening implies that the dip is probably not originating in a simple increase in absorbing column, lasting for several hours. Instead, it might have one of two alternative origins; either it is an intrinsic fluctuation in the output of the compact region, or it is the result of a Compton-thick medium passing in front of the X-ray emission region and (at least) partially obscuring it.

2.4.3 Spectral results

The third diagnostic test we apply to the data is to analyse the X-ray spectrum of each dataset. Although AGN are now known to display very complex spectral phenomenology in the soft X-ray regime including warm absorbers (e.g. Blustin et al. 2005) and soft excesses (e.g. Gierliński & Done 2004), in the absence of high quality data their spectra are still commonly fitted with simple power-law models (e.g. in deep surveys, Alexander et al. 2005). Starburst regions also have complex spectra (see e.g., Pietsch et al. 2001; Read & Stevens 2002), but, in addition to a strong continuum, these are dominated by relatively narrow emission lines from hydrogen-like and helium-like charge states of the abundant low-Z elements that are present in the hot gas energised by the starburst processes, typically modelled with an optically thin, thermal spectrum with multiple temperature components (e.g., Moran et al. 1999; Jenkins et al. 2004; Warwick et al. 2007). Crucially, these components are detectable even in moderate quality *XMM-Newton* data (e.g.

Franceschini et al. 2003; Jenkins et al. 2004), providing a test of whether the starburst dominates the X-ray emission.

The spectra were analysed using XSPEC version 11.3.2 (Arnaud 1996). For the *XMM-Newton* datasets we had three separate spectra for each observation of each source (one from the pn camera, and two from the MOS); these were analysed simultaneously, with a constant coefficient inserted to model calibration uncertainties between the detectors. The value of this coefficient was fixed to 1.0 for the pn, and allowed to vary in the fits to the MOS data. In practise, the value of this constant varied by no more than $\pm 10\%$ between detectors in the majority of observations.

As noted in Section 2.3, most fits were performed using the standard XSPEC χ^2 minimisation techniques. However, some of the data were so poor they did not meet the Gaussian criteria for χ^2 fitting; consequentially we used the Cash statistics option in XSPEC to perform maximum likelihood fitting to these data. Cash statistics was only used on observations 7925, 9558, and 0112840101. We began by analysing the background spectrum for each source. For the *Chandra* data we constrained its form by fitting a simple power-law continuum model to it, using the Cash statistics option in XSPEC (i.e., "cstat"). In the case of the *XMM-Newton* data in observation 0112840101, we examined only the pn data as the datasets were heavily background-dominated, and the MOS cameras only contributed $\sim$ 20 - 30 source counts each. The background data had sufficient statistics to use χ^2 fitting, and required a broken power-law plus a narrow Gaussian component to produce a good fit. The source data itself was then analysed, but not background subtracted. Instead, the results of the fit to the background spectrum were added as a fixed component to the spectral model, scaled appropriately for the relative aperture sizes. The model fitting was then performed using Cash statistics. The quality of the fit was evaluated using the 'goodness' command, which we set to compare the obtained C-statistic value to 1000 Monte-Carlo simulations based on the best fitting model, and provides a percentage of simulated datasets with a C-statistic value lower than that obtained in the fit.

The spectral fitting was conducted using a very basic absorbed power-law continuum model. The precise combination of models utilised was TBABS*ZTBABS*ZPO

in XSPEC syntax, where the TBABS component represents the foreground absorption column in our own Galaxy, the ZTBABS is the absorption column local to the X-ray source (and hence redshifted), and the ZPO is the redshifted power-law continuum. The foreground Galactic absorption was set to a fixed value, calculated using the NRAO dataset of Dickey & Lockman (1990) in the COLDEN Galactic hydrogen column density calculator within the *Chandra* Proposal Planning Toolkit[11], and shown for each galaxy in Table 2.1. The redshifts were derived from *SDSS* data, and are also listed in Table 2.1. For both the Galactic and intrinsic absorption columns, the abundance levels are set as per Wilms, Allen and McCray (2000). We show the result of these fits in Table 2.5. The errors quoted in Table 2.5 are the 90% errors on the model parameters for one interesting parameter, and the 68% errors for the fluxes. As an example of the data quality, we show the four spectra from observations of J140052.5-014510 in Figure 4.2.

All the χ^2 fits provide statistically acceptable explanations of the data with a simple absorbed power-law model (null hypothesis probability > 0.05). The goodness criteria for both fits of J123719.3+114915 are also acceptable; however we note the Cash statistics fit to the 7925 data for J082042.4+205715 has a poor goodness (99% of simulated power-law datasets providing a better Cash statistic). However, the data for this model is too poor to attempt more complicated fits.

Table 2.5 shows that each of the sources displays a very distinct spectrum. J082042.4+205715 has a relatively hard slope, with $\Gamma \lesssim 2$, but has little intrinsic absorption with a column $\lesssim 10^{21}$ cm^{-2}. J123719.3+114915 appears very hard with a power-law slope $\Gamma < 1.6$, although its absorption column appears inconsistent between the two observations. Finally, J140052.5-014510 has both a very low absorption column of $\lesssim 5 \times 10^{20}$ cm^{-2}, and the softest spectrum with, $\Gamma \geq 2$. Note that all the spectral fits in Table 2.5 are shown in chronological order (see Table 2.3 for observation dates).

Although the power-law models provide reasonable fits to the data, we examined whether there was any evidence for further spectral complexity by the addition of

[11] `http://cxc.harvard.edu/toolkit/colden.jsp`

Table 2.5: Results of fitting the spectral data with an absorbed power-law model.

Source/Obs ID	$N_{\rm H}$	Γ	χ^2/dof	C-stat/%	EPIC-pn flux	ACIS flux
(1)	(2)	(3)	(4)	(5)	(6)	(7)
2XMMp J082042.4+205715						
0108860501	< 10.9	$1.62^{+0.22}_{-0.19}$	36.5/42		$1.29^{+0.31}_{-0.13}$	
7925	< 8.2	$1.94^{+0.15}_{-0.25}$		554.1/99		$1.63^{+0.02}_{-0.14}$
0505930301	< 4.5	$1.73^{+0.08}_{-0.04}$	209/220		$2.23^{+0.11}_{-0.12}$	
2XMMp J123719.3+114915						
0112840101	< 10.3	$0.48^{+0.29}_{-0.26}$		1180/69	$1.21^{+0.26}_{-0.19}$	
9558	$82.0^{+82.1}_{-50.2}$	$1.12^{+0.55}_{-0.48}$		343.8/50		$0.44^{+0.07}_{-0.17}$
2XMMp J140052.5-014510						
0200430901	< 3.5	$2.31^{+0.22}_{-0.18}$	25.1/24		$1.95^{+0.16}_{-0.35}$	
0505930101	< 4.1	$2.59^{+0.15}_{-0.11}$	168/169		$2.27^{+0.14}_{-0.08}$	
0505930401	$4.5^{+5.1}_{-3.8}$	$2.74^{+0.28}_{-0.20}$	111/97		$1.13^{+0.08}_{-0.11}$	
9557	< 5.2	$2.06^{+0.13}_{-0.10}$	105/85			$2.34^{+0.16}_{-0.1}$

Columns: (1) Source name, and observation ID for the spectral data. (2) Absorption column density intrinsic to the source ($\times 10^{20}$ cm^{-2}). An additional foreground Galactic column (as per Table 2.1) is also applied and held fixed in the fit. (3) Power-law photon index. (4) χ^2 value and number of degrees of freedom for the best fitting model. (5) C-statistic for best fitting model (in the cases where maximum likelihood fitting was used due to the low data quality), with the percentage of Monte-Carlo simulations with a value less than that obtained in the fit to the model. (6) & (7) Observed 0.3 – 10 keV band flux ($\times 10^{-13}$ erg cm^{-2}s^{-1}).

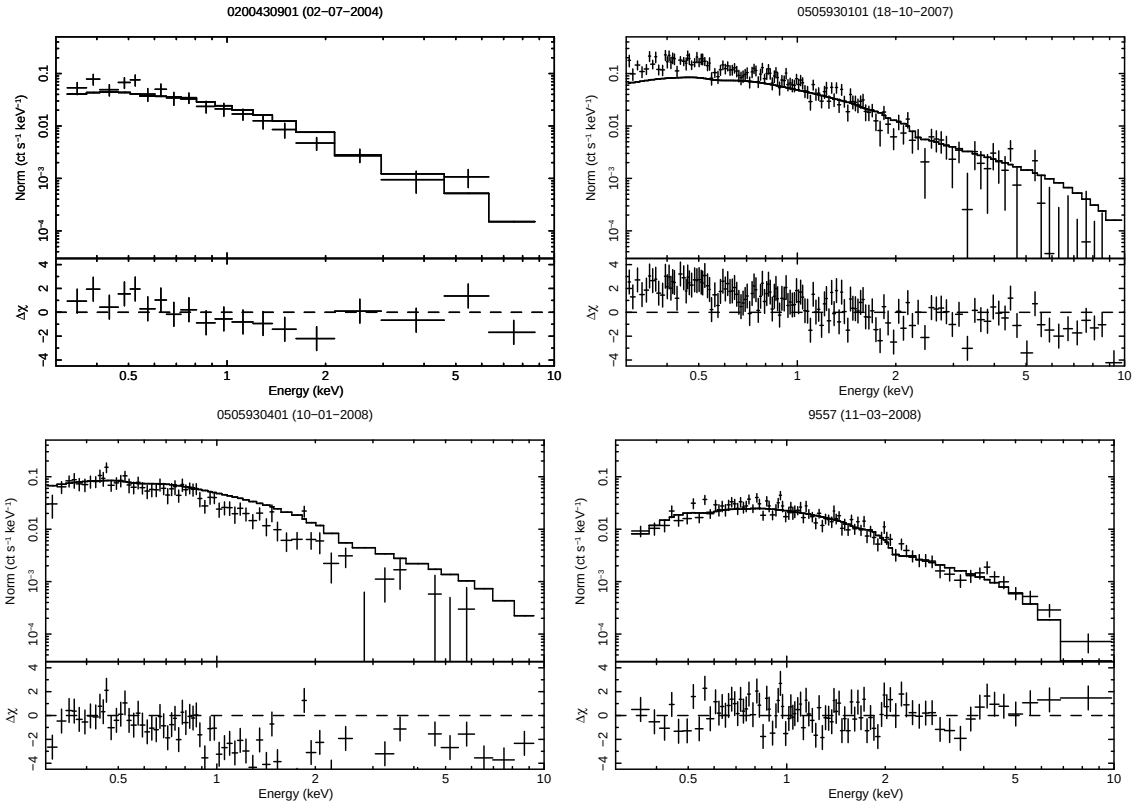

Figure 2.5: The four observed spectra of the source 2XMMp 140052.5-014510, ordered from top left to bottom right by observation date. The top three spectra are from *XMM-Newton* observations (we only show EPIC-pn data for clarity), and the last spectrum is that of the *Chandra* ACIS-S 9557 observation. The four spectra are plotted against the absorbed power-law model best fitting to the *Chandra* data to illustrate changes in the spectrum between different observing epochs. $\Delta\chi$ is plotted underneath the spectra.

further components to the model. We only did this for the better datasets, i.e. those that allowed χ^2 statistics to be used (all observations of J140052.5-014510, and the *XMM-Newton* observations of J082042.5+205715). Given that starburst spectra show strong collisionally-excited emission lines, we started by adding a MEKAL component (Mewe et al. 1985, Mewe et al. 1986, Kaastra, 1992) to each power-law model, setting each MEKAL component to the appropriate redshift and to solar abundance. In all cases, the improvements to the fits were minimal. By setting the MEKAL temperature to 0.6 keV (c.f., Jenkins et al. 2004) and re-fitting for each dataset we were able to place an upper limit on the contribution of a starburst-like MEKAL component to each power-law dominated spectrum. In the case of J082042.5+205715 the 99% upper limit was no more than 5.5% of the total 0.3 - 10 keV flux, whereas for J140052.5-014510 the 99% upper limit was just under 9%. Hence a hot gas starburst component can only be present in the spectra of those two objects at a comparatively minor level.

A separate additional component that may be present in the data is a soft excess, as is found in many AGNs (e.g., Gierliński & Done 2004). We performed similar analyses to those for the addition of a MEKAL, and found no strong evidence for the presence of a soft excess in any dataset (maximum $\Delta\chi^2 < 8$ from the addition of a DISKBB model with two additional degrees of freedom).

A final test we performed on the data was to constrain the presence of a neutral Fe K line. A high ($\gtrsim 1$ keV) equivalent width 6.4 keV Fe K emission line is indicative of the presence of a Compton-thick obscuring torus, blocking the direct line-of-sight to an AGN (e.g. Awaki et al. 1991; Ghisellini, Haardt & Matt 1994). We therefore added a narrow 6.4 keV Gaussian component to the spectra (at the appropriate redshift) and calculated the 99% upper limits on the possible contribution of such a component to each spectrum. We tabulate the results in Table 2.6. Clearly, the data for J140052.5-014510 only rules out a ~ 1 keV equivalent width line in one dataset (9557), and even that still has a rather high equivalent width of ~ 860 eV allowed at the 99% limit. In contrast, the 0505930301 data for J082042.5+205715 places a very stringent 99% upper limit of 140 eV on any possible Fe K line contribution, clearly ruling out a high equivalent width line for this object.

Table 2.6: 99% upper limits on possible Fe K line equivalent widths

Observation ID	Equivalent width limit (keV)
2XMMp J082042.5+205715	
0108860501	< 2.04
0505930301	< 0.14
2XMMp J140052.5-014510	
0200430901	< 12.96
0505930101	< 1.06
0505930401	< 4.85
9557	< 0.86

2.4.4 Long term and spectral variability

Our final set of diagnostics are taken from studying possible variations of both the X-ray flux and X-ray spectral shape between the different observation epochs, which are separated by gaps of months to years. Again, we would expect to see little variation from spatially extended X-ray emission regions composed of many components such as a starburst region, whereas AGN can vary both temporally and spectrally over such timescales (e.g. Taylor, Uttley & McHardy 2003; Sobolewska & Papadakis 2009).

Within the spectral data analysed above we do see evidence for spectral variability between different observation epochs. We illustrate this in Figure 2.5 in which we present the four different spectra of J140052.5-014510 with residuals (pn only in the three *XMM-Newton* datasets, for the sake of clarity), and compare each spectrum to the model best fitting to the Obs ID 9557 *Chandra* data. Clearly the spectra in the top three panels deviate from the shape of the last spectrum, demonstrating some degree of variability in the data. We investigate whether this is due to strong variability in the underlying spectral shape in the top three panels of Figure 2.6, where we compare the measured values of the photon indices between the different observations. It is clear that the best fitting values indicate that the spectrum of J140052.5-014510 does vary significantly, over periods as short as months. It is less clear whether this is the case for the other objects; their power-law photon indices are at least consistent at the 2σ level (or better) over their observations.

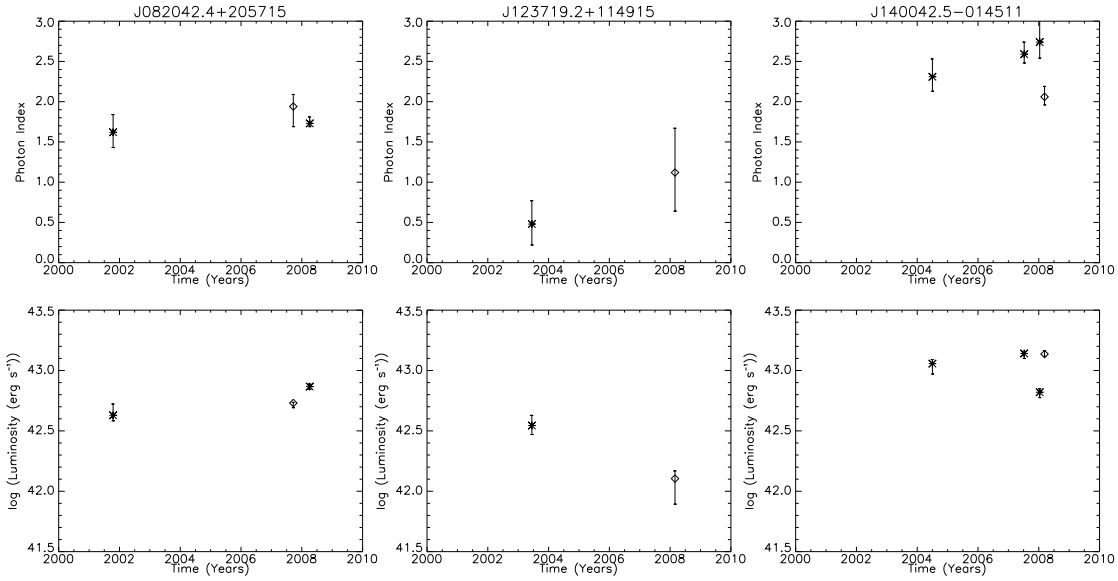

Figure 2.6: Source luminosity and photon index variability in the 0.3 to 10.0 keV X-ray band. The columns show data from (left – right) J082042.4+205715, J123719.3+114915 and J140052.5-014510 respectively. The errors shown are calculated within a 90% Gaussian range. *Top row:* Measured photon index as a function of time. *Bottom row:* Observed luminosity as a function of time. The errors shown are calculated within a 68% Gaussian range. The values are taken from the spectral fits presented in Section 4.3 or calculated as per the text, and each row is plotted on the same scale to permit direct comparison. *XMM-Newton* data points are indicated by asterisks, and *Chandra* data by diamonds.

The long-term luminosity variations are presented as the bottom three panels, where the luminosity is calculated from the fluxes in Table 2.5[12]. All three objects clearly demonstrate significant luminosity variations over timescales of months, consistent with relatively compact objects.

2.5 Discussion

The basic question posed at the beginning of this work was: what can power more than 10^{42} erg s^{-1} of X-ray luminosity from a galaxy with no unambiguous signatures of AGN activity? We have examined this by selecting three galaxies at a redshift ~ 0.1 from *SDSS* for further study at X-ray energies, based on the requisite high apparent X-ray luminosity and an optical spectrum betraying only signs of star formation processes. The work presented in the previous section details the results of several simple tests with the power to diagnose whether the X-ray emission originates in star formation processes, or an AGN.

We find that all three sources appear more consistent with AGNs than starbursts. Firstly, all are point-like in the X-ray images (cf. Figure 2.3; Table 2.4), although this is not convincing evidence in isolation given that the physical size limits on any extended component are of the order $\lesssim 1$ kpc at the distance of the galaxies, permitting at least compact nuclear starburst emission to be present. Far more convincing evidence comes from the time variability characteristics of the X-ray emission, with flux variations of factors $\gtrsim 2$ seen for all three objects (Figure 2.6; Table 2.5) implying that at least 50% of the X-ray luminosity originates in a region no more than a few light-years across. In the specific case of J140052.5-014510, we see its flux halving and then returning to its original value in a period of 6 hours in the *Chandra* ACIS-S lightcurve, implying the X-ray emission originates from a solar system-sized object, which – for a luminosity around 10^{43} erg s^{-1} – has to be due to an AGN. Finally, the X-ray spectra of the three objects are all well-described by

[12]These are the observed 0.3 - 10 keV luminosities, not the rest frame values. However, we note that the similar, low redshifts of the three objects lead to relatively small corrections when converting to rest frame luminosities, with the increases of $\sim 10\%$ for the hard spectrum source J123719.3+114915, and $< 5\%$ for the other two objects.

a power-law continuum, consistent with moderate quality AGN data and not the strong emission line-dominated spectra seen from starbursts. It should be noted that this spectral deconvolution implies dominance by an AGN-like component, but does not rule out a bright X-ray starburst. In fact, the 99% upper limits on the MEKAL thermal plasma contributions to each spectrum still allow for in the region of $\sim 2 \times 10^{41}$ erg s^{-1} of starburst-heated gas in J082042.4+205715 (comparable to the thermal component seen in many ULIRGs, e.g. Franceschini et al. 2003), and up to $\sim 10^{42}$ erg s^{-1} in J140052.5-014510.

So if these objects are all AGN-dominated in the X-rays, can we say anything about the type of AGN from the X-ray data? Firstly, only one of the objects – J123719.3+114915 – appears hard ($\Gamma < 1.6$) and perhaps relatively highly absorbed ($N_{\rm H} \sim 10^{22}$ cm^{-2} during the observation 9558), consistent with a classic type 2 object, although the poor quality of this data should be noted. The other two objects have much lower columns, with both constrained at $\lesssim 10^{21}$ cm^{-2}, more consistent with type 1 AGNs. This is supported when the data are sufficiently good to place constraints on the presence of a neutral Fe K line; in both cases high equivalent width (> 1 keV) lines are ruled out, rejecting a strong reflection component originating in the torus of a type-2 AGN (e.g. Awaki et al. 1991). However, both have different spectral slopes, with J140052.5-014510 markedly softer than J082042.4+205715. While the slope of J082042.4+205715 ($\Gamma \lesssim 2$) is fairly typical for type-1 AGNs (e.g. Nandra & Pounds 1994), the soft slope of J140052.5-014510 ($\Gamma \geq 2$) is more unusual, and consistent with slopes seen in some NL Seyfert 1 galaxies (NLS1s; Vaughan et al. 1999). However, there is no strong evidence of a distinct soft excess – as is seen in NLS1s – in either object. A piece of optical evidence indicating the possible presence of NLS1 activity is the line width of Hβ emission. By definition, NLS1 galaxies emit Hβ with line widths < 2000 km s^{-1} (Wang & Zhang 2007). We found that the three sources emit Hβ at widths considerably lower than this upper limit (< 300 km s^{-1}). However, these line widths are also consistent with those of star forming galaxies.

So why is there no signature of AGN activity in these objects' optical spectra? A number of reasons for this have been suggested in previous work focused on the

nature of so-called 'elusive AGNs', i.e., sources that show no signs of AGN activity in the optical regime, but display signs of AGN activity in the X-ray band. One possibility is that the regions within the galaxy producing narrow and broad line emission typically seen in AGNs have been rendered 'invisible' by obscuration. For example, obscuration of AGN activity within NGC 4945 by a heavy dusty torus was deduced by Iwasawa et al (1993). Obscuration of the narrow line region may also be caused by spherical gas clouds shrouding the nuclei of galaxies, such as PKS 031208 (Comastri et al. 2002). However, obscuration is not necessarily caused by gas and dust close to the galactic nucleus. Rigby et al. (2006) reported that from a sample of 31 AGNs at redshifts of $0.5 < z < 0.8$, only the most face-on galaxies displayed optical AGN activity. This implies that the obscuration of both the broad and narrow line regions may well be caused by host galaxy dust along our line of sight (e.g., Moran et al. 1996; Rigby et al. 2006; Goulding & Alexander 2009). However, given that the X-ray spectral analysis of the three sources yielded hydrogen column density upper limit values $\leq 10^{21}$ cm^{-2}, and that the calculated extinction values from the optical spectra for the galaxies are 1.11 mag $< A_v <$ 2.86 mag, obscuration is unlikely to be the cause for the elusiveness of optical AGN signatures in the sources.

Another possibility is that the BLRs that should be signatures of AGN activity may not be seen because of low accretion rates. According to Nicastro et al. (2000), AGN BLRs may form in disc winds at a critical distance within the accretion disc. This formation occurs at an accretion rate $> 10^{-3}\ \dot{m}$ ($= \dot{M}/\dot{M}_{\rm Edd}$). If the accretion rate is lower than this, the BLR cannot form. A recent study by Trump et al. (2011) deduced that the BLR of an AGN becomes invisible if the accretion rate drops below $10^{-2}\ \dot{m}$. This is because at such low accretion rates, radiatively inefficient accretion flows (RIAFs, Yuan & Narayan 2004) occur and expand close to the inner radius of the accretion disc. RIAFs lack the optical/UV emission of an optically thick accretion disc and therefore cannot ionise BLRs (Yuan & Narayan 2004; Trump et al. 2011).

In order for a source to have an accretion rate lower than $10^{-2}\ \dot{m}$ and to be displaying a luminosity of 10^{42} erg s^{-1}, the mass of the accreting black holes would

have to be $\geq 8 \times 10^7$ $M_\odot$. Using the M-σ relation (Gultekin. et al. 2009) with emission values from the *SDSS*-DR7 archive, we estimated the masses of the black holes in the centre of the sources to be 5×10^8 $M_\odot$, 3×10^7 $M_\odot$, and 2×10^8 $M_\odot$ for J082042.4+205715, J123719.3+114915, and J140052.5-014511, respectively. Therefore, low levels of accretion activity is a possible explanation for the lack of the BLRs in two of the three galaxies' nuclei.

One more possibility is that the AGN activity has been optically diluted by starlight, and indeed star formation signatures, within the host galaxy. Caccianiga et al (2007) found that from a sample of 9 star forming optically elusive galaxies, all of their AGN signatures were diluted by galactic starlight. A similar result was seen in the study of optically elusive AGNs by Trump et al (2009). In this study, 70% of the 48 optically elusive AGN were diluted by galactic starlight. If we investigate the emission-line diagnostic diagram shown in Figure 2.1, we can see that all three sources' flux ratios are positioned in the star forming region. It is likely that star formation in the galaxies has strengthened the Hα and Hβ emission fluxes, thus diminishing the [SII]/Hα and [OIII]/Hβ values. If we remove the galactic star formation signatures, our objects would likely end up within the AGN area of the diagram. Thus, we conclude that the elusiveness of optical AGN signatures within our galaxies is most likely due to dilution by stellar activity.

Our results are similar to those of Jia et al. (2011), where they investigate X-ray, optical, and infra-red properties of 6 Lyman break analogue (LBA) galaxies with optical line ratios similar those of our sources. They deduced that a combination of intense star formation and AGN activity is likely present within the LBAs by studying their multi-wavelength properties. Unlike the work of Jia et al., we were able to deduce AGN presence by looking at X-ray data alone, due to the superior quality of our X-ray data. Nevertheless, both our results and those of Jia et al. agree on the presence of AGN activity and star formation within both galaxy samples.

2.6 Summary

Surveys have revealed a class of object displaying both high X-ray luminosities ($L_{\rm X}$ $> 10^{42}$ erg s^{-1}), and a lack of a discernible active galactic nucleus (AGN) in the optical band. If these sources are powered by star formation activity alone, they would be the most extreme X-ray luminosity star forming galaxies known. We have investigated the mechanism driving the X-ray luminosities of such galaxies by studying the X-ray emission of three moderate redshift (z $\sim$ 0.1) examples of this class, selected from a cross-correlation of the *SDSS*-DR5 and 2XMMp-DR0 catalogues. X-ray spatial and long-term variability diagnostics of these sources suggest that they are compact X-ray emitters. This result is supported by the detection of rapid short term variability in an observation of one of the sources. The X-ray spectra of all three sources are best fitted with a simple absorbed power-law model, thus betraying no significant signs of the hot ISM associated with star formation. These results indicate that the X-ray emission is powered by AGN activity. But why don't these sources display optical AGN signatures? We argue that the most likely explanation is that the optical AGN emission lines are being diluted by star formation signatures from within their host galaxies.

Chapter 3

Constraining the ages of X-ray sources in NGC 922

3.1 Introduction

Collisional ring galaxies are galactic systems that are identified by a clearly visible ring, or partial ring, of recent star formation. The morphology of these systems was first noted by Burbidge & Burbidge (1959) in their study of the galaxy NGC 2444/5 (Arp 143; c.f., Figure 3.1). They suggested the knotty ring-like structure to be the result of a collision between an elliptical (specifically the elliptical structure to the north of the galaxy), and a spiral galaxy. Similar interpretations of the ring-like morphology of this type of system have been made by a number of authors based on subsequent observations (e.g., Lynds & Toomre 1976; Freeman & de Vaucouleurs 1974). On investigating the binary ring galaxy II Hz 4, Lynds & Toomre (1976) deduced that the morphology of the galaxy was likely produced as a result of a gas-poor companion galaxy cleanly passing through a galaxy with a disc-like morphology. The authors found the nucleus of the target galaxy to be off-centre, and argued that this could be the result of an asymmetric collision. A different interpretation of the morphology of these galaxies was put forward by Freeman & de Vaucouleurs (1974), who argued that the ring-like appearance of these systems could be the result of a collision between a normal spiral galaxy and a massive ($M \sim 3 \times 10^9 M_\odot$) intergalactic HI cloud.

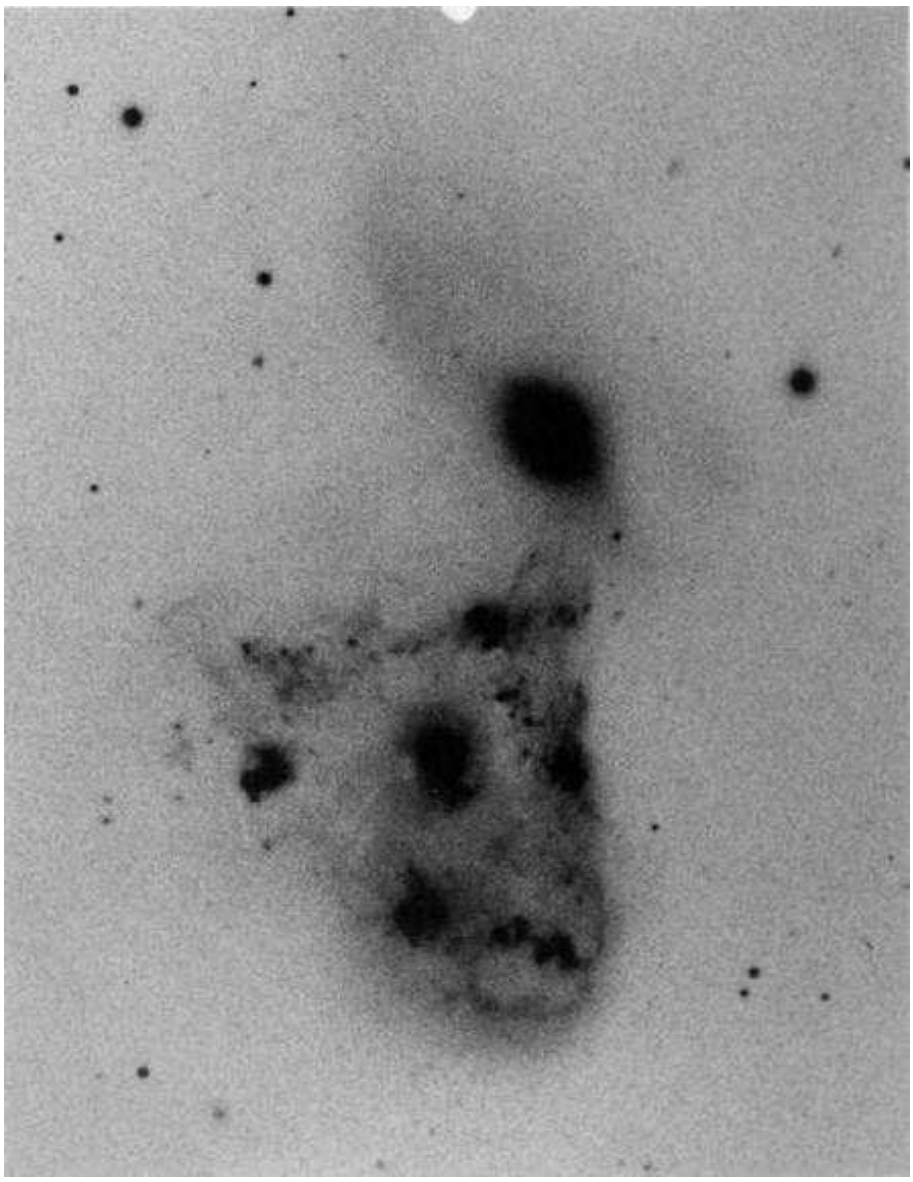

Figure 3.1: An image of Arp 143, taken from the Atlas of Peculiar Galaxies (Arp 1966). The observation was taken by the 200-inch Hale telescope at the Palomar observatory.

Several authors have studied the formation and evolution of collisional ring galaxies. Using observational data from a small sample of these systems, Theys & Spiegel (1976) proposed that collisional ring galaxies could be divided into three sub-classes: RE, RN, and RO galaxies. According to this classification scheme, RE galaxies are ring systems that possess crisp, empty rings, RN galaxies are systems that possess similar rings, but that also have off-centre nuclei, and RO galaxies are systems that possess rings that are not crisp, but instead have knots or condensations within them. From photometric analysis, the authors deduced that the galaxies in their sample have masses $\sim 10^{11}$ $M_{\odot}$ and ages $\sim 10^{8}$ years. They also found that the majority of their sample have companion galaxies, located preferentially on the minor axes of the galactic rings. Given their photometric and visual findings, they concluded that the rings in this type of system were formed as the result of a collision between the disc of a normal galaxy and a smaller companion, thus agreeing with the findings of Burbidge & Burbidge (1959) and Lynds & Toomre (1976). In a similar study, Few & Madore (1986) proposed another classification model for collisional ring galaxies, based on observational analysis from a much larger sample. They proposed that these galaxies can be divided into 2 classes, P-types and O-types, where P-type galaxies are objects that display knotty ring structures, (often) displaced nuclear regions, and a statistically significant excess of companions falling within ~ 2 ring diameters of the galaxy, and O-type galaxies are those that possess smooth ring structures and centrally located nuclei.

As well as observational studies, several authors have employed the method of N-body simulations in an attempt to understand the mechanisms necessary in the formation of galaxies with such unusual morphologies, as well as to understand the how the galactic rings evolve with time. Further to their work in 1976, Theys & Spiegel (1977) predicted the dynamical evolution of rings by simulating the passage of a spherical galaxy through the disc of a normal galaxy. Their results indicated that the visible ring-like morphology of these galaxies is caused by a density wave of gas propagating through the disc of the galaxy as a result of the collision. They also noted the possibility of the formation of more than one ring, given the correct collision parameters. As well as the ring-like density wave, their simulations also

predicted the presence of the original core region within the disc galaxy. The authors noted that this makes it difficult to interpret the existence of RE-type galaxies, as classified in their previous work, unless the target galaxy loses core mass to the intruder. If mass is lost from the core during the collision, the simulations predicted that the core of the disc galaxy should disperse. Another result was that the rings in these systems have a predicted lifetime $\sim 10^8$ years, after which they suffer the effects of bead instabilities (Dyson 1893), such as those likely to have been experienced by the Klemola 25 galaxy group (Danks & Materne 1984). These predictions agreed with the age estimates made by the authors in their previous observational work. In a more sophisticated analysis of collisional ring galaxies, Huang & Stewart (1988) performed several simulations of galaxy collisions, including the effects of self-consistent galactic halos, assuming a number of different impact positions and angles. Throughout these simulations, the authors assumed a disc-to-halo mass ratio of 2 for the target galaxy, and a companion-to-target mass ratio of 0.4. Among their results, the authors found that a collision at the centre of the target galaxy with an impact angle $> 60^\circ$ to the galactic disc barely effects the position of the galactic nucleus. However, an off-axis collision, a collision at a lesser angle, or combination of the two, could result in the nucleus of the target galaxy merging with part of the newly formed ring. They also found that a collision at the centre of the target galaxy at an angle of 45° is the most disruptive to the target disc. In a similar study by Athanassoula et al. (1997), it was found that the more massive the companion galaxy passing through the disc of the target, the larger the amplitude, the higher the expansion velocity, and the longer the lifetime of the resulting density wave. More recently, Puerari & Anguilar (2009) investigated the formation of rings in these galactic systems. By performing a combination of self-consistent modelling and numerical simulations, the authors deduced a number of results that had not been previously reported. For example, they saw that a high velocity impact implied the propagation of rings through the galactic disc at a constant velocity. Also, they found that collisions that occur perpendicular to the galaxy, peripheral to the galactic centre, are effective at both displacing the target nucleus, and creating an inclined ring that remains so for extended periods of time

($\sim 10^8$ years).

Despite the general agreement that the rings in these galactic systems are formed as the result of a collision between a target galaxy and a smaller companion, a number of these systems have been detected without the obvious presence of a companion galaxy (e.g., Few & Madore 1986; Jeske 1986). Luban-Lotan & Struck-Marcell (1989) explored the possibility that a companion can be captured during a collision under the right physical circumstances. Using N-body simulations, they found that dynamical friction could potentially be responsible for a capture, given the correct collision parameters. They also argued that if a companion collides with, and subsequently passes through, the centre of a massive galactic bulge, then sizable dynamical friction and tidal forces resulting from the collision may lead to the capture of the companion.

Over the last ~ 4 decades, a considerable amount of theoretical and observational evidence has been found for enhanced levels of star formation in collisional ring galaxies. It was proposed in the late 70's and early 80's that galaxies with near-by companions experience high levels of star formation (e.g., Larson & Tinsley 1978; Joseph et al. 1984). Appleton & Struck-Marcell (1987a) noted that in a sample of 26 collisional ring galaxies, the average $L_{\rm FIR}/L_{\rm B}$ was higher than that expected in normal galaxies, suggesting the presence of high levels of star formation. In an effort to explain this phenomenon, Appleton & Struck-Marcell (1987b) performed an investigation using the method of cold fluid modelling. Among the results of this study, the authors found that if a collisional density wave propagates at a velocity similar to that of the initial impact, then both enhancement and suppression of star formation can occur. The authors explained that the enhanced formation occurs as a result of strong compression and, hence, the formation of unusually large gas clouds at the leading edge of the density wave. They also explained that the suppression occurs when the gas clouds pass through the density wave into a rarefaction region, and break up as a result. In the same study, Appleton & Struck-Marcell (1987b) predicted the formation of a second density wave within the disc of the target galaxy, similar to the formation of the first wave. The authors argued that the material being propagated outwards by this wave would collide with material falling inwards behind

the initial density wave. The resulting compression of material in the secondary wave would then lead to an enhancement of star formation activity. They also argued that this mechanism may be the cause of strong starbursts in collisional ring galaxies. Further to this work, Struck-Marcell & Appleton (1987) performed numerical modelling, this time focusing on target galaxy discs with both a high mass and a high density of gas clouds. They found that even the collision of a low mass companion with such a disc could initiate a sustained burst of star formation in the galaxy, due to the effects of pressure on gas elements.

Observational evidence has been reported that the ongoing star formation in these systems is concentrated in the rings more so than in any other regions of the galaxies. In a Hα and IR study of a sample of collisional ring galaxies, Marston & Appleton (1995) reported that star formation almost exclusively confined to the galactic rings. A multi-wavelength ($BVRJHK$) observational study of the same sample of galaxies conducted by Appleton & Marston (1997) yielded results agreeing with those of Marston & Appleton (1995). Furthermore, it was noted by Appleton (1999) that starburst population models indicate that most knots in rings are dominated by young stellar populations.

Among the population of collisional ring galaxies is NGC 922, a peculiar high-metallicity ($Z \sim Z_{\odot}$, Wong et al. 2006) galaxy with a distinctive C-shaped ring of optical and Hα emission (see Figure 3.2). The galaxy was initially described by Block et al. (2001) as a disc-obscured grand design spiral. However, a more recent study by Wong et al. (2006) presented compelling evidence that the morphology of NGC 922 can be explained by an off-centre collision between a spiral galaxy and a dwarf companion located $\sim$ 8 arc minutes away. This explanation is supported by the presence of the stellar plume that is seen to connect the 2 galaxies (Wong et al. 2006).

As part of a study comparing the effects of metallicity in the formation of ULXs and XRBs, Prestwich et al. (2012) performed an investigation of the X-ray point source population in the galaxy NGC 922. This particular galaxy was selected for this study based on a number of factors including likely X-ray brightness, which was suggested by the high star formation rate (8 $M_{\odot}$ yr^{-1}) of the galaxy. Another factor

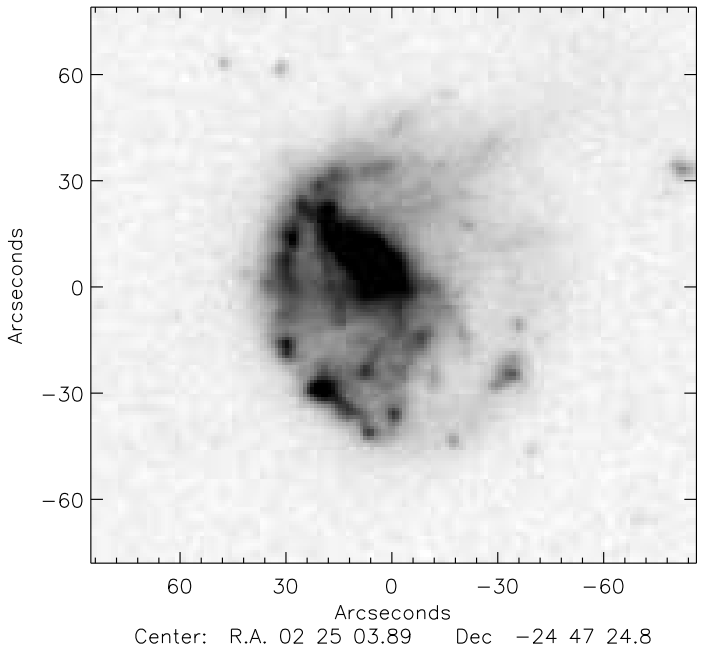

Figure 3.2: A *Digital Sky Survey* red-band image of the collisional ring galaxy NGC 922. The C-shape morphology of the galaxy is apparent in this image.

in the selection of NGC 922 was that the galaxy is relatively close, thus allowing for better spatial resolution and sensitivity in both X-ray and optical observations. In this study, Prestwich et al. (2012) reported the presence of 14 point-like X-ray sources within NGC 922, a number of which were seen to display X-ray luminosities within the ULX regime (i.e., with X-ray luminosities $\geq 10^{39}$ erg s^{-1}). Stellar population synthesis models (e.g., Belczynski et al. 2008) suggest that such ULXs (i.e., ULXs located in high metallicity star forming environments) are HMXBs. As part of their study, Prestwich et al. (2012) compared the luminosity function of the sources in NGC 922 with that of the sources within the less metal-rich ($Z \sim 0.3Z_{\odot}$, Fosbury & Hawarden 1977; Wolter & Trinchieri 2004) Cartwheel galaxy. They found that both luminosity functions were shaped like a power-law with a slope of ~ 0.8, and that the overall number of X-ray sources in each system scaled with star formation rate. They noted that these results match the predictions of the X-ray binary population models of Linden et al. (2010), assuming the correct metallicity levels and galaxy ages.

Several authors have inferred from observational evidence that a relationship exists between HMXBs and young stellar clusters. HMXBs in a number of local galaxies have been located either close to, or coincident with, star clusters (Zezas et al. 2002; Kaaret et al. 2004; Rangelov et al. 2011). Such a close proximity suggests that the HMXBs were actually formed within these clusters. Another point of evidence for the formation of HMXBs in stellar clusters is the high fraction of massive stars both in our own Galaxy (de Wit et al. 2005), and in the Antennae galaxy (Fall et al. 2005) that were formed in these stellar systems.

Although several Galactic and extra-Galactic HMXBs are known to coincide with young stellar clusters, most are located too far from a cluster to directly infer an association. However, this does not disprove the hypothesis that HMXBs were formed within clusters. One possibility is that these XRBs were ejected from their parent clusters via kicks from SN explosions or dynamical interactions with stars in dense cluster cores (McSwain et al. 2007). Another possibility is that the parent clusters have dissolved over time.

The ages of X-ray binaries are an important parameter in the modelling of X-ray

binary formation and evolution (Linden et al. 2010). To this end, we have taken the work of Prestwich et al. (2012) a step further by constraining the ages of the X-ray sources in NGC 922, using both the optical continuum of star clusters and emission lines from gas within the galaxy. The work in this chapter is presented as follows: Section 3.2 gives a summary of the properties of the X-ray source population in NGC 922, as per the work of Prestwich et al. (2012). The optical observations of NGC 922 used in this work are presented in Section 3.3. This section includes how the optical cluster counterparts to the X-ray sources were detected, and the locations of the X-ray sources relative to the counterparts and to Hα emission. The age constraints of the optical counterparts and how these constraints were obtained are presented in Section 3.4. The results of our analysis are discussed in Section 3.5. Included in this section is a discussion of the nature of the X-ray sources, as well as a brief discussion of the relationship between ULXs and recent star formation. Finally, Section 3.6 briefly summarises the work presented in this chapter.

3.2 Summary of the X-ray sources in NGC 922

The X-ray data used by Prestwich et al. (2012) was obtained from two 0.2 – 10 keV band *Chandra* observations of NGC 922 (observation IDs 10563 and 10564, PI: A. Prestwich). We have used the same observations to further investigate the properties of the X-ray source population in the galaxy. The basic information on these observations can be seen in Table 3.1. The first observation was taken on March 5, 2009, and has an exposure time of $\sim$ 30 ks. The second observation, which has the considerably shorter exposure time of $\sim$ 10 ks, was taken on October 2, 2009.

Prestwich et al. (2012) reported the presence of 14 point-like X-ray sources within NGC 922, all of which were seen to display luminosities suggestive of XRB accretion (Fabbiano 2006). We have subsequently identified one of these sources as a background galaxy, and have excluded it from our sample. The basic properties of the remaining 13 sources, as observed by Prestwich et al. (2012), can be seen in Table 3.2. The source flux values were estimated within a 0.5 – 8 keV range,

Table 3.1: Basic information on the X-ray and optical observations used in this work

Observatory	Instrument	Obs. ID	Band		Band filter[(1)]	Exposure
			(keV)	(nm)		(ks)
Chandra	ACIS-S	10563	0.2 – 10	-	-	30
Chandra	ACIS-S	10564	0.2 – 10	-	-	10
HST	WFPC2	11112	-	300	W	1.1
HST	WFPC2	11112	-	439	W	1.1
HST	WFPC2	11112	-	547	M	1.1
HST	WFPC2	11112	-	814	W	1.1
HST	WFC3	11836	-	665	N	6.7
HST	WFC3	11836	-	621	M	1.6

[(1)] *HST* band filter, where W = Wide band filter, M = Medium band filter, and N = Narrow band filter.

assuming a simple absorbed power-law model with a photon index of $\Gamma = 1.7$ as per the results of Swartz et al. (2004), and a Galactic foreground absorption column density of $N_{\rm H} = 1.6 \times 10^{20}$, for the spectra of the sources. Using XSPEC, the authors obtained the flux values by setting the normalisation of the power-law model to match the observed count rates of the sources. Source luminosity values were then calculated assuming a distance of 48 Mpc.

In this work, we have extended the analysis of Prestwich et al. (2012) by investigating the spectral properties of the sources in NGC 922. We conducted this investigation using data from observation 10563, since the exposure time of this observation is considerably longer than that of observation 10564. Despite the longer exposure, the majority of sources displayed very few photon counts during this observation. Therefore, we did not perform standard spectral analysis on the sources. Instead, we adopted 2 methods commonly used in the analysis of sources displaying few photon counts: X-ray colour analysis (Prestwich et al. 2003), and quantile analysis (Hong et al. 2004). In the X-ray colour analysis of the sources, we defined the 'soft' and 'hard' colours as (M-S)/(H+M+S) and (H-M)/(H+M+S), as per Prestwich et al. (2003), where H, M, and S are the number of source photons observed in the soft (0.5 – 1 keV), medium (1 – 2 keV), and hard (2 – 8 keV) bands, respectively. The source colours are shown in Figure 3.3. The curves in the same panel represent theoretical colour predictions of power-law (black), disc blackbody (blue),

Table 3.2: Basic properties of X-ray sources in NGC 922

Source	RA	Dec	Net count rate		$f_{\rm X}$ (March 09)	$L_{\rm X}$ (March 09)
			March 09	Oct 09		
	(J2000)		(ct s^{-1})		(10^{-15} erg cm^{-2} s^{-1})	(10^{39} erg s^{-1})
1	02:25:06.50	-24:47:17.1	0.30	<0.10	2.5±0.8	0.7±0.2
2	02:25:05.76	-24:47:01.7	1.57	2.04	14.0± 2.0	3.9±0.6
3	02:25:05.63	-24:47:52.5	11.47	4.78	87.8±4.6	24.2±1.3
4	02:25:05.28	-24:47:57.4	0.49	1.06	4.3±1.1	1.2±0.3
5	02:25:05.21	-24:47:57.4	0.44	0.80	3.5±1.0	0.9±0.3
6	02:25:05.05	-24:46:53.9	0.21	<0.10	1.9±0.8	0.5±0.2
7	02:25:04.92	-24:47:59.3	1.49	1.00	11.3±1.7	3.1±0.5
8	02:25:04.89	-24:47:10.6	0.44	0.29	3.6±1.0	1.0±0.3
9	02:25:04.02	-24:47:10.6	1.46	11.6	12.1±1.8	3.3±0.5
10	02:25:03.82	-24:47:19.0	1.68	3.28	14.2±1.9	3.9±0.5
11	02:25:03.47	-24:47:57.4	4.08	3.49	31.5±2.8	8.7±0.8
12	02:25:03.33	-24:47:45.7	0.42	0.49	3.2±0.9	0.9±0.3
13	02:25:03.32	-24:47:29.4	0.26	0.21	2.4±0.8	0.6±0.2

Notes: [(1)] Source observed 0.5 – 8 keV flux, estimated using XSPEC and assuming an absorbed power-law model with a photon index of $\Gamma = 1.7$ and a Galactic column density of $N_{\rm H} = 1.6 \times 10^{20}$ cm^{-2}. All errors were calculated within a 68% Gaussian range.

and bremsstrahlung (red) models. Unabsorbed model predictions are represented by the dashed curves, with photon index, inner disc temperature, and bremsstrahlung temperature values ranging from $\Gamma = 0 - 4$, $kT_{\rm in} = 0.1 - 10$ keV, and $kT_{\rm gas} = 0.1 - 7$ keV, respectively. Predictions of the same models with the addition of an absorption component are represented by the solid curves. In all 3 cases, the absorption column density ranges from $N_{\rm H} = 0 - 10^{23}$ cm^{-2}, with increasing absorption indicated by the direction of the arrows in the figure. The statistical uncertainties on both the hard and soft colours of the XRBs do not allow us to make any definitive statements about the nature of the sources.

One of the major benefits of using quantile analysis is that more robust results can be obtained when testing the quantile properties of sources with fewer counts (Hong et al. 2004). Since there are very few detected counts in the sources, we have adopted this method of analysis. In this analysis, we defined the quantile of a source as $\rm Q_{x\%} = (E_{x\%} - E_{\it lo})/(E_{\it up} - E_{\it lo})$, where $\rm E_{x\%}$ is the energy below which the net counts is $x\%$ of the total number of detected source counts, and $\rm E_{\it lo}$ and $\rm E_{\it up}$ are the lower and upper boundries of the full observed energy band, respectively. Using this definition, we calculated the $\rm Q_{25}$, $\rm Q_{50}$, and $\rm Q_{75}$ quantile values of our sources. These values can be seen in the bottom panel of Figure 3.3. The curves in the same panel represent theoretical quantile values of the same models used in the X-ray colour analysis. Although the results of this analysis are more robust than those of the colour analysis, we still cannot definitively quantify the physical properties of the sources. However, almost all of the sources appear to be in the absorbed part of the diagram.

3.3 Optical observations taken with *HST*

A powerful approach to constraining the ages of XRBs is by placing constraints on the ages of associated stellar clusters (Rangelov et al. 2011). Here we describe how we have applied this method to the X-ray source population of NGC 922, by analysing the data of *HST* WFPC2 and WFC3 observations of the galaxy.

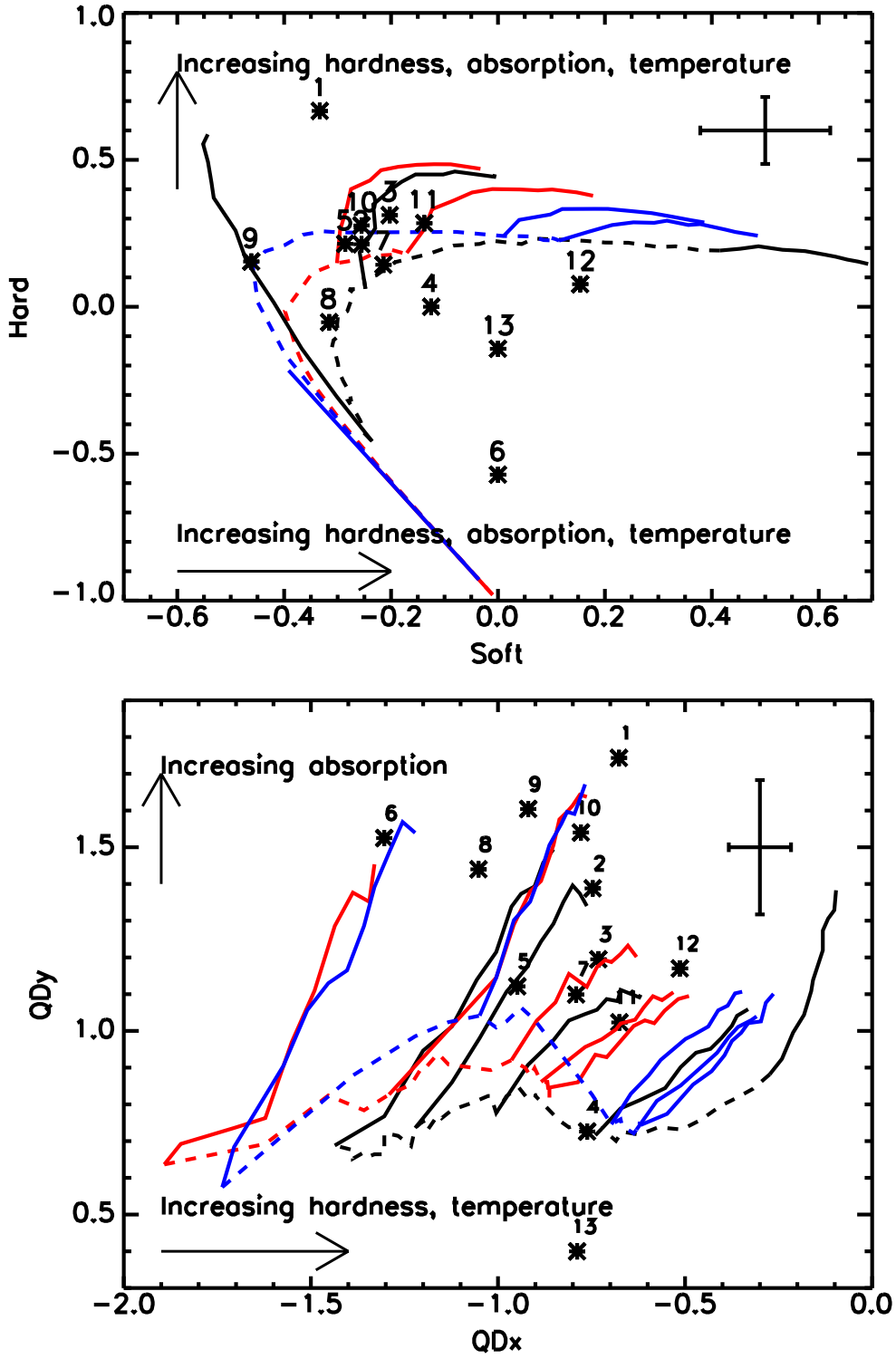

Figure 3.3: *Top:* The colour-colour plot of the 13 X-ray sources. The hard and soft X-ray colours are defined in Section 1.2. The error bars represent typical uncertainty values on the soft and hard X-ray colours of the sources. *Bottom:* The quantile plot of the X-ray sources. QDx is defined as $\log_{10}(m/m\text{-}1)$, where m is the median quantile. QDy is defined as Q_{25}/Q_{75}. In both the top and the bottom panel, the black, blue, and red solid curves represent theoretical tracks of power-law, disc-blackbody, and bremsstrahlung models, respectively. The dashed curves represent unabsorbed model predictions, while the solid curves represent predictions for absorbed models. The arrows indicate increases in model absorption, power-law photon index values, and disc blackbody and bremsstrahlung temperatures. The error bars represent typical uncertainty values on the QDx and QDy values of the sources.

3.3.1 Broad-Band Imaging from the WFPC2 Instrument

NGC 922 was observed with the WFPC2 camera on-board *HST* on June 25 2007, in the F300W ($\approx U$), F439W ($\approx B$), F555W ($\approx V$ band), and F814W ($\approx I$ band) filters, as part of the proposal GO:11112 (PI: Meurer). In order to facilitate the rejection of cosmic rays, two individual exposures were taken in each filter, both of which were subsequently combined. We downloaded the WFPC2 data from the Hubble Legacy Archive (HLA)[1]. The HLA combines the individual flat-fielded exposures for a specific filter together using the PYRAF task MULTIDRIZZLE, and outputs geometrically corrected images. It is worth noting that the WFPC2 has four CCDs − the Planetary Camera (PC) has a scale of 0.0456 arcseconds pix^{-1}, and the three Wide Field (WF) CCDs have a scale of 0.0996 arcseconds pix^{-1}. The HLA provides 2 sets of images for each WFPC2 observation: a combined WFPC2 image including all four CCDs with the PC resampled to the same resolution as the three WF CCDs, and an image of only the PC, at its original pixel scale. We have used the combined WFPC2 image when our clusters were in one of the three WFs and the WFPC2-PC image for objects only located in the PC. Details on pointings and exposure times for the *HST* data used here are given in Table 3.1.

Using the F439W, F547M, and F814W images from the data that we obtained from the HLA, we have created a composite 3-colour image of NGC 922 that can be seen in Figure 3.4. The green circles that overlay the image represent the positions of the X-ray source population of NGC 922, within a 3σ (0.72 arcsecond) uncertainty radius (see below for details on how we have defined the uncertainty of the source positions).

3.3.2 Astrometric matching of the X-ray and optical images

Chandra observations provide good astrometry for X-ray sources, whereas *HST* images give excellent relative source positions, but can have shifts as large as 1.5-2 arcseconds from absolute coordinates. Using the *USNO*-B1.0 catalogue[2] via the DS9

[1] `http://hla.stsci.edu/`

[2] `http://www.usno.navy.mil/USNO/astrometry/optical-IR-prod/usno-b1.0`

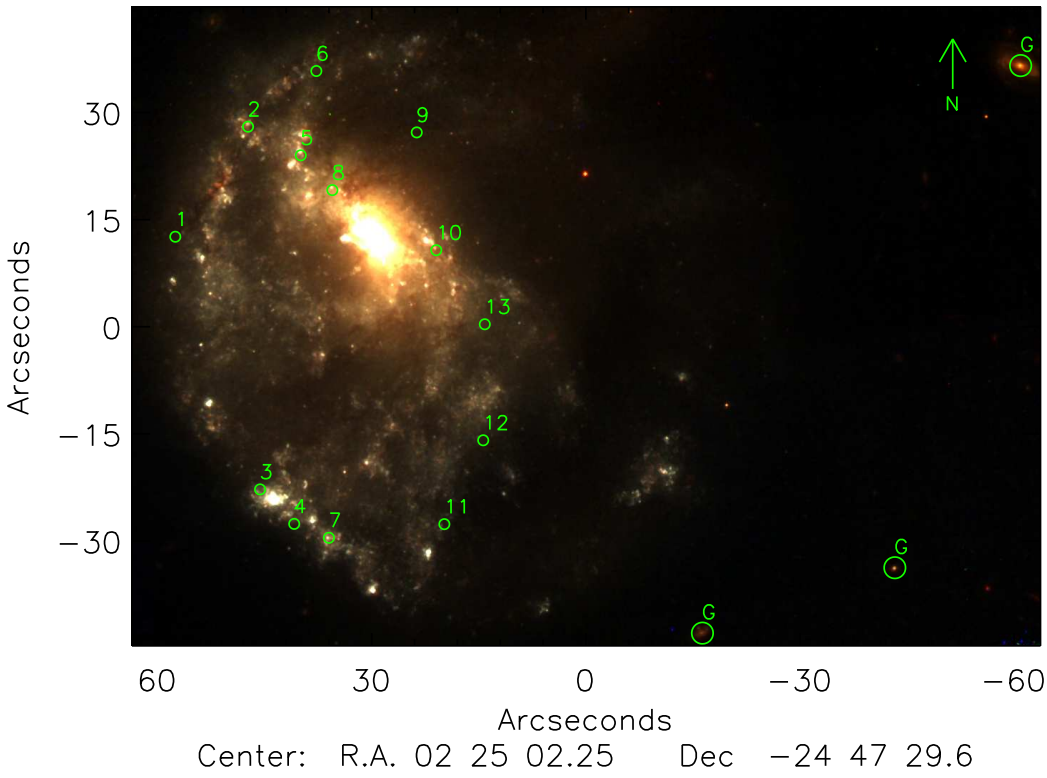

Figure 3.4: A three colour image of NGC 922, created using the data from the *HST* WFPC2 F439W, F547M, and F814W observations. The F439W band image is shown in blue, the F547M image is shown in green, and the F814W image is shown in red. The X-ray source positions are represented by the centre of the green circles. The radii of the circles are set to 3σ uncertainty. The three circles located outside the galaxy marked with a 'G' represent the positions of the background *USNO*-B1.0 catalogue galaxies that were used in calculating the offset between the X-ray and optical images. The green arrow indicates the northern direction of the image.

astronomical data visual application[3], we located three background AGN that were also detected in the *Chandra* and *HST* images. Using these sources, we calculated a mean offset between the optical and X-ray AGN coordinates of 0.16 arcseconds, and used this value to correct for the relative astrometric offset between the X-ray and optical images. We calculated a standard deviation in the offset of coordinates of 0.24 arcseconds, which we have defined as the 1σ astrometric uncertainty value. This value corresponds to a linear distance of ~ 56 pc. Throughout this work, we refer to 1.5σ and 3σ astrometric uncertainty, which corresponds to the emcompassing of 87% and 99.7% of the population of counterpart optical sources within a radius of 0.36 arcseconds and 0.72 arcseconds, respectively.

3.3.3 Optical counterparts to the X-ray sources

Using the IRAF DOAFIND routine[4], we located the optical broad-band point sources that have the closest projected distances to the X-ray source. Figure 3.5 shows F547M images of the regions of NGC 922 in which the X-ray sources are located. The overlaid red circles represent the locations of the putative optical counterparts. These optical counterparts are a combination of stellar clusters and cluster complexes, given the brightness of the sources and the distance to NGC 922. These sources are potentially the host/parent clusters of the X-ray sources. We found that the only sources that have an optical counterpart within 1.5σ uncertainty are Sources 3, 7, and 11. 6 sources (Sources 2, 8, 9, 10, 12, and 13) have the nearest optical sources located within a region between 1.5 and 3σ uncertainty. It is less certain whether or not these optical sources have such an association with the X-ray sources, although it is still a statistical possibility. Sources 5 and 6 have possible optical counterparts located just outside 3σ uncertainty. Sources 1 and 4 appear not to posses any obvious optical counterparts located anywhere close to the 3σ uncertainty region.

Using the IRAF PHOT routine[5], we performed *UBVI* circular aperture photometry

[3] `http://hea-www.harvard.edu/RD/ds9/`
[4] `http://iraf.noao.edu/scripts/irafhelp?daofind`
[5] `http://iraf.noao.edu/scripts/irafhelp?phot`

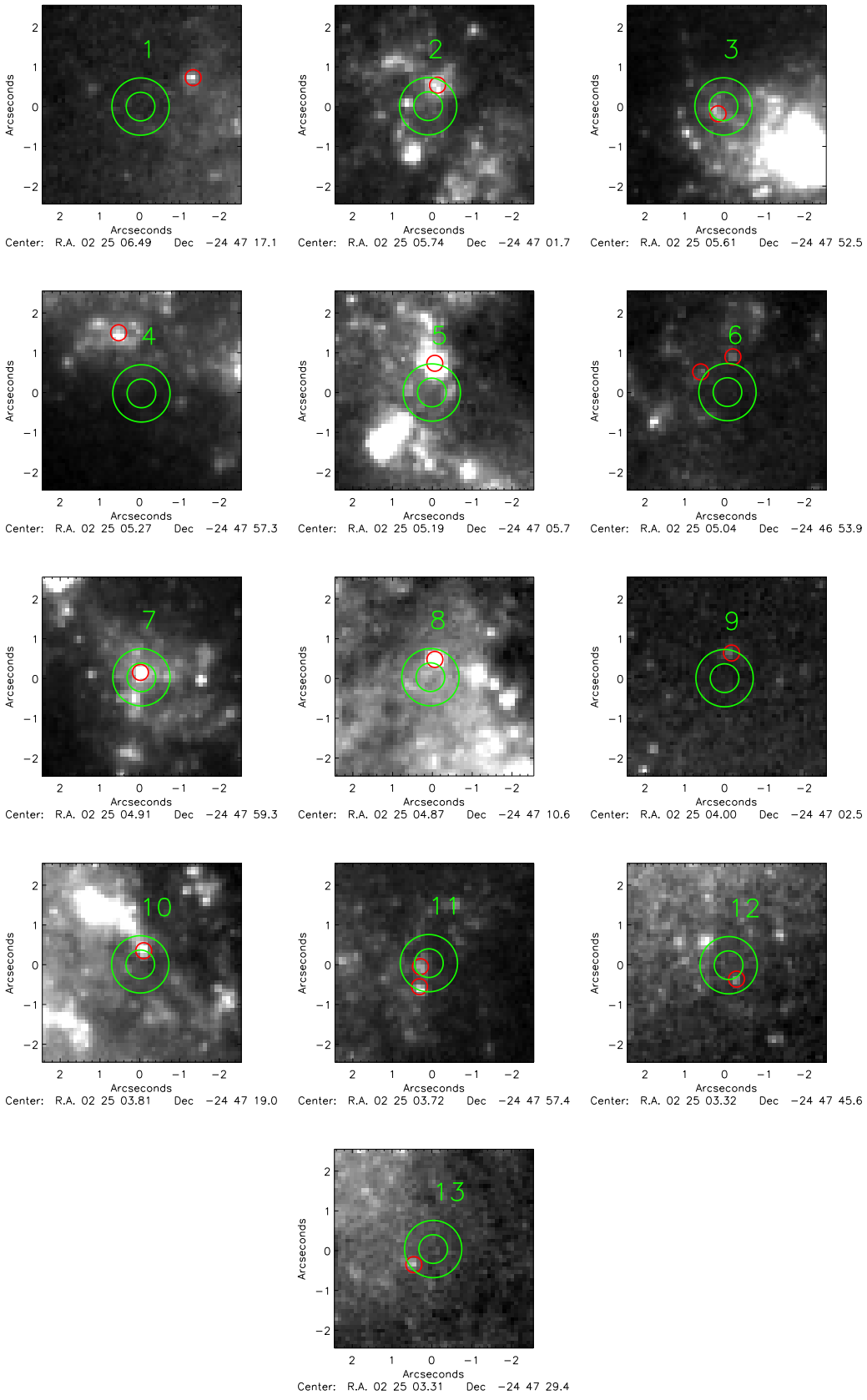

Figure 3.5: F439W-band images of the regions of NGC 922 containing the 13 X-ray binaries associated with stellar sources. These images were created using the *HST* F555W image of the galaxy. The green circles represent the 1.5σ and 3σ positional uncertainties of the X-ray sources. The smaller red circles represent the positions of the associated stellar clusters and stars. The orientation of the images is the same as that in Figure 3.4.

on these sources, assuming an aperture radius of 2 pixels, and a background annular aperture of inner and outer radius 10 and 14 pixels, respectively. Note that any point-like objects that are detected in the background annular region were rejected. We used zeropoints on the VEGAMAG system, taken from Holtzman et al. (1995). When applying these zeropoint magnitudes, we took into account an instrumental analogue to digital gain of ~ 2.11. The source magnitudes were corrected for CTE effects by applying a modified version of the formula given by Dolphin (2000)[6]. In order to extrapolate the total magnitude in each source from that within the 2 pixel apertures, a further magnitude correction was applied, based on concentration index (*CI*, the difference in magnitude between a radius of 2 pixels and 4 pixels). The corrected V-band source magnitudes, as well as the source locations and the distance between them and their associated X-ray source, can be seen in Table 3.3.

3.3.4 Narrow-Band Hα Imaging from the WFC3 Instrument

In addition to the broad-band imaging, NGC 922 was recently imaged in the narrow-band F665N and F621M filters with the ACS/WFC camera on February 8, 2010, as part of Proposal 11836 (PI: Prestwich). The details of this observation can be seen in Table 3.1. The F665N filter covers Hα and [NII] emission, which (in the absence of hard ionising X-ray sources) is typically found in regions of ionised gas near massive young stars. Stellar population synthesis models predict that Hα emission drops precipitously for star clusters older than ≈ 10 Myr, so the presence of line emission provides an excellent means of selecting very young star clusters. Note that the narrow-band emission is not necessarily coincident with the stars in NGC 922, and hence gives an independent line of evidence for the ages of XRBs.

Figure 3.6 shows a continuum-subtracted Hα image of the entire galaxy, created by normalising the F621W continuum image, and subtracting it from the line image. In Figure 3.7, the continuum-subtracted image is divided into sub-regions of the

[6]This modified CTE correction formula can be found at `http://purcell.as.arizona.edu/wfpc2_calib/`

Table 3.3: Properties of the *UBVI*- and Hα-detected sources located closest to the X-ray sources

Source	RA (J2000)	Dec (J2000)	$V_{\rm mag}$	U-B	B-V	V-I	Age (Myrs)	Distance[(a)] (pc)	Velocity[(b)] (km s^{-1})	Distance to Hα[(c)] (pc)	Note
1	02:25:06.39	-24:47:16.4	23.88	-1.32	0.09	0.42	> 10	351	> 34	307	[1,4]
2	02:25:05.73	-24:47:01.2	22.66	-1.15	0.02	0.55	6 – 8 or 20 – 50	134	3 – 7	319	[2,5]
3	02:25:05.62	-24:47:52.7	23.29	-1.22	-0.02	0.27	3 – 6	54	9 – 18	57	[3]
4	02:25:05.31	-24:47:55.8	22.66	-1.57	-0.03	0.08	> 10	379	> 37	313	[1]
5	02:25:05.19	-24:47:05.0	21.87	-1.24	0.09	0.23	3 – 6	172	28 – 56	103	[1,5]
6	02:25:05.02	-24:46:53.0	24.30	-1.12	-0.41	0.45	10 – 50	208	4 – 10	444	[1,4]
	02:25:05.08	-24:46:53.4	24.35	-1.67	0.24	0.34	10 – 50	196	4 – 10	-	[1,4]
7	02:25:04.91	-24:47:59.2	21.98	-1.24	0.06	0.53	6 – 8	29	4 – 5	209	[3]
8	02:25:04.86	-24:47:10.1	21.34	0.08	0.16	0.40	10 – 50	107	2 – 5	466	[2]
9	02:25:03.99	-24:47:01.9	24.45	-0.76	-0.03	0.50	100 – 300	153	0.5 – 1	-	[2,4]
10	02:25:03.80	-24:47:18.7	22.81	-1.36	0.14	0.82	3 – 6	82	16 – 40	29	[3]
11	02:25:03.74	-24:47:57.5	23.78	-1.32	-0.12	0.69	10 – 50	54	2 – 5	105[(d)]	[3,4]
	02:25:03.74	-24:47:58.0	23.66	-1.07	0.35	0.64	10 – 50	148	5 – 14	-	[2]
12	02:25:03.30	-24:47:45.0	25.35	-0.88	-0.42	0.04	100 – 300	94	0.3 – 1	-	[2,4]
13	02:25:03.34	-24:47:29.8	24.69	-0.58	0.85	0.35	100 – 300	145	0.5 – 1	-	[2,4]

Notes: [1] Outside the 3σ X-ray error circle; [2] Between the 1.5σ and 3σ X-ray error circle; [3] Within the 1.5σ X-ray error circle; [4] A faint V-band detection; [5] Possibly multiple source detections in the F621M band; [(a)] Projected distance between the X-ray source and associated star cluster, assuming a linear distance of 1 arcsecond is $\sim$ 233 pc; [(b)] Lower limit range for the projected velocity of the X-ray source; [(c)] Projected distance between the X-ray source and the centre of the closest significant Hα emitting blob; [(d)] Weak Hα emission at this location.

galaxy, all of which contain at least 1 of the X-ray sources. Plotted over these images are the positions of the X-ray sources, centred within the green 3σ uncertainty circles. Table 3.3 shows the distance from each X-ray sources to the centre of the closest significant Hα emitting blob.

It can be seen that $< 1/2$ the sample of X-ray sources (Sources 2, 3, 5, 7, and 10) are apparently located close to recent star formation, with distances ≤ 300 pc from the nearest significant Hα emission region. Of these, only 3 (Sources 3, 5, and 10) are within 1.5σ of a Hα emission region. If the predictions of stellar population synthesis models are correct, it would be expected for the clusters associated with these 5 sources to have ages ≤ 10 Myrs, with those closer to recent star formation having lesser ages than those that are farther away. It would also be expected that the clusters associated with the remaining 6 X-ray sources to have ages of at least 10 Myrs, as they are considerably more distant from recent star formation activity.

3.4 Cluster Properties

Figure 3.8 shows the 2-colour diagrams displaying the U-B, B-V, and V-I colours of the optical cluster counterparts to the X-ray sources, calculated using the magnitudes of these sources. These plots also display the stellar population tracks of Bruzual & Charlot (2003). These tracks represent the colour evolution of synthetic stellar populations from an age of 1 Myr to ~ 15 Gyrs, given a Salpeter initial mass function (Salpeter 1955) and a metallicity value of $Z = Z_{\odot}$ (see Wong et al. 2006).

Each of the colours along the synthetic stellar population tracks has a corresponding age. Therefore, the ages of the clusters were constrained by performing a least χ^2 fit comparing the colours of the sources against those of the tracks (Chandar R., private communication). Throughout this fitting, the source colours were corrected for extinction using values that were calculated using the extinction curve of Fizpatrick (1999). These age constraints can be seen in Table 3.3. We found that in our sample of X-ray sources with visible optical counterparts, only 5 have very low ages, with constraints of < 10 Myrs. Of these sources, Source 3, 5, and 10 have age constraints between 3 and 6 Myrs. The remaining 2 sources (Sources 2 and 7) have

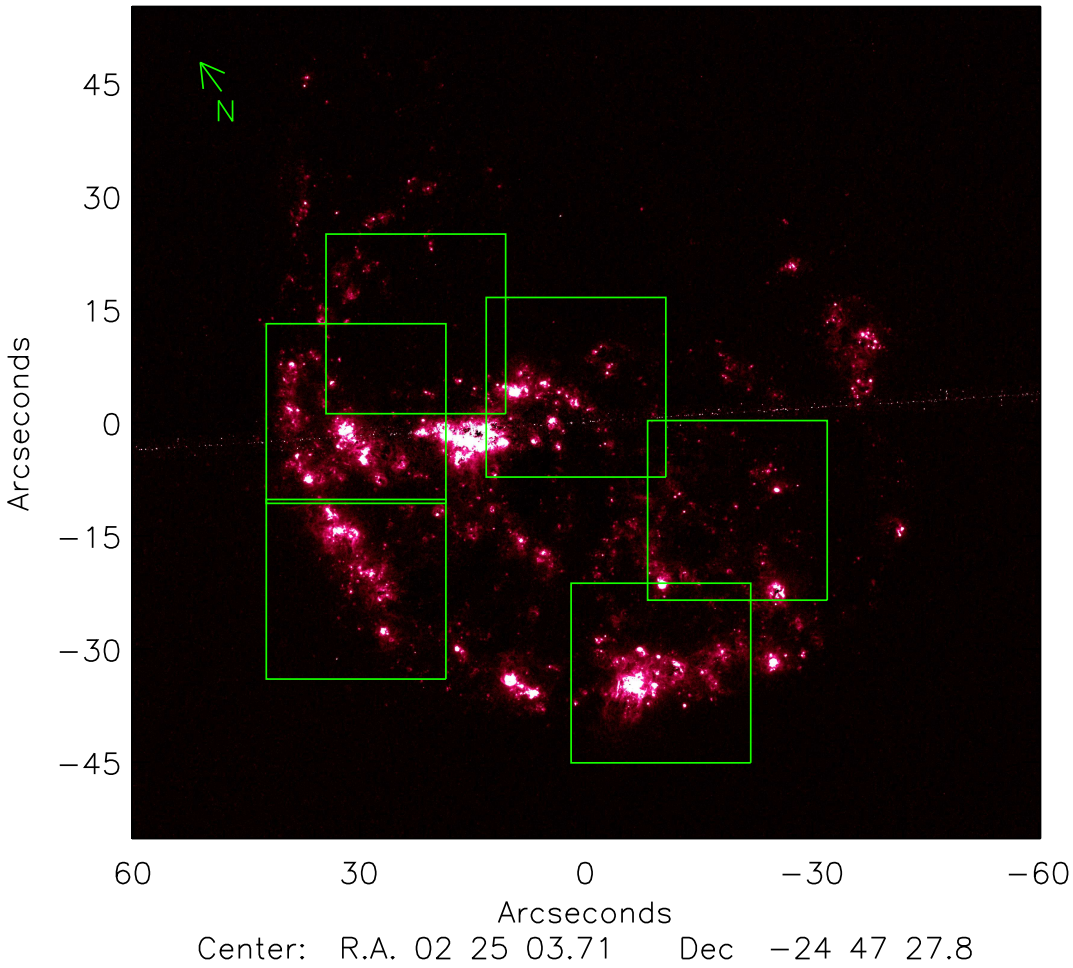

Figure 3.6: A Hα image of NGC 922, created by subtracting a normalised F621M image of the galaxy from the narrow F665 band image. The boxes overlaid represent the segments of the galaxy that are used to create the images in Figure 3.7. The green arrow indicates the northern direction of the image.

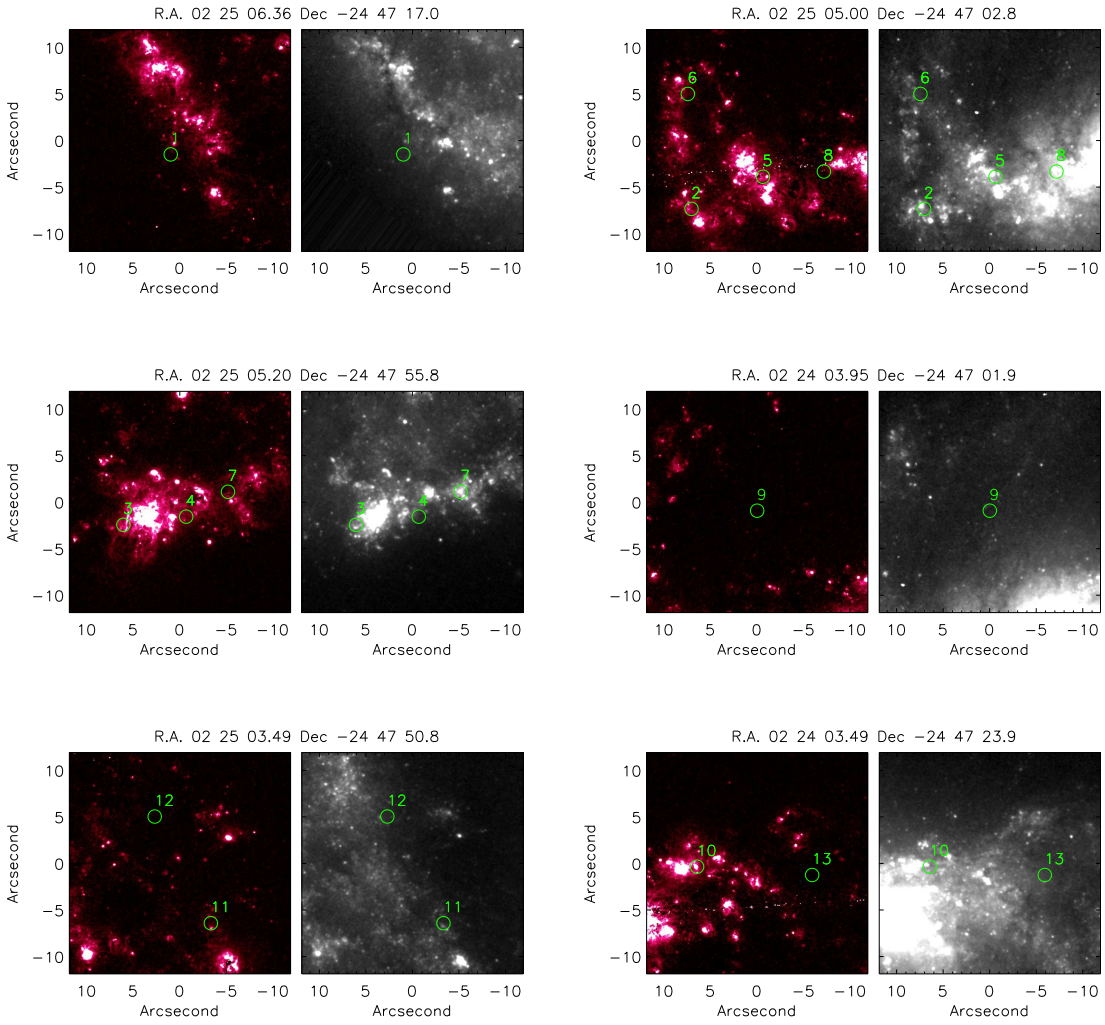

Figure 3.7: The left hand side of each panel is a magnified segment of NGC 922, created using the Hα emission-subtracted image seen in Figure 3.6. Th e left hand side of each panel is an F439W-band image of the same segment of the galaxy. Both Hα and F439W-band images show the locations of the 13 X-ray sources as green 3σ uncertainty regions. The orientation of the images is the same as that in Figure 3.6.

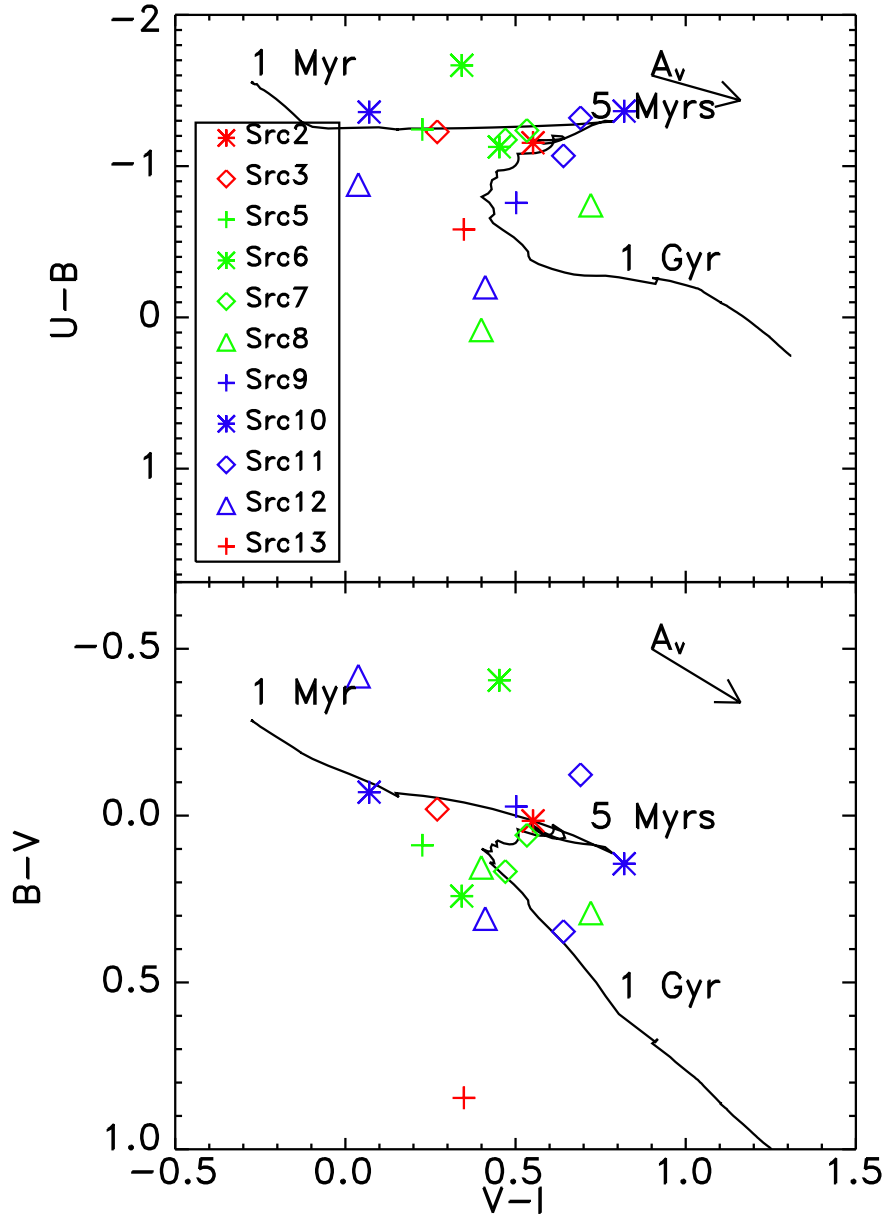

Figure 3.8: Optical 2-colour (V-I vs. U-B, and V-I vs. B-V) plots of the closest clusters associated with the X-ray sources (see the legend on the plot for source-symbol associations). The solid lines represent colour evolution tracks of solar metallicity stellar populations, as per the models of Bruzual & Charlot (2003). The model tracks in each panel evolve with time as they propagate from top-left to bottom-right. The reddening vector in each panel has a size of $A_V = 0.5$.

age constraints ranging from $\sim 6 - 8$ Myrs. Note, however, that a degeneracy was encountered in the colour analysis of Source 2, resulting in a second age constraint of $\sim 20 - 50$ Myrs from the source. Sources 6, 8, and 11 have a moderate age constraint of $\sim 10 - 50$ Myrs. The remaining sources in the sample have significantly older age constraints, ranging from $100 - 300$ Myrs. We could not place a quantitative age constraint on Sources 1 and 4, since they have no apparent optical counterpart. Given the distance between the sources and recent star formation, we have placed a lower age bound of 10 Myrs on them both. However, it is possible that the sources are significantly older than this.

3.5 Discussion

3.5.1 The nature of the XRBs

We have applied two independent methods to constrain the ages of the XRBs in NGC 922. First, we used the properties of stellar clusters closest to the sources. We distinguished between sources that are associated with star clusters or stellar complexes (i.e., within 3σ of an optical counterpart) and those that are not, although we recognise that the former may still not be physically associated due to the large physical distance covered by our 3σ uncertainty, and/or a lack of information about on the relative positions of the 2 objects along our line-of-sight. Second, we used proximity to Hα emission, as this emission traces gas ionised by young massive stars, and is not necessarily co-spatial with optically luminous star clusters.

From our investigation, we have yielded several results regarding the nature of the X-ray sources in NGC 922, in relation to the ages of the sources. A summary of these results can be seen in Table 3.3. Sources 3, 5, and 10, all of which are located within 1.5σ of Hα emission, have counterpart clusters with colours indicating an age constraint of $3 - 6$ Myrs. The sources with age constraints slightly older than this are numbers 2 and 7. The colours of the clusters associated with both sources indicate an age constraint of $6 - 8$ Myrs, although a degeneracy is present in the age constraint of Source 2. It is possible that the cluster associated with this source is considerably older than this, with a constraint of $10 - 50$ Myrs. In the case of Source

7, the age constraint agrees with the much smaller distance between the X-ray source and recent star formation. Sources 6, 8, and 11 have counterpart clusters with a much older age constraint of 10 – 50 Myrs. This agrees with the large distances between the sources and significant Hα emission. Sources 9, 12, and 13 are seen to be associated with what could possibly be some of the oldest and faintest clusters in the galaxy. The colours of these clusters indicate an age constraint of 100 – 300 Myrs, agreeing with the very large distances between the X-ray sources and Hα emission.

The observed displacement between the X-ray sources and optical counterparts indicate that the distribution of offsets between these sources is considerably wider than that which we predicted (see Figure 3.9). When fit with a gaussian curve, the distribution of sources with age constraints < 10 Myrs displayed a standard deviation of $\sigma \sim 91$ pc (~ 0.39 arcseconds), while the sources with higher age constraints displayed a standard deviation of $\sigma \sim 118$ pc (~ 0.51 arcseconds). These larger values of σ suggest that the sources may have been ejected by their host clusters, either by kicks resulting from asymmetric SN explosions, or by a dynamical interaction. Although we cannot distinguish between the two ejection mechanisms, we have placed a lower limit range on the ejection velocity components perpendicular to our line of sight for each of the X-ray sources. These values, which were calculated by assuming that the ejections occurred soon after the formation of the clusters, and dividing the projected distance between the sources and corresponding clusters by the respective upper and lower age constraints, can be seen in Table 3.3.

Sources 3, 5, and 10 (i.e., the 3 youngest sources) display the highest projected velocities, with values ranging from 9 – 56 km s^{-1}. The only other sources display velocities within this range are Sources 1 and 4, with lower limits of 34 km s^{-1} and 37 km s^{-1}, respectively. However, these velocities are based on a lower age limit of 10 Myrs, and could possibly be significantly lower than this. The majority of sources with age constraints of 6 – 8 Myrs and 10 – 50 Myrs are seen to display considerably lower ejection velocities, with values ranging from 2 – 7 km s^{-1}. Only Source 11 has a moderately higher velocity than this, with a range of 5 – 14 km s^{-1}. The lowest velocities in the sample are seen in the oldest sources, with velocities ranging from

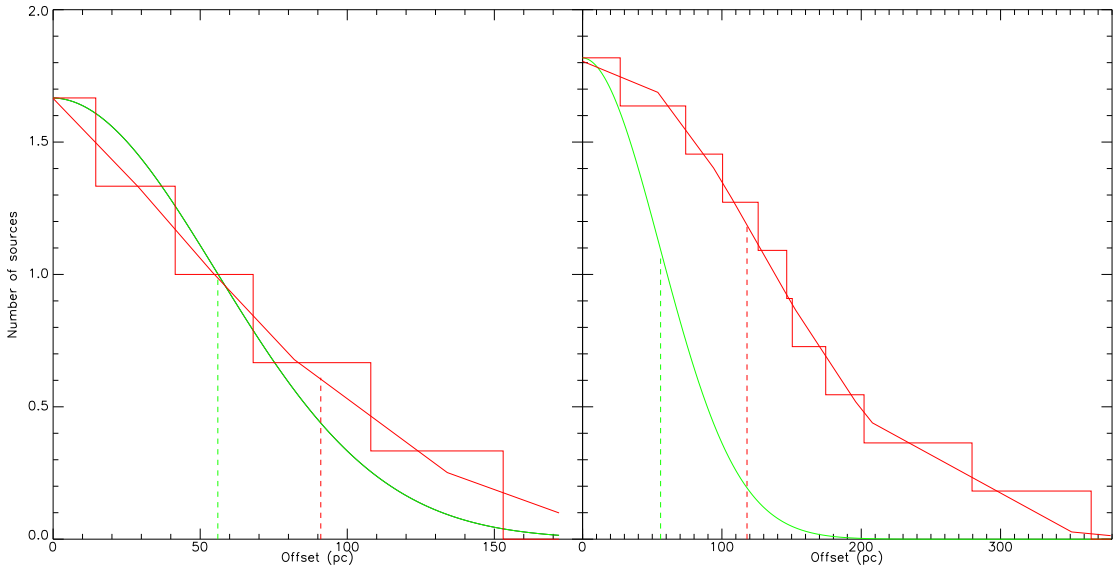

Figure 3.9: The distribution of offsets between the X-ray sources and optical putative cluster counterparts with age constraints < 10 Myrs (*left*) and > 10 Myrs (*right*). The green curve in each panel represents the predicted distribution of sources, with a standard deviation of $\sigma = 0.24$ arcseconds. The red histograms represent the observed distribution of source offsets. The red curves represent the gaussian curves that best fit the distributions. The dashed vertical green and red lines indicate the standard deviations of the predicted and observed distributions, respectively.

$0.3 - 1$ km s^{-1}. Note that if IMBHs are formed as a result of direct collapse of super stars in the cores of SSCs, SNe, and therefore SN kicks, are not expected to occur (Portegies Swart et al. 2004). If this is the case, it can be argued that the youngest sources in our sample are incompatible with hosting IMBHs. Also note that if a binary system is ejected from its parent cluster, it typically experiences an ejection velocity of ~ 10 km s^{-1} (e.g., Kaaret et al. 2004). At this velocity, a source will have attained a distance of ~ 100 pc from its parent cluster after 10 Myrs. This may imply a degeneracy in association between the X-ray sources in our sample (in particular the oldest sources), and the clusters that we have identified as their optical counterparts.

The results from our X-ray analysis indicated that high levels of absorption can be seen in a number of the sources (see Figure 3.3). In particular, Source 1 displays a likely absorption column density that would be sufficient to extinguish any optical counterparts close to the source. Also, a number of sources with counterpart clusters at distances $> 1.5\sigma$ (i.e., Sources 2, 6, 8, 9, 10, and 12) are seen to display high

column densities. It is possible that young clusters exist closer to these sources, but are being extinguished by high levels of dust in our line of sight. Therefore, the results that we have yielded in the analysis of these X-ray sources may be questionable.

3.5.2 The relationship between ULXs and recent star formation

Prestwich et al. (2012) reported that among the X-ray source population in NGC 922, 8 sources display luminosities $> 10^{39}$ erg s^{-1}, and are therefore classified as ULXs (c.f., Table 3.1). Our work has subsequently revealed that out of these 8 ULXs, 3 are located within 3σ of relatively bright Hα emission, thus implying that less than half the ULXs population in NGC 922 are associated with recent star forming activity. All 3 of these sources are located within 3σ of stellar clusters that are at least moderately bright. Four of the remaining 5 sources are associated with recently formed stellar clusters (ages < 10 Myrs), also implying an association with recent star formation. The remaining ULX is associated with a faint cluster with an age greater than that of the other clusters.

Like NGC 922, the Cartwheel galaxy is an example of a star forming collisional ring galaxy. Previous studies have indicated the presence of > 20 ULXs located within the galaxy (Gao et al. 2003; Wolter & Trinchieri 2004). Figure 3.10 shows a 3-colour image of the galaxy, overlaid with the locations of the ULXs. Gao et al. (2003) reported the majority of ULXs to be located close to Hα knots within the galactic system. This association indicates an association between the ULXs and regions of on-going star formation.

Although not a drop-though ring galaxy, the Antennae galaxy system is another example of an active star forming galactic system. In a study of the X-ray source population of the system, Rangelov et al. (2011) discovered that from a sample of 7 ULXs in the Antennae galaxy (c.f., Figure 3.11), only 3 were coincident with or very close to either Hα emission, or a young stellar cluster. They found the remaining 4 ULXs to be located in regions of the galaxy that do not display recent star formation, and therefore deduced that these ULXs are likely to be considerably

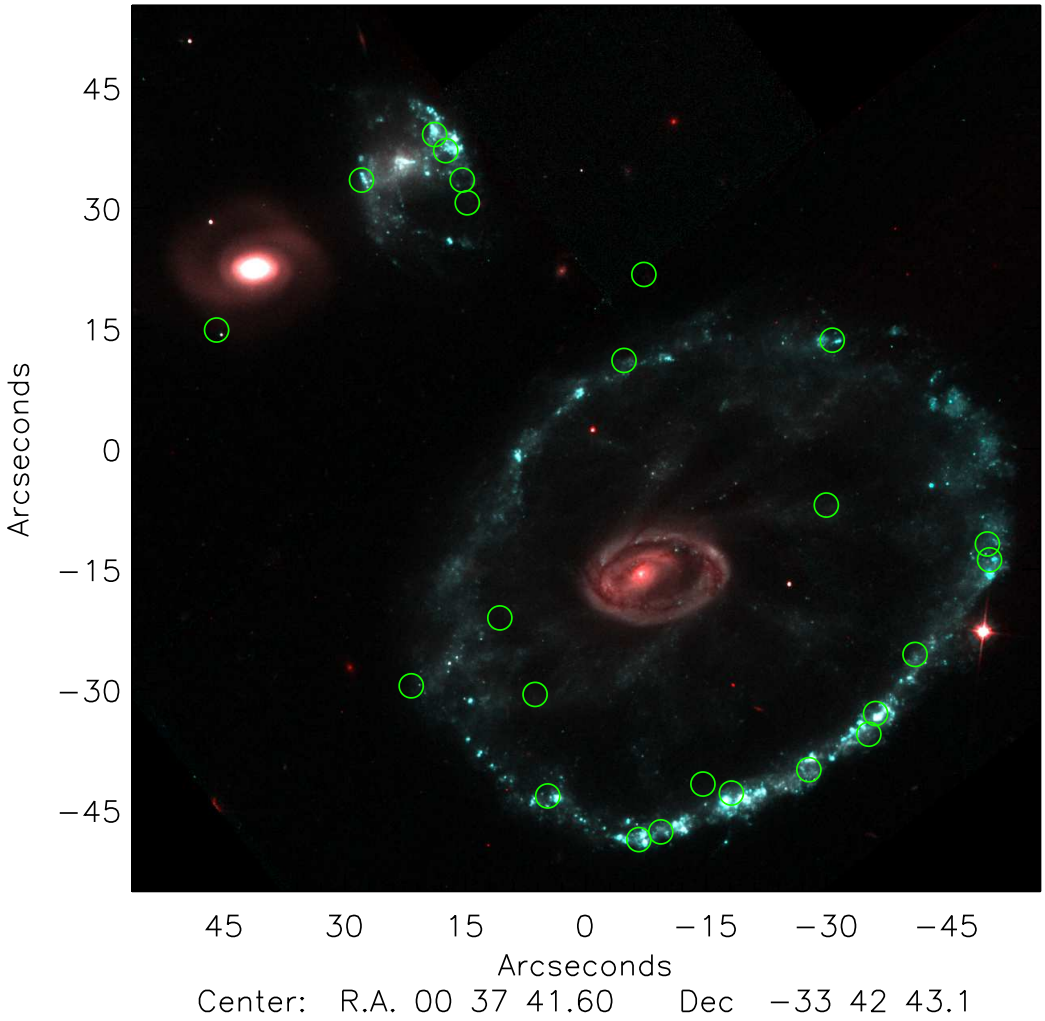

Figure 3.10: A red/blue image of the Cartwheel galaxy system, created using *HST* F814 and F450 observation taken in October 1994 (PI Borne). The locations of the ULXs identified by Wolter & Trinchieri (2004) are represented by the green circles.

older than 10 Myrs.

In a study of 47 ULXs located within 27 *SDSS* star forming galaxies, Swartz et al. (2009) reported 60% of sources to be located within regions of star formation activity. However, the authors also reported that 10/12 of the brightest ($L_{\rm X} > 3 \times 10^{39}$ erg s^{-1}) ULXs in the sample are located within regions that display optical colours considerably less blue, and therefore older, than those seen in typical HII regions in their sample of galaxies. A possible interpretation for this is that the brightest sources are accreting HMXBs with B-type companion stars with ages within a range of 10 – 20 Myrs, thus inferring very little Hα emission in the vicinity of the sources. If this is the case, then it is possible that an even greater majority of ULXs in the sample are located within regions of star formation activity.

In summary, recent results increasingly support a correlation between ULXs and local regions of recent star formation. This result is consistent with the numerical model predictions of Belczynski et al. (2008).

3.6 Summary

In this work, we present age constraints of 13 XRBs located within the drop-through ring galaxy NGC 922. Star formation is ongoing in the galaxy, as a result of a shock-wave propagating through the galactic disc. This shock-wave was caused by a collision between NGC 922 and a neighbouring dwarf galaxy $\sim$ 330 Myrs ago. We find that 5/13 X-ray sources are associated with the ongoing star formation, which is occurring in both the ring close to the edge of the galaxy, and in a region close to the galactic nucleus. These, as well as 6 of the remaining 8 sources, are associated with star clusters. By constraining the ages of these clusters, we find that those associated with the star formation are no more than $\sim$ 10 Myrs old. The sources that are located farther away from recent star formation have age constraints significantly greater than this, with some constraints as high as 100 – 300 Myrs. The importance of these results is reflected in their agreement with those of the latest XRB and stellar population synthesis models. The projected distance between the X-ray sources and associated clusters indicate that the sources may have been ejected from their parent

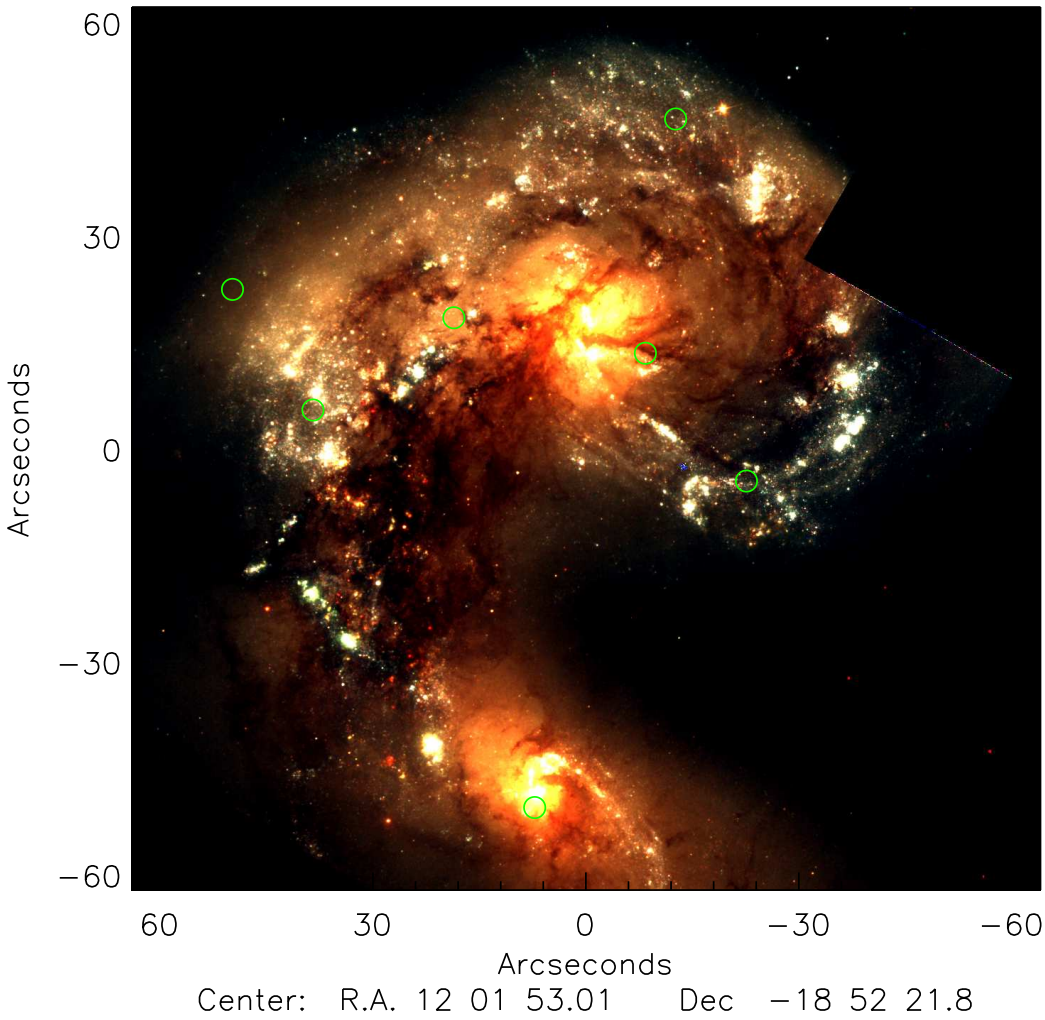

Figure 3.11: A 3-colour image of the Antennae galaxy system, created using *HST*WFPC2 F439, F555, and F814 observations of the galaxy that were taken in January 1996 (PI Whitmore). The locations of the 7 ULXs identified by Rangelov et al. (2011) are represented by the green circles.

clusters mostly by dynamical interactions or ejection by SN explosions. It can be argued that if these sources were ejected by their parent clusters, then the projected velocities of the youngest sources with respect to their associated clusters imply an inconsistency between the sources and IMBHs. The results obtained for a number of XRBs in the sample may be questionable, as they have been seen to display high levels of absorption, indicating that dust may be extinguishing other, potentially closer and younger, associated clusters.

Chapter 4

The brightest X-ray point sources in M82

4.1 Introduction

M82 is an irregular galaxy (Irr II, Sandage 1960; I0 type, de Vaucouleurs & de Vaucouleurs 1964) located in the M81 galaxy group, at a distance of 3.89 Mpc (Sakai & Madore 1999). With a dynamical mass of $\sim 1.5 \times 10^{10}\ M_{\odot}$ and an optical extent of $\sim$ 12 kpc (e.g., Griffiths et al. 2000), this dwarf galaxy is considered the prototypical starburst galaxy (Rieke et al. 1980). It is currently experiencing an extremely powerful starburst episode, with a star-formation and supernovae rate of $\sim 10\ M_{\odot}\ \mathrm{yr}^{-1}$, and $\sim 0.1\ \mathrm{yr}^{-1}$, respectively (e.g., O'Connell & Mangano 1978). This starburst, which can be see in the central $\sim$ 500 pc region of the galaxy, was likely initiated by a tidal interaction between the galaxy and its more massive neighbour M81, $\sim 10^{8}$ years ago. Evidence of this interaction can be seen in a plume of HI emission bridging the two galaxies (Cottrell 1977; Yun et al. 1994).

Evidence of the current star-formation has been identified in several bands, including IR, radio, and optical. Harper & Low (1973) reported the far IR luminosity of the galaxy to be higher than that of any other band, at $\sim 10^{44}\ \mathrm{erg\ s}^{-1}$. This very high IR luminosity is likely an indicator of the rate of formation of OB-type stars (Rieke et al. 1980). Several young supernova remnant candidates have been discovered within the nuclear region of M82 through radio observations (Kronberg

& Biermann 1983; Kronberg et al. 1985; Fenech et al. 2010). In the optical band, giant HII regions have been detected within the central $\sim$ 600 pc of the galaxy (Pedlar et al. 1999). As well as the presence of HII regions, optical observations have indicated that a population of $\sim$ 200 SSCs exist within M82 (Christopher et al. 2004).

M82 is a highly extinguished object, with $A_\nu \sim 5 - 25$ towards the central regions of the galaxy (Lester et al. 1990; Telesco et al. 1991; Waller et al. 1992; McLeod et al. 1993). This being the case, X-rays are a very powerful tool in exploring the properties of the galaxy, and so most X-ray observatories have observed M82. These observations have revealed a combination of hard and soft diffuse emission and hard compact emission in the central regions of the galaxy, and soft diffuse emission extending outwards in a halo (Watson et al. 1984; Kronberg et al. 1985). This halo of soft diffuse emission has been observed to extend $\sim$ 3' south-east and 1.7' – 2.5' north-east (e.g., Bregman et al. 1995). An example of an X-ray image of the galaxy can be seen in the left hand panel of Figure 4.1. This image shows data from an early (1991) *ROSAT* PSPC observation of M82. The spatially extended emission is thought to be emission from a two temperature plasma (e.g., Ranalli et al. 2008; Tsuru et al. 2007; Strickland & Heckman 2007), tracing a freely expanding 'superwind' (e.g., Fabbiano 1988) that originates within the galaxy (Cappi et al. 1999). This wind, which is thought to be propagating at speeds of a few 1000 kms^{-1} (Lynds & Sandage 1963; Burbidge, Burbidge, & Rubin 1964; Seaquist & Odegard 1991), was likely caused by the expansion and subsequent breaking through of a star-formation-powered superbubble from the galactic disc (Heckman, Armus, & Miley 1990). Evidence of the superbubble was reported by Weiss et al. (1999), where it can be seen in CO emission lines. The X-ray emission is thought not to be coming from the wind, but from plasma within the halo that is being shock-heated by the wind (Lehnert et al. 1999).

Some interesting relationships have been found within the galactic halo between X-ray and optical emission. For example, the right hand panel of Figure 4.1 shows a Hα image of M82 with overlaid contours. These contours trace the X-ray emission coming from the galaxy, as seen by the 1991 *ROSAT* observation. Clearly, there

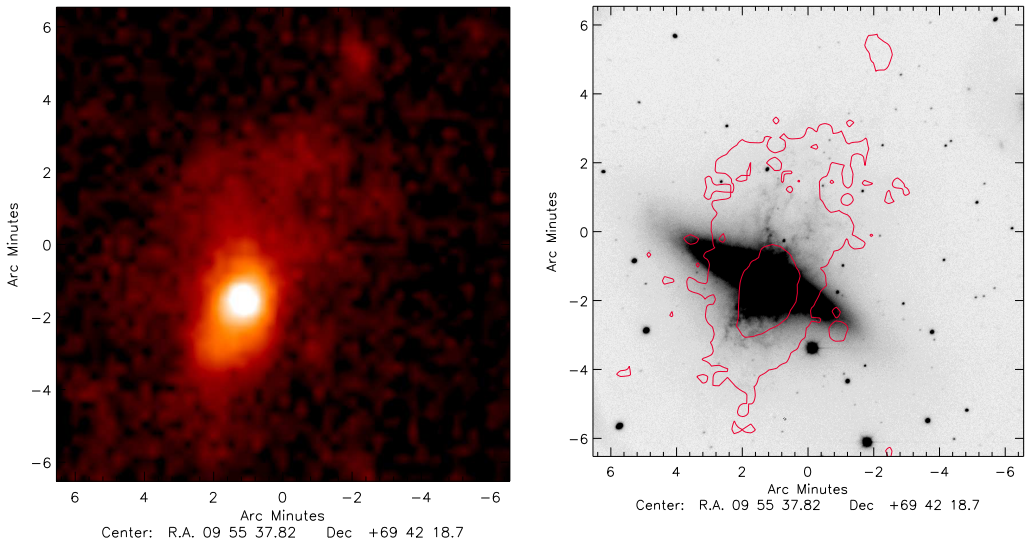

Figure 4.1: *Left:* A 0.1 – 2.4 keV *ROSAT* PSPC image of M82, created using data from an observation in 1991. *Right:* A KNPO Hα image of M82. Overlaid onto this image are contours representing the X-ray emission at photon count levels of 1 and 2 cts pix^{-1}. These contours were created using the *ROSAT* image in the left hand panel.

is a correlation between the Hα filament structure (i.e., the Hα 'cap', Tsuru et al. 1997), and the X-ray emission in the galactic halo.

The compact X-ray source population of M82 has been of great interest since the very first X-ray observations of M82. Point sources both outside and inside the nucleus of the galaxy have been reported. Watson et al. (1984) reported the presence of 8 point-like X-ray emitters, based on the analysis of *Einstein* High Resolution Imager (HRI) data. They deduced that the sources were likely to be Population II objects (i.e., HMXBs, SN remnants, and young OB stars), given the starburst nature of M82. They found the 0.2 – 4 keV luminosities of the sources to be $\sim 10^{38}$ erg s^{-1}, implying that the sources were likely to be HMXBs, if they were singular sources. They also pointed out the possibility that the sources may instead be compact stellar clusters of $\sim 10^{5-6}$ stars, given that OB stars have typical X-ray luminosities of $\sim 10^{33}$ erg s^{-1} (e.g. Vaiana et al. 1978). Fabbiano (1988) reported the possibility of young XRBs dominating the 1.2 – 10 keV *Einstein* Imaging Proportional Counter (IPC) flux within the galactic nucleus, thus agreeing with the results of Watson et al. (1984). Contrary to these results, in a high resolution study of M82, Bregman

et al. (1995) point out that the *ROSAT* HRI instrument does not have sufficient spatial resolving power to determine whether the X-ray emission coming from the central region of the galaxy is powered by XRBs. Thus, they provisionally inferred that the emission is thermal, produced by hot gas from SNe. Soon after, Tsuru et al. (1997) and Ptak & Griffiths (1999) reported that the imaging power of *ASCA* was not good enough to explicitly resolve point sources within the central region of M82, but did report an apparent hard single point source within the galactic nucleus and suggested it to be an obscured low luminosity AGN.

With the launch of the high spatial resolution *Chandra X-ray Observatory*, a breakthrough in resolving X-ray point sources in spatially complex regions occurred. Zezas et al. (2001) reported the presence of 24 X-ray point sources within the galaxy, several of which are located close to the nucleus. 12 of these point sources were found to display levels of variation from the first detected flux ranging from 20 – 700% on timescales of 1 – 6 months, thus indicating the likelihood of them being HMXBs (Zezas et al. 2001). Prestwich et al. (2001) later reported an increase in the point source population to 32, based on an improved data set. The variability of these sources has recently been investigated by Chiang & Kong (2011). They reported a further increase in the number of discrete X-ray point sources in the galaxy of 26, thus increasing the known number of point sources to 58. They found that 26 of their sources displayed flux variability on time scales ranging from days to years, 6 of which they classified as transient candidates. They also found that 3 of the sources displayed spectral variation. They concluded that the X-ray population with luminosities $\gtrsim 10^{37}$ erg s^{-1} is dominated by HMXBs, likely with black hole (BH) compact objects. These results both agree with, and greatly expand upon, those of Zezas et al. (2001).

Within the point source population of M82 are a number of candidate ULXs. Catalogues of ULXs in nearby galaxies report the presence of at least 7 ULXs within the central region of the galaxy (e.g., Swartz et al. 2004; Liu & Mirabel 2005; Berghea et al. 2008). Among them is a source that was first reported by Collura et al. (1994), located within the nuclear region of M82. From fitting the soft (0.1 – 2.4 keV) spectrum of the source with a Raymond-Smith model, they found

that the soft band luminosity of the source reached a peak of $6.3{\times}10^{39}$ erg s^{-1}. Crucially, they also reported a drop in luminosity by $\sim 3{\times}10^{39}$ erg s^{-1} during a 9 ks *ROSAT* observation. This variability, coupled with the observed high X-ray luminosities, made this source the brightest candidate BHB system known at the time. This ULX is now known as M82 X-1, and is the brightest and one of the most well studied ULXs in the local Universe.

Several spectral analyses have been performed on M82 X-1. By fitting the spectra of the central region of M82 from 9 *ASCA* observations with a model consisting of a soft thermal component plus either a hard power-law or bremsstrahlung component, Ptak & Griffiths (1999) deduced that a single, highly variable, X-ray source (M82 X-1) dominates the 2 – 10 keV flux in M82. They observed a maximum to minimum observed 2 – 10 keV luminosity difference of 5.9 $\times 10^{40}$ erg s^{-1}. This extremely high long term variability confirmed the compact nature of the source. From their analysis, the authors inferred a mass of $M > 460 M_{\odot}$ for the BH within the system, assuming sub-Eddington, isotropic accretion. Ptak & Griffiths (1999) were not the only authors to report an IMBH mass estimate for the compact object within M82 X-1. With both high long term variability and a peak observed 0.2 – 10 keV luminosity of $L_{\rm X} \sim 10^{41}$ erg s^{-1}, Kaaret et al. (2001) inferred a mass of ~ 500 $M_{\odot}$ for a central compact object within the system. Similarly, Matsumoto et al. (2001) inferred a mass ≥ 700 $M_{\odot}$ on a compact object from the observed X-ray luminosity ($\geq 10^{40}$ erg s^{-1}), and high levels of long term variability. Yuan et al. (2007) argued that the spectrum of M82 X-1, with a hard photon index of $\Gamma = 1.67$ and luminosity of $2.4{\times}10^{40}$ erg s^{-1}, can be reproduced by advection-dominated accretion. They found that the X-ray luminosity in the solution to their model was within the range of $L_{\rm X} \sim 4$ – 10% $L_{\rm EDD}$, thus inferring a BH mass of $\sim 10^4 M_{\odot}$. These values, although considerably greater than those estimated from previous spectral modelling, are still within the IMBH range. Contrary to the IMBH mass estimates, Okajima et al. (2006) found that if the spectrum of M82 X-1 was fit with the slim disc model of Kawaguchi (2003), a mass of ~ 19 – 32 $M_{\odot}$ could be inferred. Their motivation for selecting this model was that when fit with both a simple absorbed power-law and disc blackbody model, the *Chandra* spectrum of

M82 X-1 yielded statistically unacceptable fits. But when fit with a p-free disc model (Mineshige et al. 1994; Hirano et al. 1995; Kubota & Makishima 2004; Kubota et al. 2005), the fit was acceptable, with a p-value ~ 0.6. Unlike the p-value of ~ 0.75 for a typical accretion disc, this value indicated that the source was experiencing advection-dominated accretion, and thus the accretion disc was slim. From their analysis of a *Suzaku* XIS spectrum of M82 X-1, Miyawaki et al. (2009) deduced that the source was highly Comptonised, and emitting close to the Eddington limit, thus resembling ultraluminous state emission (Gladstone et al. 2009), and hence inferring a black hole mass of ~ 100 – $200\ M_{\odot}$.

As well as variability in observed flux, M82 X-1 displays variation in spectral shape. For example, a harder M82 X-1 *Chandra* spectrum was seen by Swartz et al. (2004) and Kaaret et al. (2009), where they found the best fitting model to be a power-law with a photon index ranging from $\Gamma \sim 1.3$ – 1.7. Fiorito & Titarchuck (2004) found that *RXTE* and *XMM-Newton* spectra of M82 X-1 were much softer than this, with photon index values ≥ 2. The authors further suggest that the source was undergoing a transition from the hard to the TD state during the *RXTE* observation, and that during the *XMM-Newton* observation, the source was in the TD state. A possible transition from the hard to the TD state was also reported by Feng & Kaaret (2010).

Evidence for M82 X-1 being a compact X-ray accretor is not just present in the spectral properties and long term variability of the source. High levels of short term variability have also been detected in M82 X-1. Strohmayer & Mushotzky (2003) reported a 54 mHz QPO in a 30 ks *XMM-Newton* observation of M82. Despite the low spatial resolution of *XMM-Newton*, they deduced that the QPO was coming from M82 X-1, given that the observed flux levels matched the highest level seen in any *Chandra* observation of the source to date. Using surface brightness fitting with the known *Chandra* positions of the sources in the nucleus of M82, Feng & Kaaret (2007) confirmed that the QPO does indeed originate within M82 X-1. The presence of the QPO in the power spectrum of X-1 was confirmed by Fiorito & Titarchuck (2004), when they reanalysed the *XMM-Newton* data first looked at by Strohmayer & Mushotzky (2003). They also discovered a second QPO at ~ 110

mHz in *RXTE* observational data, which they interpreted as a harmonic to the $\sim$ 50 mHz QPO. Investigating the possibility that a scaling relation exists between low frequency QPOs in ULXs and energy spectral photon indices, they examined the same relationship that exists in Galactic BHBs (e.g., Vignarca et al. 2003). Comparing the low QPO frequency of $\sim$ 5 Hz for XTE J1550-564 and $\sim$ 50 mHz for M82 X-1, the authors inferred an intermediate BH mass of $\sim 10^3 M_{\odot}$ for M82 X-1, assuming a photon index of $\Gamma = 2.7$ for both sources, and a mass of $10 M_{\odot}$ for XTE J1550-564. They noted that this estimate agrees with mass estimates of other ULXs obtained using absolute normalisations and colour temperature (Shrader & Titarchuk 2003). Mucciarelli et al. (2006) reported a QPO at 113 mHz in a power spectrum from a 105 ks *XMM-Newton* observation of M82 X-1. Their analysis showed that the properties of the QPO are similar to those of the $\sim$ 50 mHz QPO reported in previous works. They argued that the properties of the QPO in the source are strongly suggestive of a type-C low frequency QPO (Remillard et al. 2002). Assuming that BH mass is inversely proportional to QPO frequency, the authors inferred a BH mass range of $\sim 10 - 1000 M_{\odot}$ for M82 X-1. In analysing the same 105 ks of *XMM-Newton* data, Dewangan et al. (2006) reported the presence of the same QPO in the power spectrum of M82 X-1. Similar to the work of Fiorito and Titarchick (2004), Dewangan et al. (2006) estimated the BH mass of M82 X-1 by employing the Γ–ν_{QPO} relation. Comparing the spectral and timing properties of M82 X-1 found in their work to those of GRS 1915+105 (Vignarca et al. 2003), they deduced a BH mass of $M = 25 - 520 M_{\odot}$, assuming a BH mass of 14 ± 4 for GRS 1915+105 (Greiner et al. 2001).

In 2006, a modulation of 62$\pm$2.5 days was discovered in a 240 day *RXTE* PCA observation of M82 (Kaaret et al. 2006a). Kaaret et al. (2006b) interpreted this modulation as a periodic binary orbit of M82 X-1, arguing that the source was the brightest source during the observation and hence the most likely source to display the modulation. Their argument for the periodic orbital nature of the modulation was that if the modulation was a super-periodic orbit, M82 X-1 would most likely have to be a neutron star binary system. The luminosity of the source at the time, and in general, argues against this possibility. However, they note that there is

a low possibility of the modulation not being an orbital period, but instead being aperiodic in nature. Kaaret & Feng (2007) confirmed the 62 day periodicity when they analysed 400 days of new *RXTE* observational data of M82.

One of the first ultraluminous point-like X-ray emitters detected in M82 was reported by Watson et al. (1984), located ~ 1' west of the galactic nucleus, displaying a 0.2 – 4 keV luminosity of $\sim 8 \times 10^{38}$ erg s^{-1}. This source was referred to as Source 1 by Watson et al. (1984), and hence will be referred to as the same in the following text. Watson et al. (1984) argued that the source is a low mass Population II XRB, given an X-ray to optical flux of < 200 (e.g., Patterson 1981). Stocke et al. (1991) report Source 1 as having an observed hard band luminosity (2 – 11 keV) $\geq 2 \times 10^{39}$ erg s^{-1}, thus making it more luminous than any XRB found at that time, in either the Galaxy or the Magellanic Clouds. Given such a high luminosity, the same authors argued for Source 1 being an accreting BHB candidate, thus agreeing with the hypothesis made by Watson et al. (1984) that the source is an accreting binary system. High levels of variability within the source were reported by Collura et al. (1994). They saw that the flux of the Source 1 changed by a factor of ~ 10 over the period of a ~ 13 ks *Einstein* observation in May 1979. The source was subsequently undetected during two *ROSAT* observations of M82, in May and June of 1991 and 1992, respectively. More recently, Source 1 has not been reported as detected by *XMM-Newton* or *Chandra* (e.g., Chiang & Kong 2011; Berghea et al. 2008; Swart et al. 2004), indicating that the source has been in a quiescent state over the last $\sim$ 10 years. The variability of the source points towards the nature of the source being a compact accretor, agreeing with both the arguments of Watson et al. (1984) and Stocke et al. (1991).

Another bright ULX that has been studied in detail is X42.3+59. This source is located within the nuclear region of M82, very close to M82 X-1, and has been reported as the second brightest source in the galaxy (e.g., Feng et al. 2010). Feng and Kaaret (2007) identified X42.3+59 as a ULX transient, showing that the 2 - 10 keV flux of the source varied by a factor of $\sim$ 1000 over a period of $\sim$ 7 years. From a peak hard band luminosity of $2.2{\times}10^{40}$ erg s^{-1} seen in an early *XMM-Newton* observation, the authors inferred a BH mass of $\geq 200 M_{\odot}$ for the

source. Chiang & Kong (2011) confirmed the transient nature of the source, showing that over a period of 8 years, X42.3+59 has displayed a maximum significance in flux difference of $S_{\rm flux} \sim 99$, and a maximum flux ratio of $R \sim 66 \pm 26$. From analysing the source spectra, Kong et al. (2007) suggested that the accretion process may be dominated by advection, thus inferring a BH mass of $\sim 10^3$ – $10^4 M_{\odot}$. However, they do not rule out the possibility that the source is experiencing a unique spectral/luminosity state. A low frequency type A-I QPO was reported to originate from this source by Feng et al. (2010). By a mass scaling relation with Galactic XRBs that also display type A-I QPOs (e.g., XTE J1550-564), they estimate a BH mass of 1.2 - $4.3{\times}10^4 M_{\odot}$ for X42.3+59.

Recent work by Jin, Feng, & Kaaret (2010) identified another ULX in M82. This source, which they labelled as X37.8+54, is located west of the galactic nucleus, and has been seen to display high levels of long-term variability (Jin, Feng, & Kaaret 2010; Chiang & Kong 2011), with X-ray luminosities ranging from ~ 1 – 6.5×10^{39} erg s^{-1}. The source has also been seen to display high levels of short-term variability (Jin, Feng, & Kaaret 2010; Chiang & Kong 2011). From analysing the spectra of the source from 10 *Chandra* observations, Jin, Feng, & Kaaret (2010) identified the compact object within X37.8+54 as a fast rotating black hole of mass < 100 $M_{\odot}$. The authors also suggested that the spectra indicate 2 distinct canonical BH accretion states: the hard state and the TD state. This is supported by the results of Chiang & Kong (2011), who reported that the hardness ratios of the source, as per *Chandra* observations, vary to such a degree as to imply spectral state transition.

In this work, we exploit the *Chandra* data obtained by *Great NASA Observatories M82 Extended Survey* (*GNOMES*) to investigate the X-ray properties of the 8 brightest X-ray point sources in M82, including M82 X-1, X42.3+59, and X37.8+54. The aim of *GNOMES* is to study the properties of both the diffuse and point-like X-ray emission within the galaxy, at the highest spatial resolution over as wide a field as possible. This being the case, the *Chandra* observations were taken over 4 separate pointings: north-east, north-west, south-west, and south-east of the nucleus. The four pointings were taken over 6 observations, all adding up to an exposure of $\sim$ 480 ks, thus making for a data set rich enough to allow us to

Table 4.1: Basic information on the *GNOMES Chandra* observations of M82

Obs. ID	Date[a]	Pointing[b]	Aimpoint		Exposure
			RA	Dec	(ks)
10542	24-06-2009	NE	09:56:00.20	+69:42:11.8	118.61
10543	04-07-2009	NW	09:55:47.54	+69:41:52.8	118.45
10925	07-07-2009	SW	09:56:04.88	+69:38:33.0	44.54
10544	07-07-2009	SW	09:56:04.89	+69:38:32.9	73.53
11800	20-02-2010	SE	09:56:19.30	+69:39:23.1	16.82
10545	28-07-2010	SE	09:56:19.50	+69:39:33.8	95.04

[a] Date in dd-mm-yyyy; [b] The observational pointing direction, where NE = North-East, NW = North-West, SW = South-West, and SE = South-East.

investigate the spectra of the sources in some detail, as well as short and long term temporal characteristics and spectral variability.

4.2 Observations and source selection

The six observations examined in this work (obs ID 10542, 10543, 10925, 10544, 11800, and 10545) were taken as part of the *Great NASA Observatory M82 Extended Survey* (*GNOMES*). The X-ray portion of this survey was designed to observe M82 with four 120 ks *Chandra* Advanced CCD Imaging Spectrometer (ACIS) – S3 chip observations, each time with a different pointing direction (north-east, north-west, south-west, and south-east of the nucleus of M82). Two of the four observations (the south-east and south-west observations) were subsequently divided into two separate observations. All six observations were taken in VFAINT mode. Details of these observations can be seen in Table 4.2. The data were downloaded from the *Chandra* Data Archive[1]. We reprocessed the level 1 files in the usual fashion using the *Chandra* CIAO v. 4.1 software[2], and used the resulting data in our analysis.

The aim of this work was to investigate the X-ray properties of the brightest X-ray point sources in the galaxy. In order to do this, we firstly needed to locate these sources within the *Chandra* observations. We did this by running the

[1] `http://cxc.harvard.edu/cda/`
[2] `http://cxc.harvard.edu/ciao/`

CIAO WAVDETECT[3] routine on the full-band (0.3 – 10 keV) images, with scale values of 1, 2, and 4 pixels. This yielded the detection of several sources, most of which looked to be quite dim. We filtered the resulting source sample by rejecting any source with a peak observed luminosity $< 5 \times 10^{38}$ erg s^{-1}, assuming a distance of 3.89 Mpc, and a best fitting spectral power-law model with $\Gamma = 2$ and hydrogen column density of $N_{\rm H} = 10^{21}$ cm^{-2}, across the 6 observations. In order to do this, we first estimated the background-subtracted count rates of the sources using the CIAO APRATES routine. Using the *Chandra* Proposal Planning Toolkit PIMMS routine[4], we then estimated the fluxes based on the count rate values. After filtering out the less luminous sources, we were left with the 8 brightest X-ray sources, including the previously studied M82 X-1, X42.3+59, and X37.8+54. Figure 4.2 show the locations of these highly luminous point sources within M82. For the sake of convenience, we will label the 8 sources as Src1 (= X37.8+54), Src2 (= M82 X-1), Src3, Src4 (= X42.3+59), Src5, Src6, Src7, and Src8, with Src1 and Src8 having the lowest and highest RA positions, respectively (i.e., right to left in Figure 4.2). For context, an *SDSS* 3-colour optical image of the central region of M82 is shown in the lower panel of Figure 4.2. Table 4.2 shows the names and locations of the 8 sources and Table 4.3 shows a summary of the estimated count rates and luminosities, based on aperture photometry. The errors quoted in this table were calculated as 1σ confidence values. It is worth noting that during the first 5 observations, Src4 is extremely dim, with a maximum estimated luminosity of $\sim 6 \times 10^{37}$ erg s^{-1}. The source only displays sufficient luminosity to be considered as part of our sample during the final observation. This is clearly illustrated in Figure 4.3, where each of the panels is a 0.3 – 10 keV image of the central ~ 500 pc of M82 as observed during the 6 observations. Note that the luminosities quoted in the table are only a preliminary estimate, due to the effects of pile-up not being taken into account. We expect that the pile-up levels in Src2 are very high ($> 40\%$), given the high apparent photon count rates of the source. Src5 is also expected to experience high levels of pile-up ($> 20\%$) throughout the observations of 2009. The source is seen to be considerably

[3] `http://cxc.harvard.edu/ciao/ahelp/wavdetect.html`
[4] `http://cxc.harvard.edu/toolkit/pimms`

Table 4.2: The names and locations of the brightest X-ray sources in M82

	Source name[(1)] (CXOM82...)	Other name
Src1	095546.6+694041	X37.8+54
Src2	095550.1+694046	M82 X-1
Src3	095550.4+694036	-
Src4	095551.0+694045	X42.3+59
Src5	095551.3+694044	-
Src6	095551.5+694036	-
Src7	095554.2+694040	-
Src8	095601.3+694111	-

Notes: [(1)] Source names and locations, as noted by Chiang & Kong (2011).

less bright during the final 2 observations, with count rates consistent with pile-up levels $\sim 5\%$. This reduction in brightness of Src5 can be seen in Figure 4.3. The remaining 6 sources have much lower count rates, consistent with very little pile-up ($\leq 5\%$). The apparent luminosities of these sources are considerably lower than those of the two central sources, in some cases reaching > 2 orders of magnitude fainter than Src2.

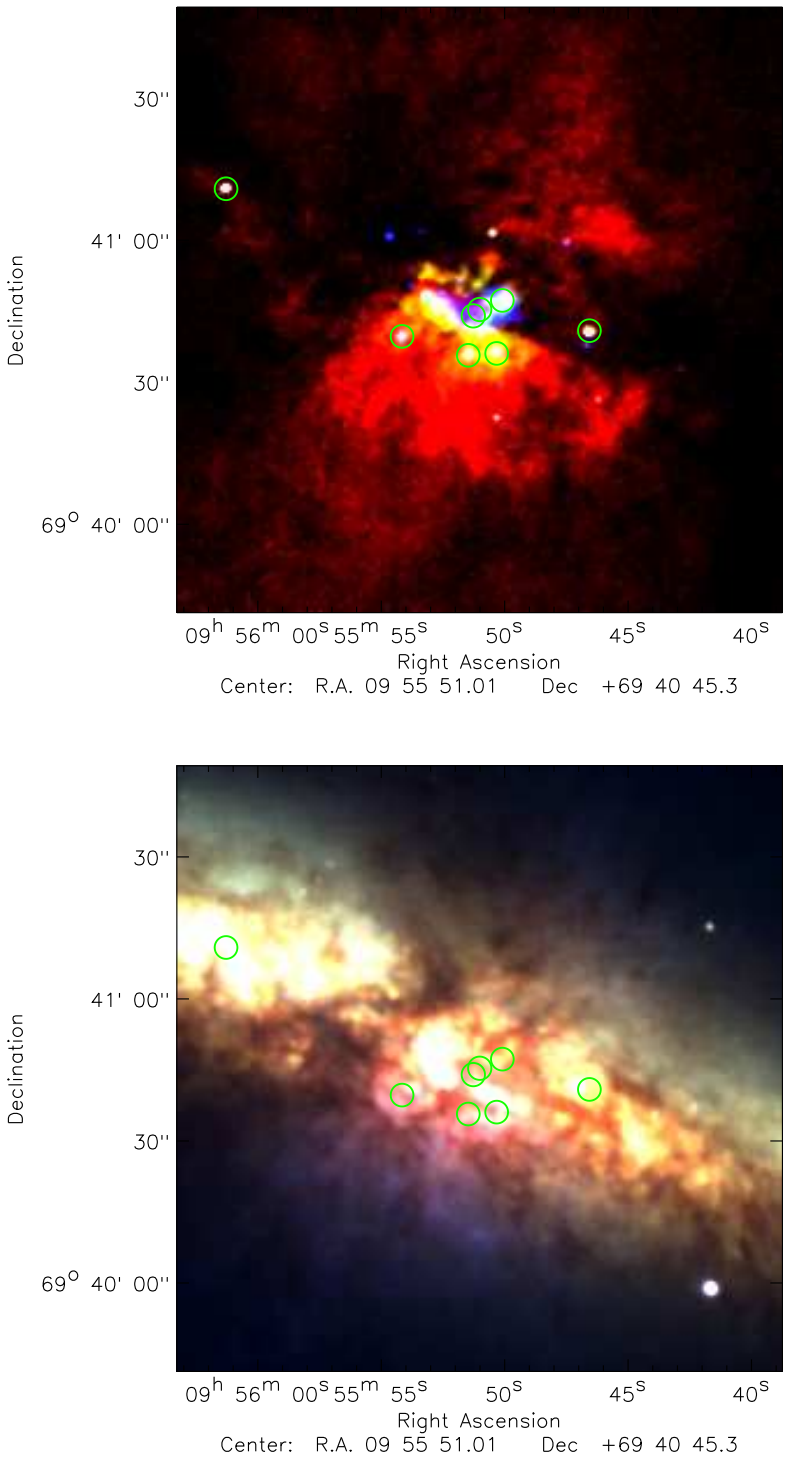

Figure 4.2: *Top:* A composite *Chandra* false-colour image of the central region of M82, created using a stacked image of all six *GNOMES* observations. The bands represented by red, green, and blue in the image are 0.3 – 1 keV, 1 – 2 keV, and 2 – 10 keV, respectively. The 8 bright X-ray point sources are indicated by the green circles. *Bottom:* A composite optical image of the central region of M82, created using r, g, and b band *SDSS* images. The source locations are also indicated by the 8 green circles in this image.

Table 4.3: Preliminary data for the brightest X-ray sources in M82

	10542	**10543**	**10925**	**10544**	**11800**	**10545**
Src1						
Counts$^{(1)}$	3831±106	4943±120	1588±68	2725±90	942±53	4680±118
$L_X{}^{(2)}$	6.60±0.18	8.44±0.2	7.13±0.31	7.51±0.25	10.81±0.61	9.87±0.25
Src2						
Counts$^{(1)}$	26264±278	17855±233	12792±192	18124±232	4322±113	27138±282
$L_X{}^{(2)}$	45.21±0.47	30.54±0.40	57.45±0.86	49.91±0.64	49.61±1.30	57.21±0.59
Src3						
Counts$^{(1)}$	3209±119	3542±123	1403±77	2269±98	471±45	2824±108
$L_X{}^{(2)}$	5.52±0.20	6.05±0.21	6.30±0.35	6.25±0.27	5.41±0.52	5.95±0.23
Src4						
Counts$^{(1)}$	135±45	68±42	121±27	≤42	≤25	3351±81
$L_X{}^{(2)}$	0.24±0.08	0.12±0.07	0.56±0.13	≤0.12	≤0.31	7.29±0.67
Src5						
Counts$^{(1)}$	12556±207	9937±188	6278±145	5985±147	751±54	4208±73
$L_X{}^{(2)}$	21.62±0.36	16.97±0.32	28.19±0.65	16.32±0.40	8.62±0.62	9.15±0.02
Src6						
Counts$^{(1)}$	4343±130	3854±126	1238±73	2329±98	539±45	2546±102
$L_X{}^{(2)}$	7.48±0.25	6.58±0.22	5.56±0.33	6.42±0.27	6.19±0.52	5.37±0.22
Src7						
Counts$^{(1)}$	4437±123	4408±121	1650±75	2649±96	160±27	649±27
$L_X{}^{(2)}$	7.64±0.21	7.52±0.21	7.41±0.34	7.30±0.29	1.84±0.31	1.37±0.06
Src8						
Counts$^{(1)}$	4654±114	3317±97	1082±56	1615±69	11±7	48±16
$L_X{}^{(2)}$	8.01±0.20	5.66±0.17	4.86±0.25	4.45±0.19	0.13±0.08	0.10±0.03

Notes: $^{(1)}$ Source photon counts, calculated using the CIAO APRATES routine; $^{(2)}$ Source observed 0.3 – 10 keV luminosity in units of 10^{38} erg s^{-1}, estimated using the *Chandra* Proposal Planning Toolkit PIMMS routine, with a power-law photon index of 2 and an absorption column density of 10^{21} cm^{-2}. Note that pile-up was not taken into account when computing these values.

4.3 Data analysis

One of the key methods of diagnosing the properties of X-ray sources is by investigating their X-ray spectra. In order to perform spectral analyses on our 8 sources, spectral data and corresponding response files were extracted from the event files of the observations, using the CIAO DMEXTRACT[5], MKARF[6], and MKRMF[7] routines. Circular source and background apertures of radius 2 and 4 arcseconds were used in this extraction in the case of Src1, Src3, Src5 (for observation 11800), Src6, Src7, and Src8, with background apertures located in source-free regions close to their respective sources. With photon counts ≤ 170 during the first 5 observations, Src4 is only bright enough to warrant spectral analysis during observation 10545. Because of the proximity of the source to Src5 (see the bottom right panel of Figure 4.3), an aperture of radius 1.2 arcseconds was used in this extraction. The corresponding background aperture was a circle of radius 2.4 arcseconds, located in a source-free region close to Src4. During the observations 11800 and 10545, Src7 became extremely faint, with photon counts of $\sim$10 and $\sim$50, respectively, thus we did not extract spectra for this source during these observations. Because of the extreme brightness of Src2 during all 6 observations, and of Src5 during the first 4 observations, pile-up for these 2 sources was an issue. Initially, we attempted to account for the effects of pile-up in the spectra of Src2 and Src5 by folding the model fits to the spectra of the sources through the PILEUP model (Davis 2001) in XSPEC. However, the resulting observed flux levels appeared not to match those expected from the effects of pile-up, given the best fitting PILEUP model parameters. We therefore inferred that the levels of pile-up in the sources throughout the observations were too high for this method of analysis to be reliable. Hence we extracted the spectral and response files for these two sources using annular apertures of inner and outer radius 1.5 and 2.5 arcseconds for Src2, and 1.1 and 2 arcseconds for Src5. This ensured the exclusion of the central 3×3 pixel cells (and slightly more in the case of Src2) from the extraction, thus relieving the spectra of the bulk of pile-up

[5] http://cxc.harvard.edu/ciao/ahelp/dmextract.html
[6] http://cxc.harvard.edu/ciao/ahelp/mkarf.html
[7] http://cxc.harvard.edu/ciao/ahelp/mkrmf.html

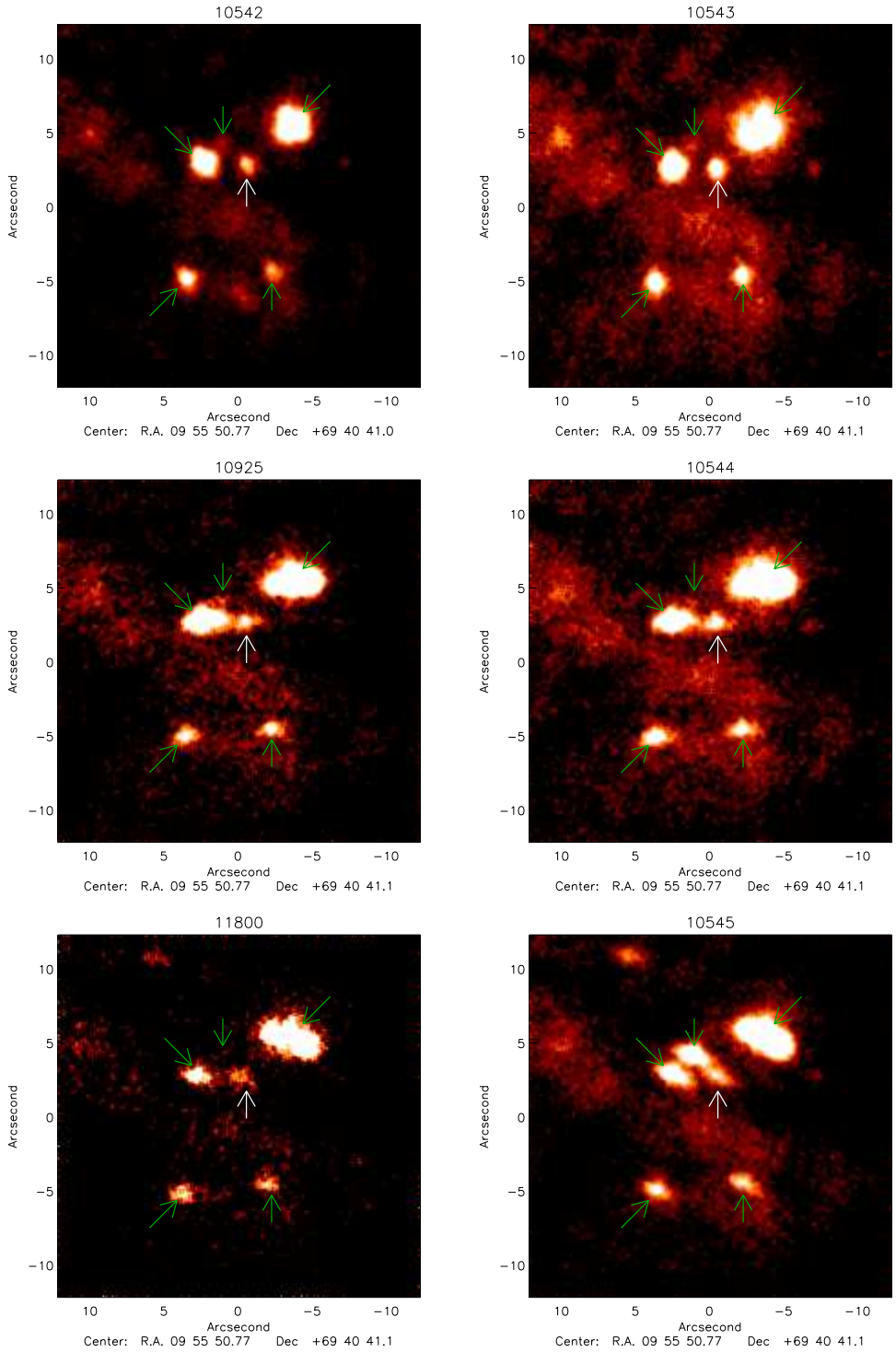

Figure 4.3: From top left to bottom right, 0.3 – 10 keV images of the central $\sim$ 500 pc of M82, created using the data from observations 10542, 10543, 10925, 10544, 11800, and 10545. The green arrows indicate the positions of Src2, Src3, Src4, Src5, and Src6. The white arrow indicates the position of another bright point source in the central region of M82. However, this source displays a luminosity of $L_{\rm X} \leq 4 \times 10^{38}$ erg s^{-1} throughout all 6 observations, and is therefore discounted from our sample. In order to compare the relative brightness of the sources throughout the observations, each of the images has been scaled so that the maximum number of cts pix^{-1} is the same as that of the 10545 image.

effects. The corresponding background apertures were circular regions of radius 5 arcseconds and 2.1 arcseconds for Src2 and Src5, respectively. Since the observed flux of Src5 during the last 2 observations is below the threshold for serious pile-up effects, we used circular sources apertures in the extraction of the spectral data for these observations. As noted above, spectral data and relevant responses of Src5 were extracted from similar source and background apertures to those used in the extraction of data for Src1, Src3, Src6, Src7, and Src8 for observation 11800. Because of the brightness of Src4 during the final observation, and the proximity of Src4 to Src5 (see Figure 4.3), a circular source aperture of radius 1.1 arcseconds was used in the extraction of spectral and response data for Src5. A circle of radius 2.2 arcseconds was used as corresponding background aperture. Spectral model fitting was subsequently performed using XSPEC version 12.5 software (Arnaud 1996). All spectral data with sufficient numbers of counts were binned to at least 20 counts per bin to accommodate for χ^2 statistics within XSPEC. The observation 11800 was considerably shorter than the others, thus yielding a shortage of photon counts in some of the sources. In particular, Src5 and Src7 were the worst effected, whose spectra were left with < 200 counts each. We therefore used the method of Cash statistics (Cash 1979) in fitting the models to these spectra.

Measuring the short-term variability in X-ray point sources is another way of determining their physical properties. To this end, we extracted 0.3 – 10 keV background-subtracted lightcurves using the CIAO DMEXTRACT routine. Apertures similar to those used for the spectral extraction were used in this process. As with source energy spectra, pile-up has an effect on source rms fractional variation (Tomsick et al. 2004). Extracting the lightcurves from the same annular apertures ensured that the regions of the sources most affected by pile-up were again excluded from the extraction. The variability of these lightcurves was measured by both χ^2 testing them against a constant count rate, and by measuring their root mean squared (rms) fractional variation as per Vaughan et al. (2003). Bin sizes were selected on the basis of lightcurves having a signal to noise ratio ≥ 5, with a minimum bin size of 1 ks. Lightcurves with < 16 bins were disregarded. The lightcurve bin sizes, which can be seen Table 4.9, range from $\sim 1000 - 1700$ seconds.

4.4 Spectral results

The most common phenomenological models used to describe the spectra of Galactic BHBs are the simple power-law and the multi-coloured disc blackbody models (PO and DISKBB in XSPEC, respectively). Since this is the case, we used both of these models in the spectral fitting of our 8 sources, together with two absorption components (TBABS*TBABS in XSPEC; see Wilms, Allen, & McCray 2000)[8]. The two separate absorption columns were to account for both Galactic absorption along our line of sight, and absorption intrinsic to the source. The Galactic absorption was set to 4×10^{20} cm^{-2} for the line-of-sight to M82 as per Dickey & Lockman (1990).

Initially, we found that Src5 and Src7 both displayed a soft excess in all of their spectra. An example of this can be seen in Figure 4.4, where the spectra of both Src5 and Src7 from the observation 10542 can be seen. This excess is likely due to emission from hot diffuse gas, not removed by the background subtraction, lying underneath where the sources are located. Figure 4.5 shows 0.3 – 1.5 keV and 1.5 – 10 keV images of Src5 and Src7 from observation 10542. These images support the argument that both sources are located in regions displaying high levels of soft diffuse emission.

To account for this, we separately extracted spectra from an aperture close to each of the sources that was not contaminated by point source emission, but that contained diffuse emission. We subsequently fit these spectra with an absorbed MEKAL model, and retrieved the best fitting parameters of $kT = 1.93$ keV, $N_{\rm H} = 7.8 \times 10^{21}$ cm^{-2}, and abundance $= 0.08\ Z_{\odot}$ for Src5, and $kT = 0.6$ keV, $N_{\rm H} = 8.5 \times 10^{21}$ cm^{-2}, and abundance $= 0.57\ Z_{\odot}$ for Src7. We then simultaneously fit the 6 spectra of the sources with either a TBABS*(TBABS*MEKAL+TBABS*PO) model or a TBABS*(TBABS*MEKAL+TBABS*DISKBB) model, setting the MEKAL parameter values to those previously obtained, and fixing the MEKAL normalisation values to be the same for each of the 6 data sets. In doing this, we obtained the best

[8] In most cases, BHBs can be fit with a combination of these 2 models. However, such spectral fits to this data do not provide statistically significant improvements over single model fits. Hence, we report only the single model fit results in this work.

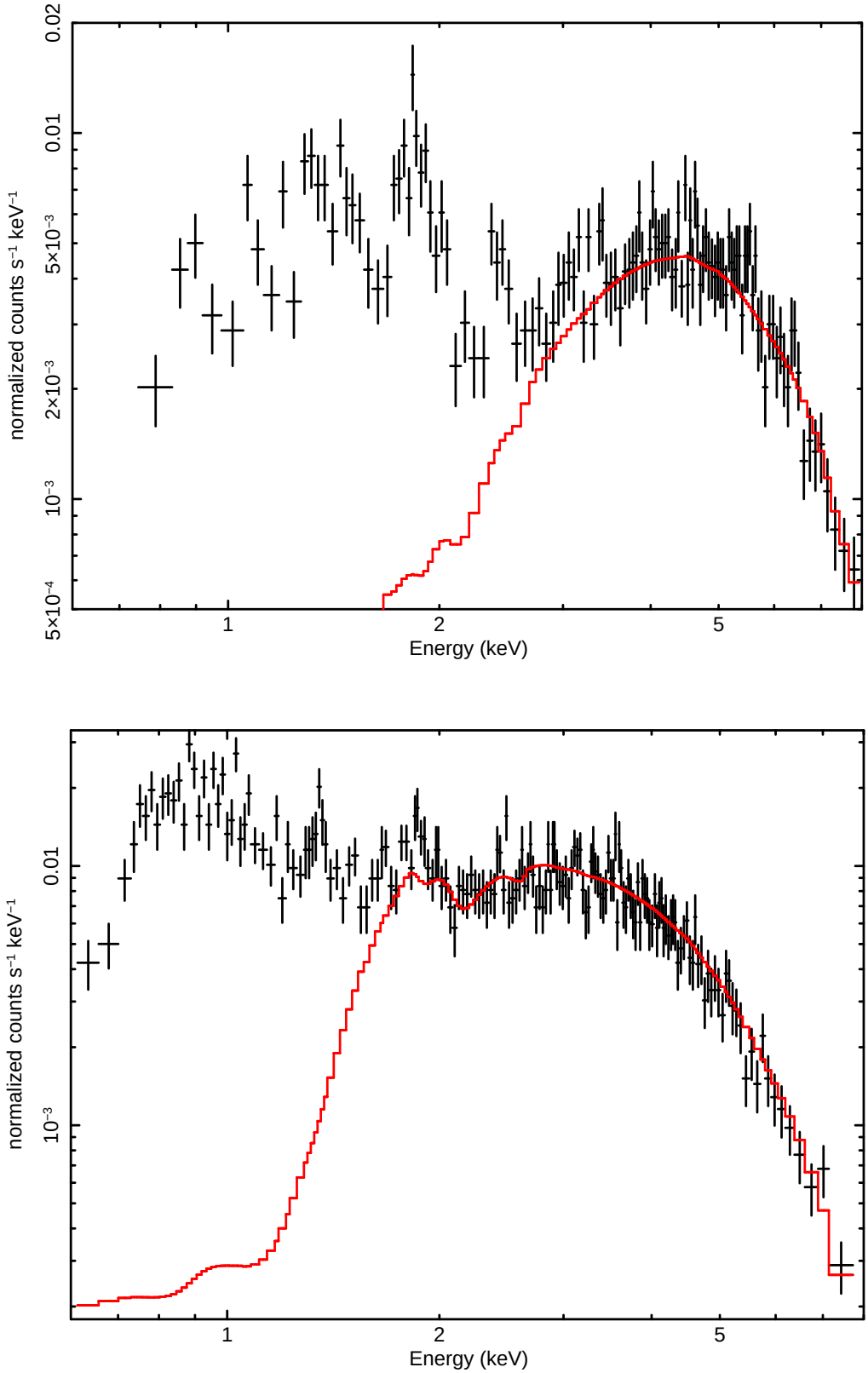

Figure 4.4: The spectra of Src5 (*top*) and Src7 (*bottom*) from observation 10542, overlaid with the best fitting power-law models. Note that the spectrum of Src5 was extracted from an annulus, and therefore has fewer photon counts than might be expected given its high flux.

fitting absorbed PO and DISKBB model parameter values for both sources while making sure that the soft excess in the spectra was modelled consistently throughout the 6 observations.

4.4.1 The sources unaffected by pile-up

The best fitting spectral results for a subset of 5 objects with limited spectral pile-up effects and multiple detections can be seen in Tables 4.4 and 4.5. In the tables, the best fitting χ^2/DoF models are marked in bold, and the χ^2/DoF values that are statistically rejectable (i.e., models with a null hypothesis probability < 0.05) are highlighted by square parentheses. All errors except for those of flux are quoted within a 90% uncertainty range; the flux values are instead quoted within a 68% uncertainty range. To summarise, the best fitting power-law model parameters range from $\Gamma \sim 1.3$ – 3.1 (excluding the 10545 observation of Src7, where $\Gamma \sim 7$) and $N_{\rm H}$ ~ 0.5 – 14×10^{22} cm^{-2} with the best-fitting power-law model, and $kT_{\rm in} \sim 0.8$ – 2 keV and $N_{\rm H} \sim 0.1$ – 10×10^{22} cm^{-2} with the disc blackbody model.

4.4.1.1 Spectral variation of the sources with multiple detections

Thanks to the *GNOMES* observational campaign of M82, we have data from 6 observations of the galaxy with a total exposure time adding up to ~ 0.5 Ms. These observations have provided us with ample data to perform decent spectral analysis on a set of 5 objects, each detected in the majority of the observations. Taking into account the number of spectral fits performed on each individual source, as well as the quality of the spectral data, we have undertaken a study of the variation in the shapes of the spectra.

Initially, we looked at the models which provided the lowest χ^2/DoF fits to each spectrum. Most of the best fitting models are not statistically rejectable, with a null hypothesis probability ≥ 0.05. We compared the best fitting models by creating the histogram shown in Figure 4.6, which displays the number of spectra that are best fit with each model vs. observed luminosity. A distinctive bi-modality can be seen in the histogram, where the sources with higher luminosities are generally best fit

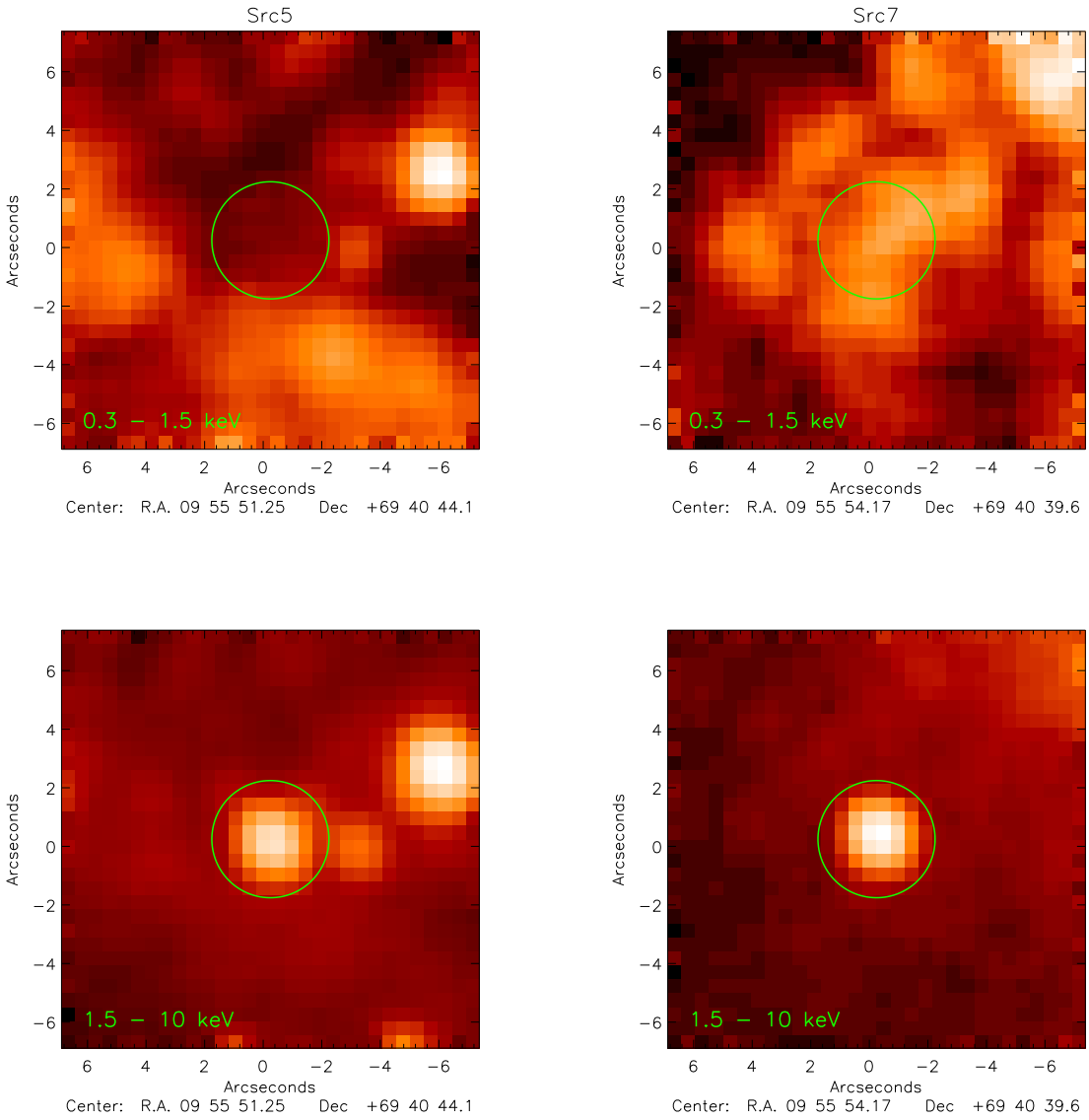

Figure 4.5: 0.3 – 1.5 keV (*top*) and 1.5 – 10 keV (*bottom*) images of the regions of M82 where Src5 and Src7 are located. These images were created using data from the *Chandra* 10542 observation of M82. The green circles indicate the locations of the sources. The images have been scaled logarithmically with arbitrary maximum and minimum ct pix^{-1} values.

Table 4.4: Best fitting XSPEC TBABS*TBABS*PO model parameters

	10542	10543	10925	10544	11800	10545
Src1						
$N_{\rm H}{}^{(1)}$	$0.86^{+0.07}_{-0.06}$	0.89±0.06	$0.70^{+0.07}_{-0.06}$	0.92±0.09	$0.64^{+0.16}_{-0.15}$	$0.69^{+0.06}_{-0.05}$
Γ	2.81±0.10	$2.65^{+0.09}_{-0.08}$	$2.40^{+0.17}_{-0.16}$	2.61±0.13	$2.05^{+0.22}_{-0.20}$	$2.15^{+0.09}_{-0.08}$
$L_{\rm X}{}^{(2)}$	$3.81^{+0.27}_{-0.24}$	$5.48^{+0.31}_{-0.29}$	$5.12^{+0.57}_{-0.50}$	$5.28^{+0.46}_{-0.42}$	$8.74^{+1.38}_{-1.18}$	$7.55^{+0.44}_{-0.41}$
χ^2/DoF	143.54/127	153.88/145	**61.64/59**	**95.28/95**	**36.95/37**	**139.45/148**
Src3						
$N_{\rm H}{}^{(1)}$	$1.37^{+0.25}_{-0.20}$	$1.60^{+0.34}_{-0.23}$	$1.25^{+0.40}_{-0.29}$	$1.92^{+0.47}_{-0.34}$	$1.84^{+0.94}_{-0.69}$	$1.66^{+0.49}_{-0.23}$
Γ	$2.42^{+0.15}_{-0.13}$	$2.33^{+0.18}_{-0.14}$	$2.10^{+0.23}_{-0.20}$	$2.49^{+0.24}_{-0.27}$	$2.26^{+0.61}_{-0.50}$	$2.48^{+0.24}_{-0.17}$
$L_{\rm X}{}^{(2)}$	$4.33^{+0.59}_{-0.47}$	$5.37^{+0.98}_{-0.65}$	$5.96^{+1.22}_{-0.95}$	$5.22^{+1.23}_{-1.29}$	$6.28^{+3.59}_{-2.06}$	$4.92^{+1.31}_{-0.68}$
χ^2/DoF	[260.56/144]	[254.05/157]	95.70/70	[216.06/109]	35.56/25	[287.18/132]
Src6						
$N_{\rm H}{}^{(1)}$	$0.73^{+0.09}_{-0.08}$	$0.59^{+0.08}_{-0.07}$	$0.41^{+0.18}_{-0.13}$	$0.56^{+0.09}_{-0.08}$	<0.42	$0.56^{+0.10}_{-0.08}$
Γ	$1.95^{+0.05}_{-0.09}$	$1.85^{+0.10}_{-0.09}$	$1.58^{+0.20}_{-0.16}$	1.90±0.12	$1.52^{+0.22}_{-0.28}$	$1.80^{+0.12}_{-0.11}$
$L_{\rm X}{}^{(2)}$	$6.57^{+0.47}_{-0.43}$	$5.42^{+0.39}_{-0.36}$	$5.52^{+0.91}_{-0.66}$	$5.35^{+0.48}_{-0.43}$	$6.37^{+1.53}_{-1.19}$	$5.44^{+0.48}_{-0.44}$
χ^2/DoF	200.95/160	**177.30/152**	**68.05/63**	**116.76/109**	22.70/25	**121.61/115**
Src7						
$N_{\rm H}{}^{(1)}$	$7.49^{+0.82}_{-0.76}$	$7.69^{+0.83}_{-0.70}$	$6.77^{+1.39}_{-1.20}$	$7.68^{+1.07}_{-0.93}$	$0.44^{+0.17}_{-0.15}$	$14.27^{+17.20}_{-9.79}$
Γ	2.76±0.22	$2.81^{+0.23}_{-0.22}$	$2.50^{+0.37}_{-0.34}$	$2.93^{+0.30}_{-0.27}$	$2.83^{+0.45}_{-0.41}$	$6.66^{+2.34}_{-4.50}$
$L_{\rm X}{}^{(2)}$	$9.63^{+2.27}_{-1.85}$	$8.74^{+2.08}_{-1.65}$	$9.61^{+4.08}_{-2.74}$	$8.54^{+2.75}_{-1.96}$	$1.65^{+0.41}_{-0.31}$	<12.99
χ^2/DoF	**172.77/179**	**203.29/173**	63.88/78	**117.49/117**	-	**[70.24/43]**
$C-stat/DoF$	-	-	-	-	278.32/660	-
Src8						
$N_{\rm H}{}^{(1)}$	$0.92^{+0.08}_{-0.07}$	$0.85^{+0.76}_{-0.71}$	$1.16^{+0.20}_{-0.17}$	$0.73^{+0.11}_{-0.10}$	-	-
Γ	$2.33^{+0.09}_{-0.08}$	$2.44^{+0.11}_{-0.10}$	$2.83^{+0.22}_{-0.20}$	$2.29^{+0.16}_{-0.15}$	-	-
$L_{\rm X}{}^{(2)}$	$6.01^{+0.41}_{-0.34}$	$3.98^{+0.29}_{-0.27}$	$3.02^{+0.49}_{-0.41}$	$3.24^{+0.35}_{-0.31}$	-	-
χ^2/DoF	[247.19/152]	136.41/117	63.45/42	56.75/61	-	-

Notes: (1) Absorption column density intrinsic to the source (10^{22} cm^{-2}); (2) Observed 0.3 – 10 keV luminosity (10^{38} erg s^{-1}). Luminosity errors were calculated within a 68% uncertainty range. All other errors were calculated within a 90% uncertainty.

Table 4.5: Best fitting XSPEC TBABS*TBABS*DISKBB model parameters

	10542	10543	10925	10544	11800	10545
Src1						
$N_{\rm H}{}^{(1)}$	0.37 ± 0.04	$0.43^{+0.04}_{-0.03}$	0.28 ± 0.07	0.44 ± 0.06	$0.24^{+0.11}_{-0.10}$	$0.34^{+0.04}_{-0.03}$
$kT_{\rm in}{}^{(2)}$	0.87 ± 0.04	0.93 ± 0.04	$1.04^{+0.10}_{-0.09}$	0.94 ± 0.06	$1.32^{+0.22}_{-0.18}$	$1.18^{+0.07}_{-0.06}$
$L_{\rm X}{}^{(3)}$	$3.52^{+0.47}_{-0.41}$	$4.88^{+0.56}_{-0.50}$	$4.42^{+1.17}_{-0.92}$	$4.57^{+0.80}_{-0.67}$	$7.51^{+3.09}_{-2.21}$	$3.13^{+0.44}_{-0.38}$
χ^2/DoF	**135.16/127**	**132.26/145**	84.23/59	98.27/95	50.25/37	[215.71/148]
Src3						
$N_{\rm H}{}^{(1)}$	$0.67^{+0.12}_{-0.10}$	$0.81^{+0.14}_{-0.12}$	$0.62^{+0.22}_{-0.18}$	$0.89^{+0.23}_{-0.18}$	$1.20^{+0.62}_{-0.46}$	$0.76^{+0.17}_{-0.14}$
$kT_{\rm in}{}^{(2)}$	1.21 ± 0.07	1.29 ± 0.08	$1.43^{+0.16}_{-0.14}$	$1.24^{+0.11}_{-0.10}$	$1.16^{+0.35}_{-0.23}$	$1.23^{+0.08}_{-0.07}$
$L_{\rm X}{}^{(3)}$	$3.98^{+0.65}_{-0.55}$	$4.80^{+0.84}_{-0.70}$	$5.28^{+1.61}_{-1.23}$	$4.65^{+1.20}_{-0.93}$	$4.84^{+4.31}_{-2.33}$	$4.60^{+0.85}_{-0.70}$
χ^2/DoF	**178.37/144**	**180.34/157**	**70.44/70**	**[172.23/109]**	**32.55/25**	**186.60/132**
Src6						
$N_{\rm H}{}^{(1)}$	$0.38^{+0.04}_{-0.05}$	0.29 ± 0.05	$0.15^{+0.11}_{-0.10}$	0.27 ± 0.06	≤ 0.11	0.26 ± 0.06
$kT_{\rm in}{}^{(2)}$	$1.40^{+0.09}_{-0.07}$	$1.49^{+0.12}_{-0.09}$	$1.75^{+0.38}_{-0.22}$	$1.44^{+0.15}_{-0.11}$	$1.72^{+0.33}_{-0.32}$	$1.57^{+0.17}_{-0.12}$
$L_{\rm X}{}^{(3)}$	$5.61^{+0.71}_{-0.79}$	$4.94^{+0.74}_{-0.83}$	$4.55^{+1.46}_{-1.60}$	$4.56^{+0.86}_{-0.91}$	$5.22^{+2.94}_{-1.31}$	$4.67^{+0.87}_{-0.97}$
χ^2/DoF	**190.03/160**	203.07/152	70.19/63	130.26/109	**21.30/25**	135.52/115
Src7						
$N_{\rm H}{}^{(1)}$	$4.88^{+0.52}_{-0.48}$	$4.98^{+0.54}_{-0.50}$	$4.31^{+0.87}_{-0.74}$	$4.88^{+0.68}_{-0.61}$	$9.30^{+0.10}_{-0.09}$	$9.99^{+31.13}_{-6.90}$
$kT_{\rm in}{}^{(2)}$	$1.45^{+0.13}_{-0.11}$	$1.43^{+0.12}_{-0.11}$	$1.65^{+0.27}_{-0.22}$	$1.37^{+0.15}_{-0.13}$	$0.78^{+0.15}_{-0.12}$	<1.47
$L_{\rm X}{}^{(3)}$	$8.71^{+2.26}_{-1.80}$	$7.97^{+2.05}_{-1.63}$	$8.81^{+4.29}_{-2.83}$	$7.80^{+2.63}_{-1.96}$	$1.55^{+0.85}_{-0.56}$	<13.50
χ^2/DoF	174.77/179	205.22/173	**63.31/78**	120.09/117	-	[70.38/43]
$C-stat/DoF$	-	-	-	-	**276.97/660**	-
Src8						
$N_{\rm H}{}^{(1)}$	$0.45^{+0.05}_{-0.04}$	$0.44^{+0.05}_{-0.04}$	0.49 ± 0.07	0.36 ± 0.04	-	-
$kT_{\rm in}{}^{(2)}$	1.13 ± 0.05	1.00 ± 0.05	0.94 ± 0.05	1.03 ± 0.05	-	-
$L_{\rm X}{}^{(3)}$	$5.30^{+0.62}_{-0.55}$	$3.40^{+0.48}_{-0.42}$	$2.82^{+0.79}_{-0.61}$	$2.65^{+0.62}_{-0.50}$	-	-
χ^2/DoF	**182.51/152**	**128.60/117**	**39.92/42**	53.06/61	-	-

Notes: (1) Absorption column density intrinsic to the source (10^{22} cm^{-2}); (2) Inner disc temperature (keV); (3) Observed 0.3 – 10 keV luminosity (10^{38} erg s^{-1}). All luminosity errors were calculated within a 68% Gaussian uncertainty range. All other errors were calculated within a 90% uncertainty.

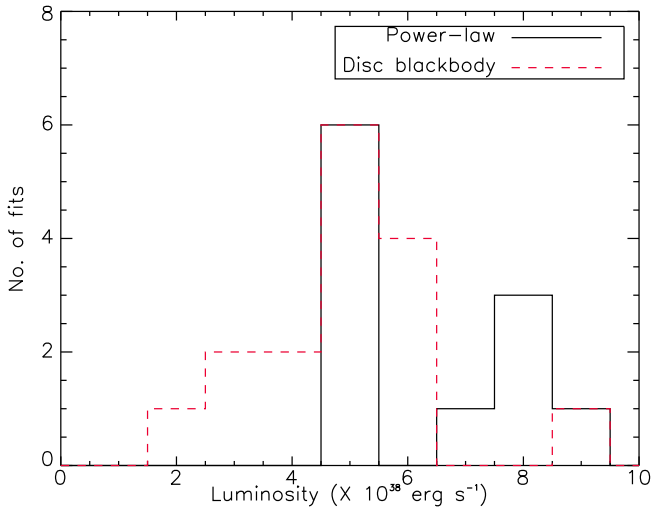

Figure 4.6: Luminosity distribution of the number of successful power-law fits (black) and disc blackbody (red) models.

with the power-law model, and the lower luminosity sources with the disc blackbody model.

Even though in most cases we can't strongly distinguish one best fitting model from the other, we can still measure variation in the spectral shapes from observation to observation. An example of this is illustrated in Figure 4.7, where the ratios of spectral data of Src8 to the best fitting 10542 disc blackbody model of the same source are shown. Clearly the shape of the spectrum changes from observation to observation. A more general example of spectral changes can be seen in Figure 4.8, where we have plotted both source observed and intrinsic luminosity vs. photon index and inner disc temperature for the best fitting power-law and disc blackbody models. Note that the intrinsic luminosity was calculated by setting absorption to zero in the best fitting models. The errors that are displayed in the plots represent a 1σ uncertainty in the parameters shown.

We found a number of trends that can be seen in the parameters of the best fitting models. A very obvious trend is the almost linear decrease with photon index relative to luminosity in Src1, Src3, and Src8. However, when absorption is removed, the photon index is no longer seen to decrease with luminosity. Indeed, the photon index of Src6 is seen to increase with increase in luminosity when absorption

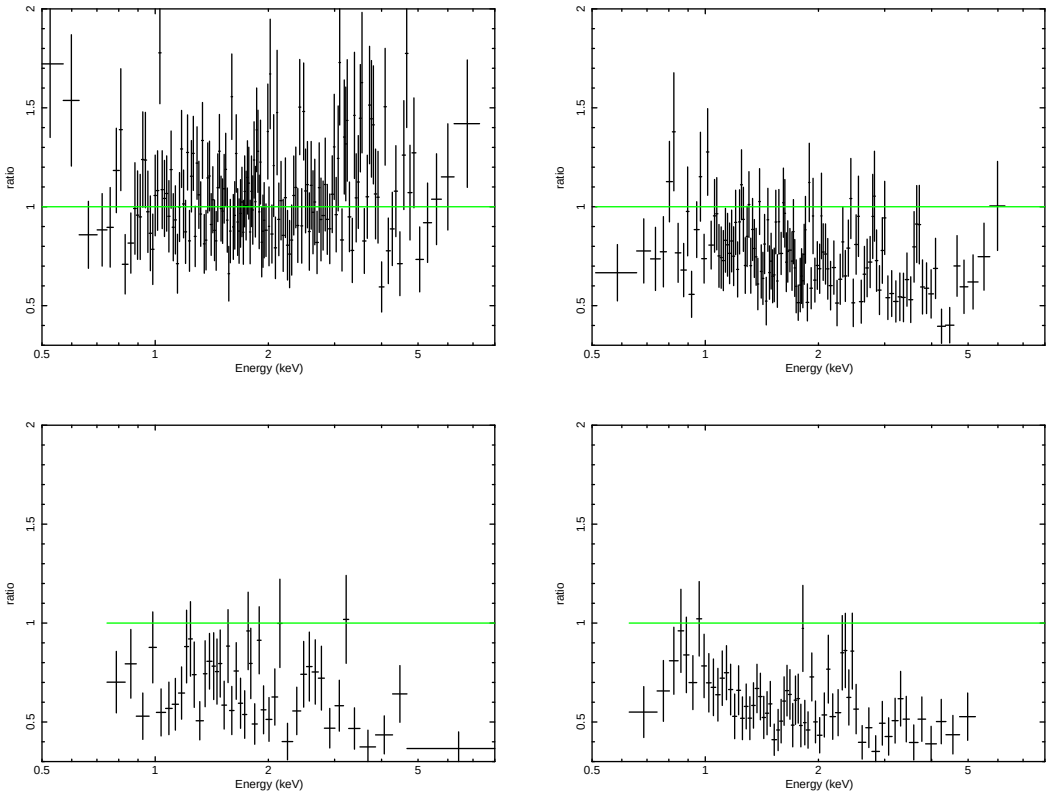

Figure 4.7: From top left to bottom right, the ratio of Src8 spectral data from observation 10542, 10543, 10925, and 10544 to the best fitting 10542 disc blackbody model of the same source. The level of the model in each panel is indicated by the green line.

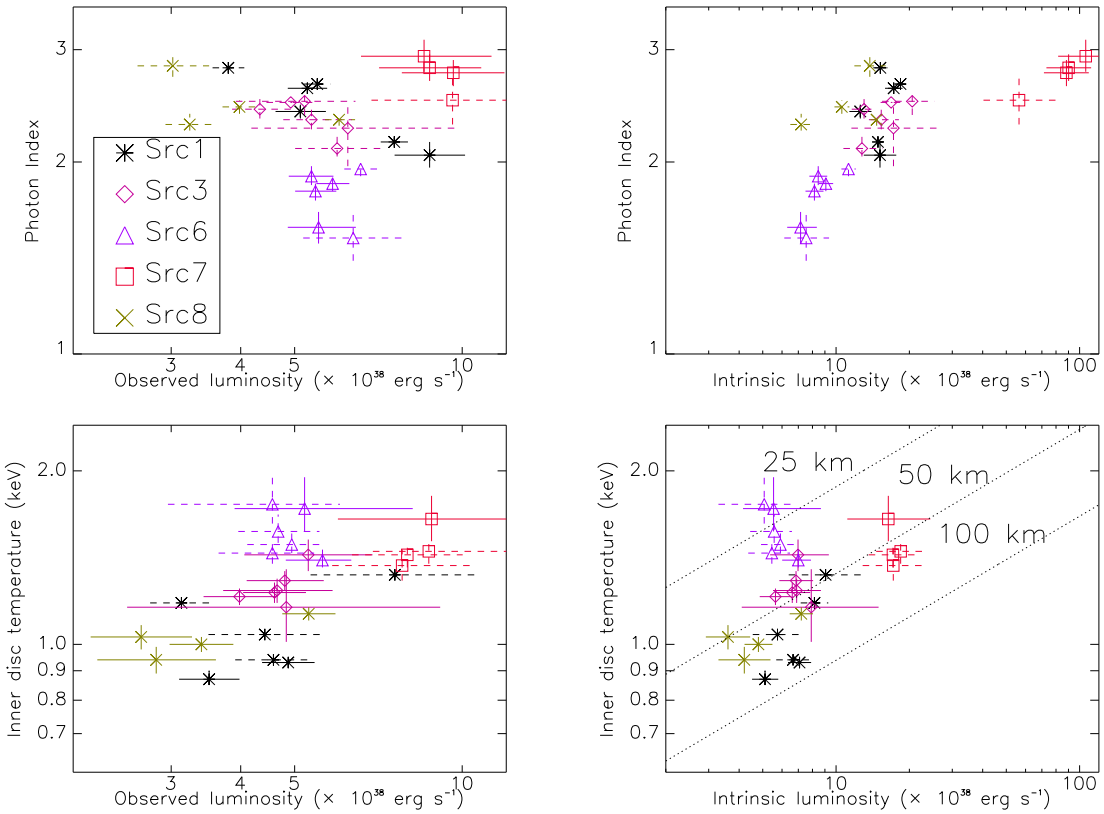

Figure 4.8: Luminosity vs. photon index (*upper*) and inner disc temperature (*lower*) plots of the best fitting power-law and disc blackbody models, respectively, for the five multiply-detected sources unaffected by pile-up. The observed luminosities are the luminosity values in the left hand panels. The intrinsic luminosities are the luminosity values in the right hand panels. The errors plotted in this figure were calculated within a 1σ range. For sources that are best fit by the model that is the subject of each panel, the error bars are represented by solid lines. For sources that are best fit with the other model, error bars are represented by dashed lines. The dotted lines in the bottom right panel represent $L_{\rm X} \propto {\rm T}^4$ tracks for inner disc radius values of 25, 50, and 100 km, corresponding to BH masses of $\sim 2.8\ M_{\odot}$, $\sim 5.6\ M_{\odot}$, and $\sim 11.2\ M_{\odot}$, respectively. Different colours/symbols represent the parameter values for the different sources (see the legend in the top left panel).

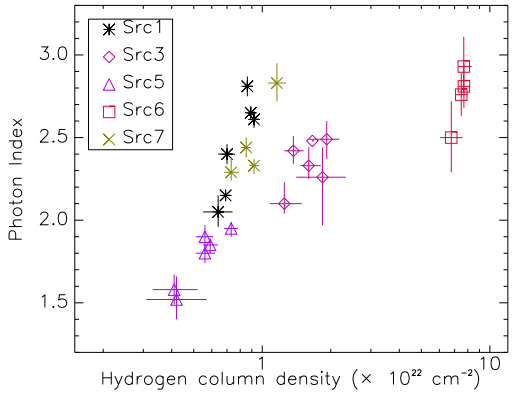

Figure 4.9: The power-law photon index vs. absorption column density of the best fitting source power-law models for the five sources unaffected by pile-up. Errors plotted here were calculated within a 1σ range.

is removed. The same trend was seen by Gladstone & Roberts (2009). They suggest that a likely cause for this is the limited band-pass of the *Chandra* instruments above 5 keV, which does not permit a sufficiently large energy range over which to properly constrain the power-law slope. This limited bandpass could plausibly induce some degeneracy between the slope of the power-law spectrum, and the amount of material needed to produce the turnover in the spectrum. Investigating the relationship between power-law photon index and hydrogen column density in the best fitting models (c.f., Figure 4.9) indicated that higher column density levels match higher photon index values in the case of all 5 sources, thus agreeing with the hypothesis posed above.

Another weak trend that we saw was the increase in inner disc temperature with respect to luminosity, in the case of Src1 and Src8. Unlike the case of power-law photon index, the removal of absorption leads to little relative movement between the luminosities of each source, as was the case with Gladstone & Roberts (2009). The increase in disc temperature is a trend seen in typical Galactic BH binaries (BHBs) in TD state (Done, Gierlinski, & Kubota 2007).

4.4.1.2 Src4

The best fitting spectral parameters for the single luminous detection of Src4 can be seen in Table 4.6. In summary, the best fitting power-law model parameters

Table 4.6: Best fitting XSPEC TBABS*TBABS*PO and TBABS*TBABS*DISKBB model parameters for Src4

TBABS*TBABS*PO	
$N_{\rm H}{}^{(1)}$	$4.25^{+0.37}_{-0.41}$
Γ	$1.34^{+0.12}_{-0.14}$
$L_{\rm X}{}^{(2)}$	$2.39^{+0.28}_{-0.32}$
χ^2/DoF	**179.35/173**
TBABS*TBABS*DISKBB	
$N_{\rm H}{}^{(1)}$	3.44±0.11
$T_{\rm in}{}^{(3)}$	$3.45^{+0.55}_{-0.44}$
$L_{\rm X}{}^{(2)}$	$2.26^{+0.78}_{-0.55}$
χ^2/DoF	181.33/173

Notes: (1) Absorption column density intrinsic to the source (10^{22} cm^{-2}); (2) Observed 0.3 – 10 keV luminosity (10^{39} erg s^{-1}); (3) Disc blackbody inner disc temperature (keV). All luminosity errors are calculated within a 68% Gaussian uncertainty range. All other errors are calculated within a 90% uncertainty.

represent a hard, absorbed spectrum, with a photon index of $\Gamma \sim 1.3$ and a column density of $N_{\rm H} \sim 4.3 \times 10^{22}$ cm^{-2}. The best fitting disc blackbody model parameters imply a very hot inner disc, with a best fitting temperature of $T_{\rm in} \sim 3.5$ keV, and a best fitting column density value of $\sim 3.4 \times 10^{22}$ cm^{-2}. Statistically, the best fitting power-law and disc blackbody models are indistinguishable from one another.

4.4.2 The two brightest sources

The results of the spectral fitting for Src2 and Src5 can be seen in Table 4.7. In summary, Src2 is consistently best fit with a hard power-law with a photon index ranging from $\Gamma \sim 1.2$ – 1.6 and column density ranging from ~ 1.2 – 1.6×10^{22} cm^{-2}. These values of Γ are significantly harder than those found in XRBs in the hard state. The best fitting inner disc temperatures are particularly high, ranging from ~ 2 – 3.4 keV, with column density levels ranging from ~ 0.8 – 1.3×10^{22} cm^{-2}.

Determining the best fitting models for the spectra of Src5 was made more difficult by the high levels of soft excess in the spectra, as well as limited number of photon counts that the annular apertures provided. During the first three observations, the best fitting disc blackbody models were found to be unconstrained, with

Table 4.7: Best fitting XSPEC TBABS*TBABS*PO and TBABS*TBABS*DISKBB model parameters for Src2 and Src5

	10542	10543	10925	10544	11800	10545
Src2						
TBABS*TBABS*PO						
$N_{\rm H}^{(1)}$	$1.24^{+0.16}_{-0.13}$	$1.79^{+0.18}_{-0.14}$	$1.64^{+0.22}_{-0.18}$	$1.61^{+0.21}_{-0.17}$	$1.65^{+0.38}_{-0.31}$	$1.64^{+0.20}_{-0.10}$
Γ	$1.51^{+0.11}_{-0.10}$	$1.53^{+0.11}_{-0.09}$	$1.63^{+0.14}_{-0.12}$	$1.33^{+0.13}_{-0.11}$	$1.21^{+0.22}_{-0.18}$	$1.55^{+0.12}_{-0.10}$
$L_{\rm X}^{(2)}$	$3.71^{+0.38}_{-0.30}$	$6.40^{+0.67}_{-0.48}$	$2.73^{+0.36}_{-0.25}$	$2.29^{+0.28}_{-0.20}$	$3.73^{+0.81}_{-0.54}$	$1.71^{+0.20}_{-0.14}$
χ^2/DoF	**153.74/160**	**246.07/210**	**127.58/123**	**171.36/157**	**65.69/61**	**167.86/168**
TBABS*TBABS*DISKBB						
$N_{\rm H}^{(1)}$	$0.84^{+0.07}_{-0.09}$	$0.85^{+0.06}_{-0.08}$	$1.15^{+0.11}_{-0.13}$	1.18 ± 0.09	$1.27^{+0.17}_{-0.15}$	$1.16^{+0.10}_{-0.12}$
$T_{\rm in}^{(3)}$	$2.24^{+0.31}_{-0.18}$	$2.28^{+0.26}_{-0.15}$	$2.00^{+0.28}_{-0.16}$	$2.97^{+0.52}_{-0.36}$	$3.41^{+1.29}_{-0.74}$	$2.18^{+0.28}_{-0.16}$
$L_{\rm X}^{(2)}$	$3.26^{+0.57}_{-0.85}$	$5.64^{+0.82}_{-1.26}$	$2.35^{+0.44}_{-0.62}$	$2.10^{+0.62}_{-0.57}$	$3.46^{+2.34}_{-1.49}$	$1.49^{+0.25}_{-0.37}$
χ^2/DoF	180.02/160	271.42/210	139.43/123	194.47/157	69.47/61	180.93/168
Src5						
TBABS*TBABS*POWER-LAW						
$N_{\rm H}^{(1)}$	$9.02^{+2.72}_{-2.77}$	$10.42^{+3.19}_{-3.90}$	$18.02^{+4.38}_{-4.67}$	$18.85^{+4.66}_{-4.47}$	$17.86^{+8.63}_{-6.80}$	$29.13^{+2.55}_{-3.13}$
Γ	$0.22^{+0.20}_{-0.25}$	$0.35^{+0.30}_{-0.31}$	$0.65^{+0.39}_{-0.41}$	$1.21^{+0.46}_{-0.42}$	$1.46^{+0.94}_{-0.79}$	$2.15^{+0.26}_{-0.32}$
$L_{\rm X}^{(2)}$	$1.50^{+0.56}_{-0.51}$	$0.82^{+0.34}_{-0.37}$	$1.96^{+1.11}_{-0.84}$	$0.53^{+0.36}_{-0.22}$	< 0.97	$0.35^{+0.10}_{-0.12}$
χ^2/DoF	**132.54/127**	116.90/120	102.29/87	94.09/93	46.94/38	**[254.30/195]**
TBABS*TBABS*DISKBB						
$N_{\rm H}^{(1)}$	$12.83^{+1.61}_{-1.47}$	$13.30^{+1.05}_{-0.99}$	$18.30^{+1.99}_{-1.84}$	$17.27^{+2.03}_{-1.87}$	$15.96^{+2.67}_{-5.74}$	$23.76^{+1.86}_{-1.98}$
$T_{\rm in}^{(3)}$	<1000	<1000	<1000	$4.82^{+2.66}_{-1.03}$	$3.50^{+7.60}_{-1.40}$	$2.59^{+0.50}_{-0.31}$
$L_{\rm X}^{(2)}$	<3967	<1457	<812	<1.17	<1.17	<0.44
χ^2/DoF	137.84/127	**114.94/120**	**102.27/87**	**92.94/93**	**46.09/38**	[260.80/195]

Notes: (1) Absorption column density intrinsic to the source (10^{22} cm^{-2}); (2) Observed source 0.3 – 10.0 keV luminosity (10^{40} erg s^{-1}); (3) Disc blackbody inner disc temperature (keV). All luminosity errors were calculated within a 68% Gaussian uncertainty. All other errors were calculated within a 90% uncertainty.

inner disc temperatures all hitting the 1000 keV model limit, and luminosities also very poorly constrained. On the other hand, the best fitting power-law models were found to be more reasonable, albeit with photon indices on the low side. The best fitting model parameters range from $\Gamma \sim 0.2 - 2.2$ and $N_{\rm H} \sim 9 - 29 \times 10^{22}$ cm^{-2} in the case of the power-law model, and $T_{\rm in} \sim 2.6 - 4.8$ keV and $N_{\rm H} \sim 18 - 24 \times 10^{22}$ cm^{-2} in the case of the disc blackbody model (where constrained). It is worth reiterating that different apertures were used in the extraction of spectral and response data in the case of observations 11800 and 10545.

As was done with the less bright sources, we investigated the variations in the best fitting source models. As noted above, Src2 is constantly best fit with a power-law model. When we looked at how the best fitting parameters of Src2 vary with both observed and intrinsic luminosity, we saw no noticeable trend in either photon index or inner disc temperature with luminosity. With Src5, neither model was statistically distinguishable from the other. As with Src2, no trend was seen in the model parameters with luminosity.

4.5 Long term variability

Spectral analysis indicated that variability is present in the X-ray luminosity of a number of the sources. This variability is illustrated in Figures 4.10 and 4.11. Note that we have excluded Src4 from this analysis, because only 1 observed luminosity value for the source was obtained. The most significant changes in observed luminosity can be seen in Src8, where the luminosity decreases from a peak of $\sim 5 \times 10^{38}$ erg s^{-1} to a level below the detector limit over the course of the 6 observations. A similar decrease in luminosity is seen in Src7, where the luminosity drops from $\sim$ ULX range in the first 4 observations to a luminosity of $\sim 2 \times 10^{38}$ erg s^{-1} in the second last observation.

We further investigated this variability by calculating the significance in the difference in photon count rate between observations via the equation

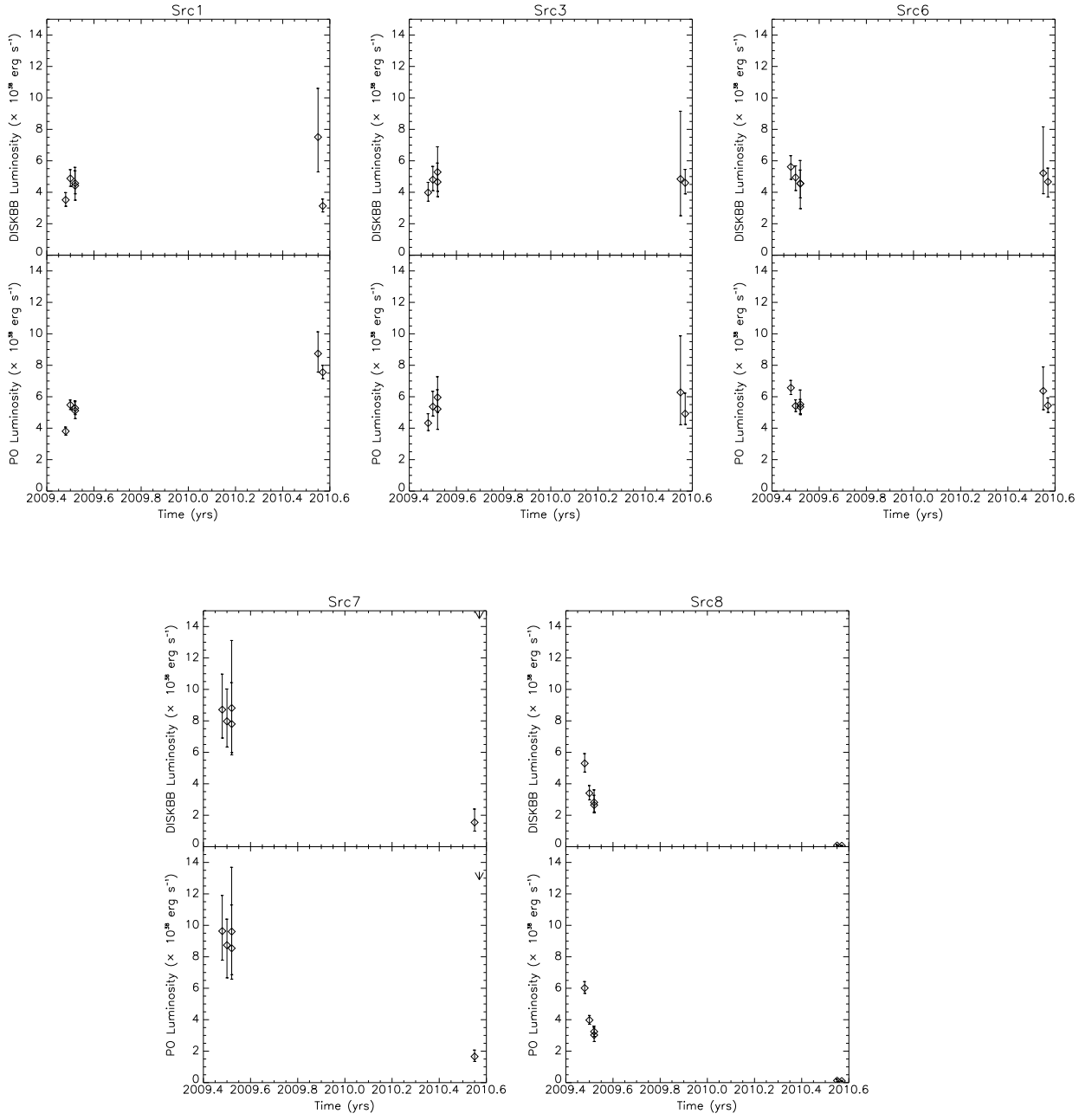

Figure 4.10: From top left to bottom right, the 0.3 - 10.0 keV band observed luminosity of Src1, Src3, Src6, Src7, and Src8, calculated from the best fitting power-law and disc blackbody model fluxes. The errors were calculated withing a 68% Gaussian confidence range.

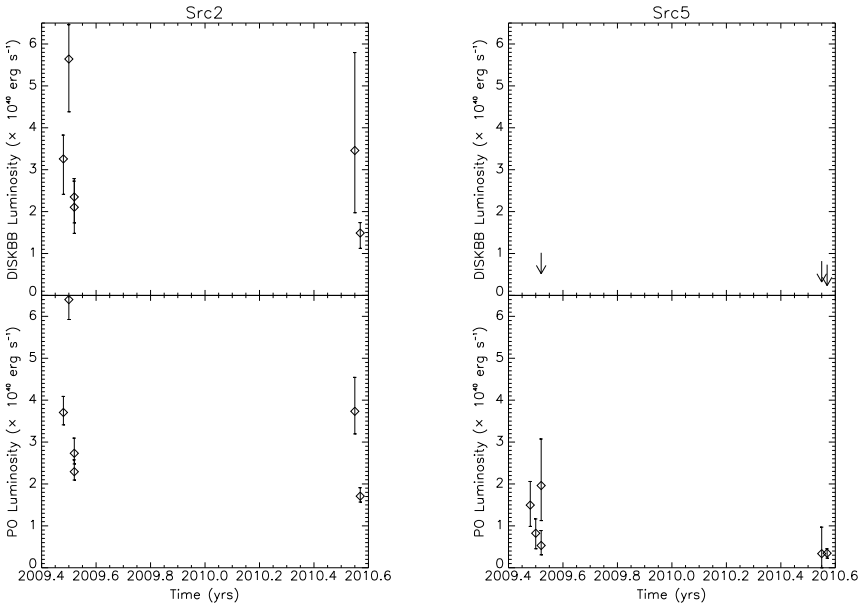

Figure 4.11: The 0.3 – 10.0 keV band luminosity of Src2 and Src5, calculated from the best fitting power-law and disc blackbody model fluxes. The errors were calculated withing a 68% Gaussian confidence range.

$$S_{\rm CR} = \max_{i,j}|CR_i - CR_j|/\sqrt{\sigma^2_{CRi} + \sigma^2_{CRj}} \tag{4.1}$$

as per Chiang & Kong (2011), where CR_i is the 0.3 – 10 keV photon count rate and σ_{CRi} is the corresponding count rate error. We further investigated this variability by quantifying the intensity of count rate variations, as the ratio R of maximum count rate to minimum count rate, over the course of the six observations. When we performed this more quantitative variability analysis, we found that all of the sources display an $S_{CR} > 15$ and $R > 6$. The source S_{CR} values, as well as their count rate ratios, can be seen in Table 4.8.

With an S_{CR} value of 33.5, Src2 displays the most significant levels of long term luminosity variability amongst the seven sources. However, Src7 displays the largest drop in flux throughout the 6 observations, with $R = 104$. A large drop in flux is also seen in Src8, with $R = 97.4$. Almost as significantly variable as Src2 is Src5, with an S_{CR} value exceeding that of Src7. Src1 shows a high significance in variability, with

Table 4.8: Long term source variability results

Source	$S_{CR}{}^{(1)}$	$R^{(2)}$
Src1	26.4	11.6
Src2	33.5	18.0
Src3	14.5	6.95
Src5	28.9	6.31
Src6	16.3	6.40
Src7	15.1	104
Src8	30.9	97.4

Notes: (1) S_{CR} value calculated using the observed photon count rates of the source; (2) Count rate ratio, calculated using the observed photon count rates of the sources.

an S_{CR} value only exceeded by those of Src2 and Src5. Although we only obtained a single constrained count rate value for Src4, the photon count estimates for the source as well as the source count rate during observation 10545 indicate what is likely the highest level of long-term variability in the sample.

4.5.1 Intra-observational variability

The results of the lightcurve variability tests can be seen in Table 4.9. Note that the errors quoted in this table were calculated as per Vaughan et al. (2003). We found that Src1, Src2, Src3, Src4, and Src5 display a significant deviation from a constant count rate at least once throughout the 6 observations (i.e., with null hypothesis probabilities < 0.05). Src1 shows signs of variability only during the observations of 2009. On the other hand variability is seen in Src3 throughout both 2010 observations, but not in 2009. It is worth noting that these changes in short-term variability may be an indication of long term physical changes in the two sources. The count rate in Src2 is seen to change stochastically from being consistent with a constant rate to being variable throughout the observations. During observation 10545, Src4 displays a very high level of short-term variability. Src5 is highly variable throughout the majority of observations. No variability is seen in Src6, Src7, or Src8.

Table 4.9: Intra-observational source variability results

Obs. ID	Bin size (ks)	No. of bins	NHP[(1)]	$F_{\rm var}$[(2)]
Src1				
10542	1.0	120	0.02	7±3
10543	1.0	119	0.00	18±2
10925	1.0	44	0.01	13±4
10544	1.0	73	0.04	10±3
11800	1.0	16	0.56	-
10545	1.0	95	0.38	-
Src2				
10542	1.0	120	0.38	<14
10543	1.0	119	0.003	8±2
10925	1.0	44	0.08	6±3
10544	1.0	73	< 0.001	13±2
11800	1.0	16	0.06	9±4
10545	1.0	95	0.34	<9
Src3				
10542	1.0	120	0.34	<14
10543	1.0	119	0.26	<12
10925	1.0	44	0.6	-
10544	1.0	73	0.33	<14
11800	1.0	16	0.02	23±8
10545	1.0	95	0.06	10±5
Src4				
10542	-	-	-	-
10543	-	-	-	-
10925	-	-	-	-
10544	-	-	-	-
11800	-	-	-	-
10545	1.0	95	0.00	28±2

Table 4.9: Intra-observational source variability results – Continued

Obs. ID	Bin size (ks)	No. of bins	NHP[(1)]	$F_{\rm var}$[(2)]
Src5				
10542	1.5	79	< 0.001	21±4
10543	1.7	69	< 0.001	27±4
10925	1.0	44	0.04	13±4
10544	1.3	52	0.01	16±4
11800	1.0	16	0.25	<20
10545	1.0	95	0.00	14±2
Src6				
10542	1.0	120	0.39	-
10543	1.0	119	0.99	-
10925	1.0	44	0.14	9±8
10544	1.0	73	0.19	7±6
11800	1.0	16	0.51	-
10545	1.0	95	0.37	<15
Src7				
10542	1.0	120	0.78	-
10543	1.0	119	0.85	-
10925	1.0	44	0.65	-
10544	1.0	73	0.33	<25
11800	-	-	-	-
10545	-	-	-	-
Src8				
10542	1.0	120	0.71	-
10543	1.0	119	0.73	-
10925	1.2	37	0.80	-
10544	1.3	56	0.20	-
11800	-	-	-	-
10545	-	-	-	-

Notes: [(1)] Null hypothesis probability of the lightcurve being consistent with constancy; [(2)] rms fractional variation (%), calculated as per Vaughan et al (2003)

When we looked for fractional variation in the sources, we found a consistency between those objects that display variable count rates, and those that display significant rms fractional variation. Src1, Src2, and Src3 display rms fractional variation levels ranging from 10 – 20% when variable, although the variation in Src3 is only significant to within a maximum of 3σ. With an rms fractional variation of 28 ± 2 %, Src4 is the most variable source in the sample. Almost as variable is Src5, which displays an rms fractional variation $> 20\%$ throughout 2 observations, and a variation $> 10\%$ throughout 3 of the remaining 4 observations. The lightcurves of

the most significantly variable detections of Src1, Src2, Src4, and Src5 are shown in Figure 4.12. We further investigated the variability in these 4 sources by extracting PDS from the data which displayed the highest levels of variation. However, no significant red noise power was detected in these spectra. Therefore, we do not report on any PDS analysis in this work.

4.6 Discussion

4.6.1 A possible state transition

In a previous section, we investigated the spectral properties of 8 X-ray point sources within M82, 5 of which were detected with a high number of photon counts in at least 4 observations, and display X-ray fluxes that are low enough not to be effected by pile-up. Fitting the spectra of these 5 sources yielded both best fitting models and X-ray luminosities implying that the sources are within the high Eddington accretion rate fraction BH regime. In the majority of cases, either short-term variability, long-term variability, or both, agree with this hypothesis.

Because we have assumed that the 5 X-ray sources fall into the category of BHB, we have taken the next logical step in our analysis, and compared the best fitting model parameters of the sources' spectra to those seen in those seen in Galactic BHBs, as per McClintock & Remillard (2006). Three sources display photon indices > 2.4 during a number of their observations. This is analogous to them being in the SPL state as described by McClintock & Remillard (2006). Similarly, four of the sources display photon indices within the XRB hard range (i.e., $\Gamma \sim 1.7 - 2.1$, McClintock & Remillard 2006) during at least one of their observations. The inner disc temperatures of our sources are seen to reach outside the limits as defined by the TD state (0.7 – 1.1 keV, McClintock & Remillard 2006). However, they are similar to those measured in ULXs fit with simple disc models (e.g, Makishima et al. 2000).

In a study of the ULX population of NGC 4485/4490, Gladstone & Roberts (2009) suggested that a state transition may be occurring at a luminosity of $\sim 2 \times 10^{39}$ erg s^{-1} within their source sample, from the power-law-like SPL state to a

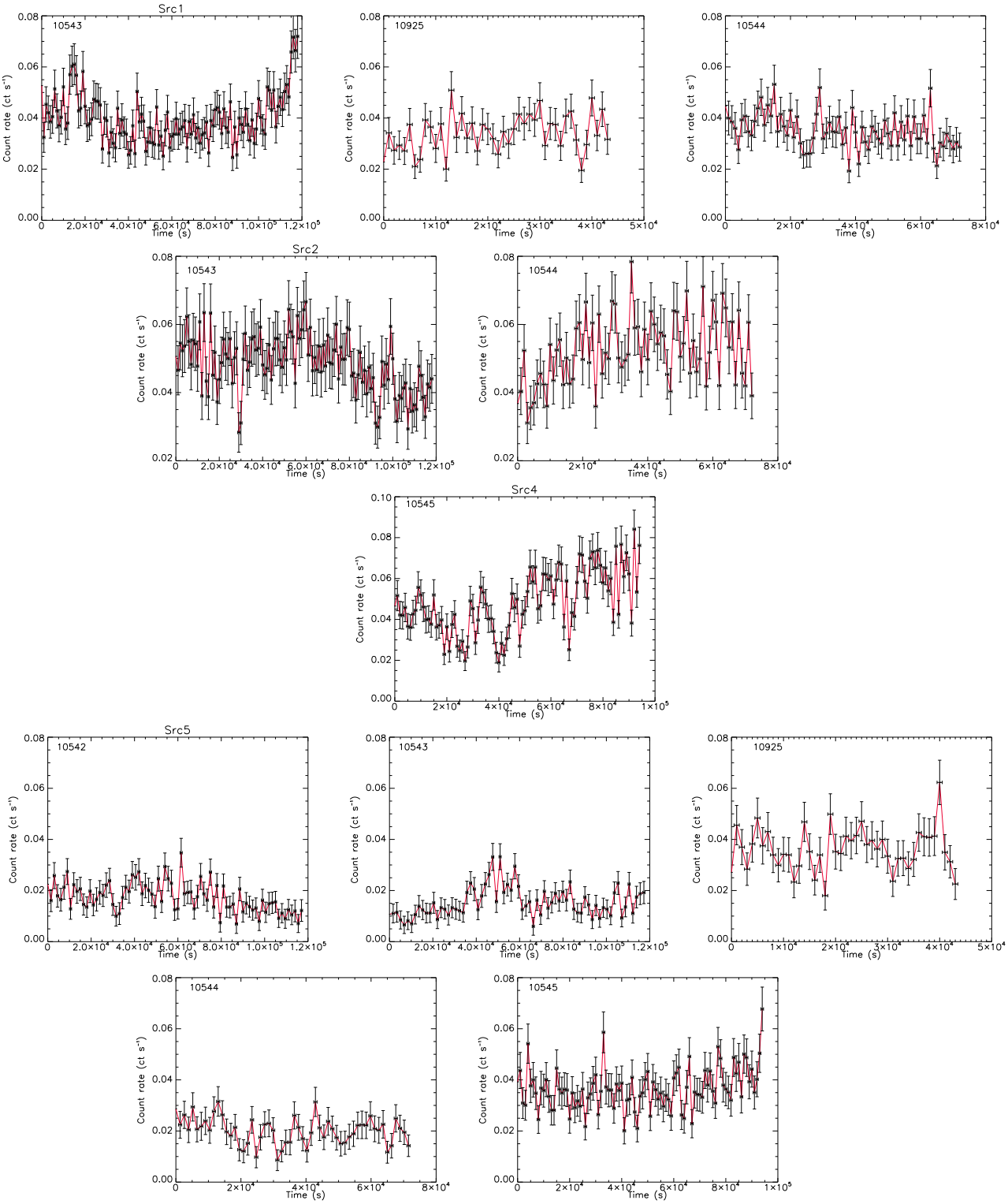

Figure 4.12: The lightcurves of Src1, Src2, Src4, and Src5 that display the most significant rms fractional variation. The top row displays the lightcurves of Src1 from the observations 10543, 10925, and 10544. The second row displays the lightcurves of Src2 from the observations 10543 and 10544. The third row displays the lightcurve of Src4 from the observation 10545. The bottom 2 rows display the lightcurves of Src5 from the observations 10542, 10543, 10925, 10544, and 10545. Note that the lightcurves of Src2 and Src5 were extracted from annular apertures, thus displaying a comparatively low photon count rate for their high flux values.

disc-like super-Eddington state. When comparing the best fitting models to luminosities in our source sample, we found that, in general, the power-law model is best fit to the spectra with highest luminosities, and that the blackbody models best fit the lower luminosity spectra (c.f., Figure 4.6). However, our sources are displaying luminosities considerably lower than those of Gladstone & Roberts (2009). Therefore, this result indicates the possibility of a state transition at lower luminosities, from the TD state to the SPL state, before the SPL to super-Eddington state transition. However, the overall luminosity-model trend seen within the sample is not necessarily seen in the individual sources. Below, we explore the spectral and timing variability of the individual sources.

The spectral shape of Src1 can either be described by a simple power-law with a photon index ranging from $\Gamma \sim 2$ – 2.8, or a disc blackbody model with an inner disc temperature ranging from $T_{\rm in} \sim 0.9$ – 1.2 keV. Significant levels of variability can be seen in the source over the first four observations, while the source displays a soft spectrum. This may indicate that the source is accreting in the SPL state. Previously, Jin, Feng, & Kaaret (2010) reported Src1 to simultaneously display a soft spectrum ($\Gamma \sim 2.6$) and significant short-term variability. During the final 2 observations, the source is seen to become spectrally harder, with no significant levels of variability, similar to a result that was also reported by Jin, Feng, & Kaaret (2011). This seems counter-intuitive, as the shape of the spectrum (with $\Gamma \sim 2$) indicates the hard accretion state, whereas BHBs in this state typically shows signs of variability. It is more likely that the source is experiencing accretion in a disc-dominated SPL state.

The spectrum of Src3 is consistently best fit with a disc blackbody model. The inner disc temperature of Src3 is ~ 1.2 keV throughout the 6 observations. Short-term variability in the source is only seen during observation 11800, but is only significant to within $\sim 3\sigma$. Such spectral and timing properties could be the signature of a BHB accreting in the TD state.

Src6 displays a spectrum that is either best fit with a power-law with a hard Γ value ranging from 1.5 – 2, or a disc blackbody with an inner disc temperature of $kT \sim 1.4$ – 1.7 keV. No significant spectral or temporal variability is seen in

this source throughout the 6 observations. The spectral hardness is an indicator of the hard state. However, this does not bode well for either the lack of short-term variability, or the inner disc temperature of the source. It may be that the apparent hardness of the spectrum is a result of an underestimation of absorption in the spectral fitting. Another possibility is that Src6 is a luminous accreting NS binary (see Done, Gierlinski, & Kubota 2007 for a review), and is thus displaying a lack of short-term variability and a relatively high temperature which may be the result of hot emission from the surface of the star via inverse Compton scattering of photons from the stellar surface off high energy electrons within the accretion flow.

The spectral shape of Src7 is likely effected by the high levels of absorption that the source experiences. The slope of its spectrum is consistently > 2.3. Alternatively, the inner disc temperature ranges from 1.4 – 1.7, like that of Src6. No short term variability is seen in Src7. However, the luminosity of the source is fainter by a factor of ~ 4 during the second last observation, thus making it one of the most long-term variable sources in our sample. Both the high photon index and the inner disc temperature of the spectrum suggests that the source is accreting in the SPL state.

When fit with a power-law, Src8 displays a soft spectral shape ($\Gamma \sim 2.3 - 2.8$). The inner disc temperature of the source is consistently ~ 1 keV, when fit with a disc blackbody model. As with Src6 and Src7, Src8 experiences no significant short-term variability throughout any of the observations. The lack of intra-observational variability, coupled with the disc-like spectrum of the source suggests that Src8 is accreting in the TD state. The luminosity of the source appears to be fading throughout the first four observations. By the fifth observation, the luminosity has faded to levels beyond the minimum threshold of the *Chandra* ACIS instrument, thus displaying the properties of a candidate transient source (e.g., Chiang & Kong 2011). Another point of evidence which supports the transient candidacy of Src8 is the shape of the long term lightcurve (see Figure 4.10), which is similar to the decay profile of a classic Galactic BH transient.

To summarise, even though a state transition appears to be possibly occurring in the population as a whole, this transition is not obvious in any of the individual

sources. The bi-modality seen in Figure 4.6 is mostly due to the fact that certain sources with consistently higher luminosities and spectra best fit with a power-law model (e.g., Src7 during the 2009 observations), and others with consistently lower luminosities and spectra best with a disc blackbody model (e.g., Src3). The limiting factor in this scenario is that there are only 5 sources in our sample. With a larger sample, investigating the possibility of a state transition at luminosities just below the Eddington limit would be significantly easier.

4.6.2 Our results in the context of other galactic population studies

Our study of the population of X-ray sources in M82 is not the first of its kind. A similar study was performed by Jenkins et al. (2004), in which they investigated the spectral and timing properties of the 14 most luminous X-ray point sources in the galaxy M101. In that work, the authors performed their investigation using high quality data from both *XMM-Newton* and *Chandra* observations of the galaxy. Their results indicated that the sample of highly luminous X-ray sources are heterogeneous in their properties, although some sources share similar qualities to others. This result is similar to what we found in our sample of sources. That being said, it can be seen that a number of the sources from both samples share similar properties. For example, out of the 9 sources whose spectra were fit with a single component phenomenological model (i.e., either a power-law or disc blackbody model) by Jenkins et al. (2004), 5 were seen to be displaying signature spectral and timing properties of the TD state. Of our smaller sample of sources, 2 (Src3 and Src8) are seen to display similar properties. The remaining 4 sources in M101 were seen to have properties like those of an XRB in the SPL state, similar to 3 of our 5 sources. Src7, which is one of the possible SPL state sources in our sample, was fit with a highly absorbed power-law + MEKAL model, having similar best fitting parameters to those of XMM3. It was suggested by Jenkins et al (2004) that the MEKAL component in the best fitting model of XMM3 may be attributed to photoionised plasma, if the companion is a high mass star. Note that this is not likely for the 2 sources in our sample that display such a spectral component,

since they are both located in regions of obvious diffuse emission (c.f., Figure 4.5). Although such similarities can be drawn from the spectral and timing properties of some of the sources, a significant number of sources in the M101 sample bear no resemblance to the sources in M82. A prime example of such a source is XMM7, which has been identified as a SSS candidate. With a best fitting DISKBB model inner disc temperature of ~ 0.2, this source possesses a spectrum like none seen in the sources of M82. It is unlikely that such an object would be observed in M82, since the column density of the galaxy is so high.

From an overall point of view, a number of differences can be seen between both samples of X-ray sources. One such difference is the lack of spectral variation in the sources in M101. Jenkins et al. (2004) reported that no significant signs of spectral variability were seen in between the *Chandra* and *XMM-Newton* observations, which were separated by ~ 2 years. On the other hand, some significant spectral variation was seen in a number of the sources in our sample. Another difference is the number of sources in each sample that display significant levels of long term variability. From the $5 \sim$ Eddington sources that we have investigated, only 3 display significant levels of variability over long time scales. In contrast to this, 11 of the 14 sources in M101 were seen to display high levels of long-term variability. A similar number of transient candidates can be seen in both samples, however, with 1/5 of our sources, and 2/14 of the sources in M101, displaying this behaviour. However, the low number of sources in both samples implies that statistically significant differences cannot be obtained. Even so, an important similarity can be drawn from the two samples of X-ray sources, which is that the spectral and timing properties of the sources, coupled with their high observed luminosity values, indicate that they are good candidate stellar-mass BHs at the upper end of the sub-Eddington luminosity regime.

4.6.3 The three brightest sources

In studying the spectral properties of Src2, we found that the source is consistently best fit with an absorbed power-law model with photon index ranging from $\Gamma \sim 1.2$ – 1.7. Such a hard photon index in the *Chandra* spectrum of Src2 has been seen in

previous observations (e.g., Swartz et al. 2004; Kaaret et al. 2009). They clearly do not agree with the significantly softer photon index that has been reported by Fiorito & Titarchuck (2004) or Dewangan et al. (2006), thus agreeing with the observation that the spectral shape of Src2 changes dramatically over extended periods of time. The long term variability properties that we found Src2 reflect the level of variability that has previously been observed within the source (Ptak & Griffiths 1999; Kaaret et al. 2001; Matsumoto et al. 2001; Chiang & Kong 2011). Historically, Src2 has been seen to display very high levels of short-term variability. In particular, the *XMM-Newton* and *RXTE* observations of Src2 indicated the presence of QPOs in the PDS of the source (Strohmayer & Mushotzky 2003; Fiorito & Titarchuck 2004; Feng & Kaaret 2007). Short term variability is also detected throughout the 6 *Chandra* observations, albeit without the presence of a QPO. However, our variability results come from a frequency band much lower than those of previous results ($\sim 10^{-5}$ – 10^{-3} Hz vs. $\geq 10^{-3}$ Hz), which likely explains the lack of a QPO in the PDS. It must also be noted that the lightcurves of Src2 were extracted from annular apertures, thus reducing lightcurve S/N.

The spectral and timing properties of Src4 have been investigated in a number of studies. Spectrally, the source has been reported to be quite hard, with a photon index ranging from $\Gamma \sim 1.3$ – 1.7 (e.g., Kong et al. 2007; Feng et al. 2010), values which are consistent with our single detection. Src4 has also been recognised as a source which displays high levels of short-term variability. Feng et al. (2007) reported the presence of a low frequency QPO in the PDS of the source. Although we did not detect a QPO in the PDS of the source, we still saw that Src4 displays the highest levels of short-term variability in the sample. High levels of long-term variability of Src4, previously reported by Feng & Kaaret (2007) and Chiang & Kong (2011), are evident in the fact that the source went from being extremely dim throughout the first 5 observations to having an observed luminosity of $\sim 2 \times 10^{39}$ erg s^{-1} during the final observation.

Very little previous study has been undertaken on the spectral and timing properties of Src5. However, the properties of the source that we have seen can be put into some historical context. Kong et al. (2007) performed a spectral study of Src5.

Their analysis indicated that the best fitting spectral model for the source was a power-law with a photon index ranging from $\Gamma \sim 0.6 - 2.2$. Our spectral analysis of the same source agrees with these varying Γ values. The levels of long-term variability that were detected in the source throughout the 6 observations are significant, reflecting previously observed X-ray variability levels seen within the source (e.g., Chiang & Kong 2011).

4.7 Summary

Thanks to the richness of data obtained from the *GNOMES* $\sim$ half Ms observation of M82, we have been afforded the opportunity to investigate the X-ray spectral and timing properties of the 8 brightest X-ray binaries in M82, including the famous M82 X-1. Our analysis of the 5 less bright sources indicates that the sample is heterogeneous, but all of the sources display spectral and timing properties that are likely similar to those of canonically accreting XRBs. A possible transition from the TD state to the SPL state was seen among this source sample, although none of the individual sources displayed such a state transition. All of these sources display significant long-term variability, and one of the 5 sources is a transient candidate. The 3 remaining sources are seen to display similar spectral shapes and long-term variability levels to those that have been seen in previous observations. Significant levels of short-term variability were detected in M82 X-1 throughout 2 of the 6 *Chandra* observations; however, out observations covered a lower frequency regime than previous work. Hence it was no surprise that QPOs are not detected in this or any other object. The remaining 2 luminous ULXs near the nucleus of M82 also showed high levels of short-term variability; however, while one was very luminous in 2009 with $L_{\rm X} > 10^{40}$ erg s^{-1}, the other remained in relative quiescence until our last observation in 2010, when it re-brightened to ULX luminosities.

This work has demonstrated the range of results that can be revealed by studies dedicated the properties of galaxies with rich XRB and ULX populations. The results from this work will help point to future programmes designed to improve our understanding of these systems.

Chapter 5

Conclusion

In this thesis we have investigated the properties of a number of point-like X-ray emitting sources located in star forming galaxies, either by analysing the X-ray properties of the sources themselves, or by studying counterpart sources detected in the optical band. This chapter presents a conclusion to this work by summarising the main results that we have found, and by highlighting a number of possible future studies, based on these results.

5.1 Summary of results

5.1.1 The source of emission from the brightest X-ray galaxies

The goal of the study presented in Chapter 2 was to determine whether galaxies that are both X-ray bright ($L_{\rm X} > 10^{42}$ erg s^{-1}) and display no clear optical signatures of AGN activity are truly powered by star formation, or by an optically undetected AGN. In an attempt to attain this goal, we investigated the X-ray properties of 3 sources that were taken from a cross correlation of the *SDSS*-DR5 and 2XMMp-DR0 catalogues, that have no optical signatures of AGN activity, X-ray luminosities exceeding 10^{42} erg s^{-1}, and, crucially, relatively good X-ray data (a few hundred to few thousands of counts). This investigation was performed using data from 9 observations of the three sources, taken using both *XMM-Newton* and *Chandra*. To

test for the presence of activity within the nuclei of these sources, we adopted 4 tests: point spread analysis; intra-observational variability analysis; spectral analysis; and long term spectral and timing variability analysis. The results of these tests infer the presence of AGN activity within the nuclei of the galaxies. A number of possibilities have been suggested as to the cause of the lack of detection of AGN activity in the optical band. The most likely cause for this is that the AGN are being optically diluted by emission related to star formation within their host galaxies. In summary, the results of this study imply that the common assumption that galaxies which display luminosities $> 10^{42}$ erg s^{-1} host AGN appears safe.

5.1.2 The age constraints of the X-ray sources in NGC 922

In Chapter 3, we present the age constraints on 13 bright X-ray point sources in the metal-rich star forming galaxy NGC 922, obtained by assuming that the clusters located closest to the X-ray sources are the parent clusters of the sources. The optical colour analysis of these clusters indicate that the X-ray sources located closest to recent star formation (identified by the presence of Hα emission) have the youngest age constraints, with ages of the sources increasing precipitously with distance to star formation. This result agrees with the predictions of the latest XRB and stellar population synthesis models. A caveat to these results is that a number of the X-ray sources are likely to display high levels of absorption, and therefore extinction, which may be hiding young stellar clusters that are located closer to the X-ray sources.

5.1.3 The properties of the brightest X-ray point sources in M82

The X-ray properties of the 8 brightest X-ray sources in M82 are presented in Chapter 4. The data from the deep ($\sim$ 480 ks) *Chandra* observation of M82 allows us to resolve its complicated nucleus, and so to investigate short-term and long-term variability, as well as long-term spectral variations in the population of luminous resolved point-like sources. Our results indicate that most sources in our sample display variability on both short and long timescales, with one of the sources being

identified as a transient candidate. The observed spectral and timing properties of a second source indicate the possibility of the source being a luminous accreting NS. We also find that the 5 objects with luminosities below 10^{39} erg s^{-1} display a possible correlation between flux and change in spectral shape, suggesting the possibility of an accretion state change from the canonical TD state to the SPL state. The spectral shapes of the 3 brightest sources in our sample, ULXs including M82 X-1 and X42.3+59, are seen to be similar to those that have been reported in previous work. High levels of short and long-term variability are seen in these 3 sources. In particular, X42.3+59 displays the highest level of long-term variation in flux, with a relatively quiescent flux level throughout the majority of the *Chandra* observations, and a sudden increase in brightness to ULX luminosities between the final 2 observations.

5.2 Future work

5.2.1 Optically undetected AGN

Although the results presented in Chapter 2 give a clear indication that galaxies with extremely high X-ray luminosities are powered by AGN, it would be useful to clarify this result with a study of a larger sample of high X-ray luminosity galaxies that display no clear signs of AGN activity in the optical band. It is possible to expand the sample of such known sources by applying a method similar to that which we used in the selection of the sources in our sample, i.e., by referring to newer archival X-ray and optical data such as later releases of the 2XMM and *SDSS* catalogues. Another possibility is to search for more examples of these sources by cross-correlating data from observations in different wavelengths to optical data. For example, the identification of AGN activity is possible via the detection of hidden broad lines in the IR spectra of sources. Data from future X-ray observations may also be used in the identification of these galaxies. With an unprecedented collecting area and spectral capabilities, it will be possible to use data obtained by *Athena*[1]

[1]For more information on *Athena*, see `sci.esa.int/ixo/`.

observations to identify sources that display optical spectra with no obvious AGN signatures, but that display clear X-ray signatures of AGN activity.

The results of our work have clearly indicated the importance of wide field surveys in the identification of optically undetected AGN. Future studies of these objects will greatly benefit from new wide-field surveys such as the *eRosita* all sky X-ray survey[2], as they will provide an excellent resource for the identification of these galaxies.

5.2.2 ULXs in low metallicity environments

There is growing observational and theoretical evidence to suggest that ULXs form preferentially in low metallicity environments (e.g., Swartz et al. 2009). As part of a larger study, an ongoing *Chandra* and *HST* survey of 27 nearby (< 30Mpc) Extremely Metal Poor Galaxies (XMPG) is being undertaken. These galaxies are the most metal-deficient galaxies known, and a logical place to find ULXs if they favour metal-poor systems.

Using data from this survey, we aim to test recent population synthesis models which predict that ULXs should be very numerous in metal-poor galaxies (e.g., Belczynski et al. 2008). We also aim to test the hypothesis that ULXs form in massive young star clusters. To achieve these aims, we will obtain a list of candidate star clusters close to/coincident with the X-ray sources within the galaxies, and constrain the ages of these clusters. It is likely for optical identification of star clusters to be hindered by high levels of extinction typically observed in active star forming galaxies. This issue can be overcome by IR observations of these galaxies. However, the identification of point-like sources such as star clusters typically requires higher spatial resolution than that which is afforded by present IR missions. The spatial resolution capabilities of the *James Webb Telescope*[3], which will exceed those of past and present IR missions, will be of great benefit to studies such as this in the future.

[2]For more information on *eRosita*, see `http://www.mpe.mpg.de/erosita/`.
[3]For more information on the *James Webb Telescope*, see `http://www.jwst.nasa.gov/`.

5.2.3 Population studies of the brightest point-like X-ray sources in local galaxies

Our study of the brightest X-ray point source population of M82 has demonstrated the large range of results that can be yielded from studies dedicated to the properties of galaxies that are rich in bright XRB populations. Similar studies of XRBs with luminosities in the 10^{38} – 10^{39} erg s^{-1} range can be undertaken in the future, by obtaining data of local galaxies (at a distance of $\sim$ 5 – 10 Mpc) either from the *Chandra* Data Archive, or from new observations taken by *Chandra*. Data obtained by *Chandra* is particularly beneficial to the study of X-ray point sources, since the high spatial resolution of the instruments on board the observatory allows for individual sources to be resolved. However, in order to obtain a number of photon counts large enough to perform high quality spectral and timing analysis of sources at these distances, each observation taken by *Chandra* must have exposure times of the order $\sim$ 100 ks. Alternatively, data from *XMM-Newton* observations can be used in such studies. The higher photon collecting area of the instruments on board *XMM-Newton* requires less observational exposure time, although the lower spatial resolution can cause confusion issues in the identification of individual point sources. In the future, studies of X-ray point sources will be able to take advantage of the unprecedentedly high collecting area and spectral capabilities of the instruments on board *Athena*. Although the anticipated spatial resolution of *Athena* is similar to that of *XMM-Newton*, the large increase in collecting area over previous missions (e.g., $\geq$ 5 times larger than *XMM-Newton*) will allow for unprecedentedly high quality analyses of X-ray point sources in nearby galaxies.

5.3 Concluding remarks

In this chapter, we have presented a summary of the major results of the work in this thesis. We have also suggested a number of possible studies that can build upon this work, using data from observations taken by telescopes that are both currently active, and that will be active in the foreseeable future. Studies such as these will build on the current work in this exciting and growing field of astronomy, of which

this thesis is just a small part, and in doing so will greatly expand our understanding of the properties and astrophysics of X-ray point sources located within active star forming galaxies.

Bibliography

[1] Adams T. F. 1977, ApJS, 33, 19

[2] Aitken D. K., Roche P. F., Allen M. C. 1982, MNRAS, 199, 31

[3] Alexander D. M., Bauer F. E., Chapman S. C., Smail I., Blain A. W., Brand, W. N., Iviso R. J. 2005, ApJ, 632, 736

[4] Alexander D. M., et al. 2003, AJ, 126, 539

[5] Antonucci R. 1993, ARA&A, 31, 473

[6] Antonucci R. R. J., Miller J. S. 1985, ApJ, 297, 621

[7] Appleton P. N. 1999, IAUS, 186, 97

[8] Appleton P. N., Marston A. P. 1997, AJ, 113, 201

[9] Arnaud K. A. 1996, Astronomical Data Analysis Software and Systems V, eds. Jacoby G. and Barnes J., p17, ASP Conf. Series volume 101

[10] Arnaud K. A., Brandaurdi-Raymont G., Culhane J. L., Fabian A. C., Hazard c., McGlynn T. A., Shafer R. A., Tennant A. F., Ward M. J. 1985, MNRAS, 217, 105

[11] Arp H. 1966, ApJS, 14, 1

[12] Athanassoula E. 1992, MNRAS, 259, 345

[13] Athanassoula E. 1994, in: 'Mass-Transfer Induced Activity in Galaxies', ed. Shlosman I., Cambridge University Press, Cambridge, p. 143

[14] Athanassoula E., Peurari I., Bosam A. 1997, MNRAS, 286, 284

[15] Awaki H., Koyama K., Inoue H., Halpern J. 1991, PASJ, 43, 195

[16] Balbus S. A. 2005, ASPC, 330, 185

[17] Baldwin J. A. 1977, ApJ, 214, 679

[18] Baldwin J. A., Philips M. M., Terlevich R. 1981, PASP, 93, 5

[19] Baldwin J. A., Wampler E. J., Gaskell C. M. 1989, ApJ, 338, 630

[20] Barger A. J. 2003, AIPC, 666, 205

[21] Barger A. J., Cowie L. L., Brandt W. N., Capak P., Garmier G. P., Hornschemeier A. E., Steffan A. T., Wehner E. H. 2002, AJ, 124, 1839

[22] Barnes J. E., Hernquist L. E. 1991, ApJ, 370, L65

[23] Barnes J. E., Hernquist L. E. 1992, ARA&A, 30, 705

[24] Bauer F. E., et al. 2004, AdSpR, 34, 2555

[25] Begelman M. C. 1985, in: 'Astrophysics of Active Galaxies and Quasars', ed. Miller J. S., University Science Books, Mill Valley, p. 41

[26] Begelman M. C. 2002, ApJ, 568, 97

[27] Begelman M. C., King A. R., Pringle J. E. 2006, MNRAS, 370, 399

[28] Belczynski K., Kalogera V., Rasio F. A., Taam R. E., Zezas A., Bulik T., Maccarone T. J., Ivanova N. 2008, ApJS, 174, 223

[29] Belczynski K., Sadowski A. Rasio F. A. 2004, ApJ, 611, 1068

[30] Belloni T. M., Homan J., Casella P., van der Klis M., Nespoli E., Lewin W. H. G., Miller J. M., Méndez M. 2005, A&A, 440, 207

[31] Bellovary J. M., Governato F., Quinn T. R., Wadsley J., Shen S., Volonteri M. 2010, ApJ, 721, 148

[32] Berghea C. T., Weaver K. A., Colbert E. J. M., Roberts T. P. 2008, ApJ, 687, 471

[33] Blandford R. D. 1985, in: 'Active Galactic Nuclei', ed. Dyson J. E., Manchester University Press, p. 281

[34] Block D. L., Puerari I., Takamiya M., Abraham R., Stockton A., Robson I., Holland W. 2001, A&A, 371, 393

[35] Blustin A. J., Page M. J., Fuerst S. V., Branduardi-Raymont G., Ashton C. E. 2005, A&A, 431, 111

[36] Bondi H. 1952, MNRAS, 112, 195

[37] Bradt H., Levine A. M., Remillard R. A., Smith D. A. 2000, in: 'Multifrequency Behavious of High Energy Cosmic Sources', eds. Giovannelli F. and Sabau-Graziati L.,astro-ph/0001460

[38] Brandt W. N. Hasinger G. 2005, ARA&A, 43, 827

[39] Bregman J. N., Schulman E., Tomasaki K. 1995, ApJ, 439, 155

[40] Bressan A., Silvia L., Granato G. L. 2002, A&A, 392, 377

[41] Bruzual G., Charlot S. 2003, MNRAS, 344, 1000

[42] Burbidge E. M., Burbidge G. R., Rubin V. C. 1964, ApJ, 140, 942

[43] Burbidge G., Hewitt A. 1992, in: 'Variability of Blazars', eds. Valtaoja E. and Valtonen M., Cambridge University Press, Cambridge, p. 4

[44] Burbudge E. M., Burbidge G. R. 1959, ApJ, 130, 12

[45] Caccianiga A., Severgnini P., Della Ceca R., Maccacaro T., Carrera F. J., Page M. 2007, A&A, 470, 557

[46] Cappi M., et al. 1999, A&A, 350, 777

[47] Cash W. 1979, ApJ, 228, 939

[48] Chiang Y. -K., Kong A. K. H. 2011 MNRAS, 414, 1329

[49] Christopher M. H., Scoville N. Z., Armus L. 2004, ASPC, 322, 209

[50] Ciliegi P., Elvis M., Wilkes B. J., Boyle B. J., McMahon R.G. 1997, MNRAS, 284, 401

[51] Code A. D., et al. 1993, ApJ, 403, 63

[52] Colbert E. J. M., Heckman T. M., Ptak A. F., Strickland D. K., Weaver K. A. ApJ, 602, 231

[53] Colbert E. J. M., Mushotzky R. F. 1999, ApJ, 519, 89

[54] Colless M., et al. 2001, MNRAS, 328, 1039

[55] Collura A., Reale F., Schulman E., Bregman J. N. 1994, ApJ, 420, 63

[56] Comastri A., et al. 2002, ApJ, 571, 771

[57] Combes E., Elmegreen B. G. 1993, A&A, 271, 391

[58] Combes F. 1991, 'Dynamics of Galaxies and their Molecular Cloud Distribution, IAU Symposium', eds. Combes F. and Casoli F., p. 146

[59] Combes F., Gerin M. 1985, A&A, 150, 327

[60] Conti P. S. 1991, ApJ, 377, 115

[61] Cottrell G. A. 1977, MNRAS, 178, 577

[62] Danks A. C., Materne J. 1984, A&A, 139, 455

[63] Davis J. E. 2001, ApJ, 562, 575

[64] Davis S. W., Narayan R., Zhu Y., Barret D., Farrell S. A., Godet O., Servillat M., Webb N. A. 2011, ApJ, 734, 111

[65] Dewangan G. C., Titarchuck L., Griffiths R. E. 2006, ApJ, 637, 21

[66] de Vaucouleurs G., de Vaucouleurs A. 1964 ApJ, 140, 1622

[67] de Wit W. J., Testi L., Palla F., Zinnecker H. 2005, A&A, 437, 247

[68] Dickey J. M., Lockman F. J. 1990, ARA&A, 28, 215

[69] Dolphin A. E. 2000, PASP, 112, 1397

[70] Done C. 2002, RSPTA, 360, 1967

[71] Done C., Gierlinski M., Kubota A. 2007, A&Rv, 15, 1

[72] Done C., Gierlinski M. 2003, MNRAS, 342, 1041

[73] Done C., Kubota A. 2006, MNARS, 371, 1216

[74] Dyson F. W. 1893, RSPTA, 184, 43

[75] Eckart M. E., Stern D., Helfand D. J., Harrison F. A., Mao P. H., Yost S. H. 2006, ApJS, 165, 19

[76] Edge D. O., Shakeshaft J. R., McAdam W. B., Baldwin J. E., Archer S. 1959, MmRAS, 68, 37

[77] Ehman J. R., Dixon R. S., Kraus J. D. 1970, AJ, 75, 351

[78] Ekers J. A. 1969, AJPA, 7, 3

[79] Elmegreen B. G. 1994a, in: 'Violent Star Formation: From 30 Doradus to QSOs, Proceedings of the First IAC-RGO Meeting', ed. Tenorio-Tagle G., Cambridge University Press, Cambridge, p. 220

[80] Elmegreen B. G. 1990, ASPC, 12, 247

[81] Elvis M., Civano F., Vignali C., et al. 2009, ApJS, 184, 158

[82] Elvis M., Maccacaro T., Wilson A. S., Ward M. J., Penton M. V., Fosbury R. A. E., Perola G. C. 1978, MNRAS, 183, 129

[83] Esin A. A., McClintock J. E., Drake J. J., Garcia M. R., Haswell C. A., Hynes R. I, Muno M. P. 2001, ApJ, 555, 483

[84] Esin A. A., McClintock J. E., Narayan R. 1997, apJ, 489, 865

[85] Fabbiano G. 1988, ApJ, 330, 672

[86] Fabbiano G. 2006, ARA&A, 44, 323

[87] Fabbiano G., Baldi A., King A. R., Panman T. J., Raymodn J., Read A., Rots A., Schweizer F., Zezas A . 2004, ApJ, 605, 21

[88] Fabbiano G., Heckman T. M., Keel W. C. 1990, ApJ, 335, 442

[89] Fabbiano G., White E. 2006. in: 'Compact Stellar X-ray Sources', eds. Lewin W. H. G. and van der Klis M., Cambridge University Press, Cambridge, p. 475

[90] Fabbiano G., Zezas A., Murray S. S. 2001, ApJ, 554, 1035

[91] Fabrika S., Mescheryakov A. 2001, in: 'IAU Symposium, Vol. 205, Galaxies and their Constituents at the Highest Angular Resolutions', ed. Schilizzi R. T., p. 268

[92] Fall S. M., Chandar R., Whitmore B. C. 2005, ApJ, 631, 133

[93] Fanaroff B. L., Riley J. M. 1974, MNRAS, 167, 31

[94] Farrell S. A., Webb N. A., Barret D., Godet O., Rodrigues J. M. 2009, Nature, 460, 73

[95] Fender R. 2006, in: 'Compact Stellar X-ray Sources', eds. Lewin W. H. G. and van der Klis M., Cambridge University Press, Cambridge, p. 381

[96] Fender R. P., Belloni T. M., Gallo E. 2004, MNRAS, 355, 1105

[97] Fenech D., Beswick R., Muxlow T. W. B., Pedlar A., Argo M. K. 2010, MNRAS, 408, 607

[98] Feng H., Kaaret P. 2007, ApJ, 668, 941

[99] Feng H., Kaaret P. 2010, ApJ, 712, 169

[100] Feng H., Rao F., Kaaret P. 2010, ApJ, 710, 137

[101] Feng H., Soria R. 2011, NewAR, 55, 166

[102] Feng Y., Taam R. E., Misra R., Wu X. -B., Xue Y. 2007, ApJ, 658, 287

[103] Feng, H., Rao F., Kaaret P. 2010, ApJ, 710, 137

[104] Ferland G. J., Peterson B. M., Horne K., Welsh W. F., Nahar S. N. 1992, apJ, 387, 95

[105] Few J. A M., Madore B. F. 1986, MNRAS, 222, 673

[106] Filipenko A. V. 1992, in: 'Relationships Between Active Galactic Nuclei and Starburst Galaxies', ed. Filipenko A. V., Astronomical Society of the Pacific, San Francisco, p. 253

[107] Fiorito R., Titarchuck L. 2004, ApJ, 614, 113

[108] Fitzpatrick E. L. 1999, PASP, 111, 63

[109] Fosbury R. A. E., Hawarden T. G. 1977, MNRAS, 178, 473

[110] Franceschini A., et al. 2003, MNRAS, 343, 1181

[111] Freeman K. C., de Vaucouleurs G. 1976, ApJ, 194, 569

[112] Galloway D., Psaltis D., Chakrabarty D., Muno M. 2003, ApJ, 590, 999

[113] Gao Y., Wang Q. D., Appleton p. N., Lucas R. A. 2003, ApJ, 596, 171

[114] Gerin M., Combes E., Athanassoula E. 1990, A&A, 239, 37

[115] Ghisellini G., Haardt F., Matt G. 1994, MNRAS, 267, 743

[116] Ghosh P., Lamb F. K. 1991, 1979, ApJ, 234, 296

[117] Giacconi R., Gursky H. Paolini F. R., Rossi B. B. 1962, PRL, 9, 439

[118] Giacconi R., et al. 2001, ApJ, 551, 624

[119] Gierlinski M., Done C. 2002, MNRAS, 349, 7

[120] Gierlinski M., Zdziarski A. A., Poutanen J., Coppi P. S., Ebisawa K., Johnson W. N. 1999, MNRAS, 309, 496

[121] Gierliński M. Done C. 2004, MNRAS, 349, 7

[122] Gladstone J. C., Roberts T. P. 2009, MNRAS, 397, 124

[123] Gladstone J. C., Roberts T. P., Done C. 2009, MNRAS, 397, 1836

[124] Gladstone J., Done C., Gierlinski M. 2007, MNRAS, 378, 13

[125] Goodrich R. W., Veilleux S., Hill G. J. 1994, ApJ, 422, 521

[126] Goulding A. D., Alexander D. M. 2009, ASPC, 408, 59

[127] Goulding A. D., Alexander D. M. 2009, MNRAS, 398, 1165

[128] Greiner J., Cuby J. G., McCaughrean, M. J. 2001, Nature, 414, 522

[129] Griffiths R. E., Ptak A., Feigelson E. D., Garmire G., Townsley L., Brandt W. N., Sambruna R., Bregman J. N. 2000, Sci, 290, 1325

[130] Grimm H. -J., Gilfanov M., Sunyaev R. 2002, A&A, 391, 923

[131] Grimm H. -J., Gilfanov M., Sunyaev R. 2003, MNRAS, 339, 793

[132] Grisé F., Kaaret P., Feng H., Kajava J. J. E., Farrell S. A. 2010, ApJ, 724, 148

[133] Gultekin K., et al. 2009, ApJ, 698, 198

[134] Haardt F., Maraschi L. 1993, ApJ, 413, 507

[135] Hameury J. -M., Lasota J. -P., McClintock J. E., Narayan R. 2007, ApJ, 489, 234

[136] Hannikainen D., Campbell-Wilson D., Hunstead R., McIntyre V., Lovell J., Reynolds J., Tzioumis T., Wu K. 2001, ApSSS, 276, 45

[137] Harper D. A., Low F. J., 1973, ApJ, 182, 89

[138] Harwit M., Pancini F. 1975, ApJ, 200, 127

[139] Hasinger G., van der Klis M. 1989, A&A, 225, 79

[140] Hazard C., Gulkis S., Bray A. D. 1967, ApJ, 148, 669

[141] Heckman T. M. 1980, A&A, 87, 152

[142] Heckman T. M. 1987, in 'Observational Evidence of Activity in Glaxies', eds. Khachikian E. Y., Fricke K. J., Melnick J., Reidel, Dordrecht, p. 421

[143] Heckman T. M., Armus L., Miley G. K.

[144] Heil L. M., Vaughan S., Roberts T. P. 2009, MNRAS, 397, 1061

[145] Hickox R. C., Markevitch M. 2006, ApJ, 645, 95

[146] Hirano A., Kitamoto S., Yamada T., Mineshige S., Fukue, J. 1995, ApJ, 446, 350

[147] Holtzman J. A., Burrows C. J., Casertano S., Hester J. J., Trauger J. T., Watson A. M., Worthey G. 1995, PASP, 107, 1065

[148] Hong J., Grindlay J., Schlegel E., Grindlay J. E.. 2004, ApJ, 614, 508

[149] Hornschemeier A. E., Heckman T. M., Ptak A. F., Tremonti C. A., Colbert E. J. M. 2005, AJ, 129, 86

[150] Hornschemeier A. E., et al. 2001, ApJ, 554, 742

[151] Hoyle F., Lyttleton R. A. 1941, MNRAS 101,27

[152] Huang S. -N., Steward P. 1988, A&A, 197, 14

[153] Ichimaru S. 1977, ApJ, 214, 840

[154] Immler S., Lewin, W. H. G. 2003, in: 'Lecture Notes in Physics, Berlin Springer Verlag, Vol. 598, Supernovae and Gamma-Ray Bursters', ed. Weiler K., p. 91

[155] Iwasawa K., Koyama K,. Awaki H., Kunieda H., Makishima K., Tsuru T., Ohashi T., Nakai N. 1993, ApJ, 409, 155

[156] Jannuzi B. T., Elston R., Schmidt G. D., Smith P. S., Stockman H. S. 1994, ApJ, 429, 49

[157] Jansen et al. 2001, A&A, 365, 1

[158] Jenkins L. P., Roberts T. P., Ward M. J., Zezas A. 2004, MNRAS, 352, 1335

[159] Jia J., Ptak A., Heckamn T. M., Overzier R. A., Hornschemeier A., LaMassa S. M. 2011, ApJ, 731, 55

[160] Jin J., Feng H., Kaaret P. 2010, ApJ, 716, 181

[161] Körding E., Falcke H. Markoff S. 2002, A&A, 382, 13

[162] Kaaret P., Alonso-Herrero A., Gallagher J., S., Fabbiano G., Zezas A. 2004, MNRAS, 348, 28

[163] Kaaret P., Corbel S., Prestwich A. H., Zezas A. 2003, Science, 299, 365

[164] Kaaret P., Feng H. 2007, ApJ, 669, 106

[165] Kaaret P., Feng H., Gorski M. 2009, ApJ, 692, 653

[166] Kaaret P., Prestwich A. H., Zezas A., Murray S. S., Kim D. -W., Kilgard R. E., Schlegel E. M., Ward M. J. 2001, MNRAS, 321, 29

[167] Kaaret P., Simet M. G., Lang C. C. 2006, ApJ, 646, 174

[168] Kaaret P., Simet M. G., Lang C. C. 2006, Sci, 311, 491

[169] Kaastra J. S. 1992, An X-Ray Spectral Code for Optically Thin Plasmas (Internal SRON-Leiden Report, updated version 2.0)

[170] Kato M. 1983, PASJ, 35, 33

[171] Kato S., Fukue J., Mineshige S. 1998, 'Black-hole accretion disks', Kyoto University Press, Kyoto

[172] Kauffmann G., et al. 2003, MNRAS, 346, 1055

[173] Kawaguchi T. 2003, ASPC, 290, 103

[174] Kewley L. J., Dopita M. A., Sutherland R. S., Heisler C. A., Trevema J. 2001, ApJ, 556, 121

[175] Khachikan E. Y., Weedman D. W. 1974, ApJ, 192, 581

[176] Kim D. -W., Fabbiano G. 2003, ApJ, 586, 826

[177] Kim D. -W., Fabbiano G. 2003, ApJ, 846, 857

[178] Kim M., et al. 2007, ApJS, 169, 401

[179] King A. R. 2009, MNRAS, 393, 41

[180] King A. R., Dehnen W. 2005, MNRAS, 357, 275

[181] King A. R. 2004, MNRAS, 347, 18

[182] Kong A. K. H., Yang Y. J., Hsieh P. -Y., Mak D. S. Y., Pun C. S. J. 2007, ApJ, 671, 349

[183] Kong A. K. H., Yang Y. J., Yen T. -C., Feng H., Kaaret P. 2010, ApJ, 722, 1816

[184] Kotilainen J. K., Moorwood A. F. M., Ward M. J., Forbes D. A. 1996, A&A, 313, 771

[185] Krolik J. H., Madau P., Życki P. T. 1994, ApJ, 420, 57

[186] Kronberg P. P., Biermann P. 1983, IAUS, 101, 583

[187] Kronberg P. P., Biermann P., Schwab F. R. 1985, ApJ, 291, 639

[188] Kubota A., Ebisawa K., Makishima K., Nakazawa K. 2005, ApJ, 631, 1062

[189] Kubota A., Makishima K. 2004, ApJ, 601, 428

[190] Kuulkers E., den Hartog P. R., in't Zand J. J. M., Verbunt F. W. M., Harris W. E., Cocchi M. 2003, A&A, 399, 663

[191] Kwan J. 1979, ApJ, 229, 567

[192] Lasota J. -P. 2001, NewAR, 45, 449

[193] Lawrence A. 1991, MNRAS, 252, 586

[194] Lawrence A., Watson M. G., Pounds K. A., Elvis M. 1987, Nature, 325, 694

[195] Lehmer B. D., et al. 2005, ApJS, 161, 21

[196] Lehmer B. D., et al. 2008. ApJ, 681, 1163

[197] Lehnert M. D., Heckman T. M., Weaver K. A. 1999, ApJ, 523, 575

[198] Leitherer C., Heckman T. M. 1995, ApJS, 96, 9

[199] Lester D. F. 1995, ASPC, 73, 159

[200] Lester D. F., Carr J., Marshall J., Gaffney N. 1990, NASCP, 3084, 340

[201] Lewin W. H. G., van Paradijs J., Taam R. 1996, in: 'X-ray Binaries', eds. Lewin W. H. G., van Paradijs J., and ven den Heuvel E. P. J., Cambridge University Press, Cambridge

[202] Linden T., Kalogera V., Sepinsky J. F., Prestwich A., Zezas A., Gallagher J. S. 2010, ApJ, 725, 1984

[203] Lira P., Ward M. J., Zezas A., Alonso-Herrero A., Ueno, S. 2002, MNRAS, 330, 259

[204] Liu Q. Z., Mirabel I. F. 2005, A&A, 429, 1125

[205] Liu Q. Z., van Paradijs J., van den Heuvel E. P. J. 2000, A&AS, 147, 25

[206] Lumb D. H., Warwick R. S., Page M., De Luca A. 2002, A&A, 398, 93

[207] Lynds C. R., Sandage A. R. 1963, AJ, 68, 284

[208] Lynds R., Toomre A. 1976, ApJ, 209, 328

[209] Méndez M., van der Klis M. 1997, ApJ, 479, 926

[210] Maccarone T. J., Coppi P. S. 2003, MNRAS, 338, 189

[211] Madau P., Rees M. J. 2001, ApJ, 551, L27

[212] Madhusudhan N., Justham S., Nelson L., Paxton B., Pfahl E., Podsiadlowski P., Rappaport S. 2006, ApJ, 640, 918

[213] Maiolino R., et al. 2003, MNRAS, 344, 59

[214] Makishima K., et al. 2000, ApJ, 535, 632

[215] Mapelli M., Moore B. Giordano L., Mayer L., Colpi M., Ripamonti E., Callegari S. 2008, MNRAS, 383, 230

[216] Marconi A., Oliva E., van der Werf P. P., Maiolino R., Schreier E. J., Macchetto F., Moorwood A. F. M. 2000, A&A, 357,24

[217] Markoff S., Falcke H., Fender R. 2001, A&A, 372, 25

[218] Markowitz A., et al. 2003, ApJ, 593, 96

[219] Marston A. P., Appleton P. N. 1995, AJ, 109, 1002

[220] Matsumoto H., Tsuru T. G., Koyama K., Awaki H., Canizares C. R., Kawai N., Matsushita S., Kawabe R. 2001, ApJ, 547, 25

[221] McClintock J. E., Remillard R. E. 2006, in: 'Compact Stellar X-ray Sources', eds. Lewin W. H. G. and van der Klis M., Cambridge University Press, Cambridge, p. 157

[222] McHardy I. 1988, MmSAI, 59, 239

[223] McLeod K. K., Rieke G. H., Rieke M. J., Kelly D. M. 1993, ApJ, 412, 111

[224] McSwain M. V., Ransom S. M., Boyajian T. S., Grundstrom E. D., Roberts M. S. E. 2007, ApJ, 660, 740

[225] Melo V. P., Muñoz-Tuñón C., Maíz-Apellániz J., Tenorio-Tagle G. 2005, ApJ, 619, 270

[226] Mestel L. 1954, MNRAS, 114, 437

[227] Meurer G. R., Heckman T. M., Leitherer C., Kinney A., Robert C., Garnett D. R. 1995, ApJ, 110, 2665

[228] Mewe R., Gronenschild E. H. B. M., van den Oord G. H. J. 1985, A&AS, 62, 197

[229] Mewe R., Lemen J. R., van den Oord G. H. J. 1986, A&AS, 65, 551M

[230] Middleton M. J., Sutton A. D., Roberts T. P. 2011b, MNRAS, 1209

[231] Miller J. M., Fabian A. C., Miller M. C. 2004, ApJ, 614, L117

[232] Miller J.M., Fabbiano G., Miller M. C., Fabian A. C. 2003, ApJ, 585, 37

[233] Miller M. C., Colbert E. J. M. 2004, IJMPD, 13, 1

[234] Mineshige S., Hirano A., Kitamoto S., Yamada T. T., Fukue J. 1994, ApJ, 426, 308

[235] Miyamoto S., Iga S., Kitamoto S., Kamodo Y. 1993, ApJ, 403, 39

[236] Miyamoto S., Kitamoto S. 1991, ApJ, 374, 741

[237] Miyawaki R., Makishima K., Yamada S., Gandhi P., Mizuno T., Kubota A., Tsuru T. G., Matsumoto H. 2009, PASJ, 61, 263

[238] Moorwood A. 1996, SSR, 77, 303

[239] Moorwood A. E. M., and Oliva E. 1994a, ApJ, 429, 602

[240] Moran E. C., Filippenko A. V., Chornock R. 2002, ApJ, 579, 71

[241] Moran E. C., Halpern J. P., Helfand D.J. 1996, ApJS, 106, 341

[242] Moran E. C., Lehnert M. D., Helfand D. J, 1999, ApJ, 526, 649

[243] Moretti A., Campana S., Lazzati D., Tagliaferri G. 2003, ApJ, 588, 696

[244] Mucciarelli P., Casella P., Belloni T., Zampieri L., Ranalli P. 2006, MNRAS, 365, 1123

[245] Mulchaey J. S., Davis D. S., Mushotzky R. F., Burstein D. 2003, ApJS, 145, 39

[246] Mushotzky R. F., Cowie L. L., Barger A. J., Arnaud K. A. 2000, Nature, 404, 459

[247] Nandra K., Pounds K.A. 1994, MNRAS, 268, 405

[248] Narayan R., Garcia M. R., McClintock J. E. 1997, ApJ, 478, 79

[249] Narayan R., McClintock J. E., Yi I. Y. 1996 ApJ, 457, 821

[250] Narayan R., Yi I. 1995, ApJ, 452, 710

[251] Narayan R., Yi I. 1994, ApJ, 428, 13

[252] Nicastro F. 2000, ApJ, 530, 65

[253] Nobili L., Turrola R., Lapidus I. 1994, ApJ, 433, 276

[254] O'Connell R. W., Mangano J. J. 1978, ApJ, 221, 620

[255] Okajima T., Ebisawa K., Kawaguchi T. 2006, ApJ, 652, 105

[256] Oliva E., Origlia L., Kotilainen J. K., Moorwood A. M. F. 1995, A&A, 301, 55

[257] Osterbrock D. E. 1981, ApJ, 249, 462

[258] Owen R. A., Warwick R. S. 2009, MNRAS, 394, 1741

[259] Pérez Garcia A. M., Rodríguez Espinosa J. M., Santolaya Rey A. E. 1998, ApJ, 500, 685

[260] Patterson J. 1981, Nature, 292, 810

[261] Pedlar A., Wills K. A., Cole G. H. J., Muxlow T. W. B., Mundell C. G., Gallimore, J. F. 1999, ASPC, 156, 252

[262] Penston M. V., Pérez 1984, MNRAS, 211, 33

[263] Perna R., Soria R., Pooley D., Stella L. 2008, MNRAS, 384, 1638

[264] Peterson B. M. 1996, 'Active Galactic Nuclei', Cambridge University Press, Cambridge

[265] Peterson B. M., et al. 2000, ApJ, 542, 121

[266] Phillips M. M., Edmunds M. G., Pagel B. E., Turtle A. J. 1983, MNRAS, 203, 759

[267] Pietsch P. 1993, in: 'Physics of Nearby Galaxies: Nature or Nurture?', eds. Thuan T. X, Balkowski c., and Van J. T. T., Editions Frontières, p. 67

[268] Pietsch W. N., et al. 2001, A&A, 365, 174

[269] Portegies Zwart S. F., Baumgardt H., Hut P., Makino J., McMillan S. L. W. 2004, Nature, 428, 724

[270] Poutanen J., Lipunova G., Fabrika S., Butkevich A. G., Abolmasov P. 2007, MNRAS, 377, 1187

[271] Prestwich A. H., Irwin J. A., Kilgard R. E., Krauss M. I., Zexas A., Primini F., Kaaret P., Borson B. 2003, ApJ, 595, 719

[272] Prestwich A., Zezas A., Kaaret P., Murray S., Kilgard R., Kim D.-W., Shlegel E. 2001, IAUS, 205, 208

[273] Prestwich, A. H., Galache J. L., Linden T., Kalogera V., Zezas A., Roberts T. P., Kilgard R., Wolter A., Trinchieri G. 2012, ApJ, in press

[274] Psaltis D. 2006, in: 'Compact Stellar X-ray Sources', eds. Lewin W. H. G. and van der Klis M., Cambridge University Press, Cambridge, p. 1

[275] Ptak A., Griffiths R. 1999, ApJ, 517, 85

[276] Ptak A., Heckman T., Levenson N. A., Weaver K., Strickland D. 2003, ApJ, 592, 782

[277] Puerari I., Anguilar L. 2009, RevMexAA, 35, 237

[278] Quataert E., Narayan R. 1999 ApJ, 520, 298

[279] Ranalli P., Comastri A., Origlia L,. Maiolino R. 2008, MNRAS, 386, 1464

[280] Rangelov B., Prestwich A. H., Chandar R. 2011, ApJ, 741, 86

[281] Read A. M., Stevens I. R. 2002, MNRAS, 335, 36

[282] Reichert G. A., Mushotzky R. F., Petre R., Holt S. S. 1985, ApJ, 296, 69

[283] Remillard R. A., Muno M. P., McClintock J. E., Orosz J. A. 2002, ApJ, 580, 1030

[284] Reynolds C. S., Nowak M. A. 2003, PhR, 377, 389

[285] Rieke G. H., Leboefsky M. J., Thompson R. I., Low F. J., Tokunaga A. T. 1980, ApJ, 238, 24

[286] Rieke G. H., Loboefsky M. J. 1979, ARA&A, 17, 477

[287] Rieke G. H., Low F. J. 1975, ApJ, 197, 17

[288] Rigby J. R., Rieke G. H., Donley J. L., Alonso-Herrero A., Pérez-González P. G. 2006, ApJ, 645, 115

[289] Roberts T. P. 2007, Ap&SS, 311, 203

[290] Rowan-Robinson M. 1977, ApJ, 213, 635

[291] Sakai S., Madore B. F. 1999, ApJ, 526, 599

[292] Salpeter E. E. 1964, ApJ, 140, 796

[293] Sandage A. 1960, ApJ, 131, 610

[294] Sanders D. B., Soifer B. T., Elais J. H., Madore B. F., Matthews L., Neugebauer G., Scoville N. Z. 1988, ApJ, 325, 74

[295] Schlegel D. J., Finkbeiner D. P., Davis M. 1998, ApJ, 500, 525

[296] Schmidt M. 1969, in: 'Quasars and High-Energy Astronomy', eds. Douglas K. N., Robinson I., Schild A., Schucking E. L., Wheeler J. A., and Woolf N. J., Gordon and Breach, New York, p. 55

[297] Schmidt M., Green R. F. 1983, ApJ, 269, 352

[298] Scoville N., Young J. S. 1983, ApJ, 265, 148

[299] Seaquist E. R., Odegard N. 1991, IAUS, 144, 281

[300] Seyfert C. 1943, ApJ, 97, 28

[301] Shakura N. I., Sunyaev R. A. 1973, A&A, 24, 337

[302] Sharpio S. L., Lightman A. P., Eardley D. M. 1976, ApJ, 204, 187

[303] Shemmer O., Uttley P., Netzer H.,McHardy I. M., 2003, MNRAS, 343, 1341

[304] Shemmer O., et al. 2001, ApJ, 561, 162

[305] Shlosman I., Begelman M. C., Frank J. 1990, Nature, 345, 679

[306] Shrader C. R., Titarchuck L. 2003, ApJ, 598, 168

[307] Silverman J. D,. et al. 2010, ApJS, 191, 124

[308] Smith B. J. 1996, ASSL, 209, 170

[309] Smith R., Vaughan S. 2007, MNRAS, 375, 1479

[310] Sobolewsaki M. A., Papadakis I. E. 2009, MNRAS, 399, 1597

[311] Sobolewska M. A., Papadakis I. E. 2009, MNRAS, 399, 1597

[312] Soria R., Wu K. 2003, A&A, 410, 53

[313] Stobbart A. -M., Roberts T. P., Wilms J. 2006, MNRAS, 368, 397

[314] Stocke J. T., Wurtz R., Kuehr H. AJ, 102, 172

[315] Strickland D. K., Heckman T. M. 2007, ApJ, 658, 258

[316] Strauss M. A., Huchra J. P., Davis M., Yahil M., Fiisher K. B., Torny J. 1992, ApJS, 83, 29

[317] Strickland D. k., Heckman T. M. 2009, ApJ, 697, 2030

[318] Strohmayer T. D., Mushotzky R. F. 2003, ApJ, 586, 61

[319] Strohmayer T. E., Bildsten L. 2006 in: 'Compact Stellar X-ray Sources', eds. Lewin W. H. G. and van der Klis M., Cambridge University Press, Cambridge, p. 113

[320] Strohmayer T. E., Mushotzky R. F. 2003, ApJ, 586, 61

[321] Strohmayer T. E., Zhang, W., Swank J. H., Smale A., Titarchuck L., Day C., Lee U. 1996, ApJ, 469, 9

[322] Struck-Marcell C., Appleton P. N. 1987, ApJ, 323. 480

[323] Swartz D. A., Ghosh K. K., Tennant A. F., Wu K. 2004, ApJS, 154, 519

[324] Swartz D. A., Ghpsh K. K., Tennant A. F., Wu K. 2004, ApJ, 154, 519

[325] Swartz D., Tennant A. F., Soria R. 2009, ApJ, 703, 159

[326] Szokoly G. P., et al. 2004, ApJS, 155, 271

[327] Takahashi K., Inoue H., Dotani T. 2001, PASJ, 53, 1171

[328] Tanaka Y., Shibasaki N. 1996, ARA&A, 34, 607

[329] Tanaka Y., Lewin W. H. G. 1995, in: 'X-ray Binaries', eds. Lewin W. H. G., van Paradijs J., and ven den Heuvel E. P. J., Cambridge University Press,Cambridge, p. 126

[330] Tananbaum H., Gursky H., Kellogg E., Giacconi R., Jones C. 1972, ApJ, 177, 5

[331] Tauris T. M., van den Heuvel E. P. J. 2006, in: 'Compact Stellar X-ray Sources', eds. Lewin W. H. G. and van der Klis M., Cambridge University Press, Cambridge, p. 623

[332] Taylor R. D., Uttley P., McHardy I. M. 2003, MNRAS, 342, 31

[333] Telesco C. M., Dressel L. L., Wolstencroft R. D. 1993, ApJ, 414, 120

[334] Telesco C. M., Joy M., Dietz K., Decher R., Campins H. 1991, ApJ, 369, 135

[335] Theys J. C., Spiegel E. A. 1976, ApJ, 208, 650

[336] Theys J. C., Spiegel E. A. 1977, ApJ, 212, 616

[337] Tomisaka K., Ikeuchi S. 1988, ApJ, 330, 695

[338] Tomsick J. A., Kaaret P., Kroeger R. A., Remillard J. E. 1999, ApJ, 512, 892

[339] Treister E., Urry M. C., Lira P. 2005, ApJ, 630, 104

[340] Trouille M., Barger A. J., Cowie L. L., Yang Y., Mushotzky R. F. 2008, ApJS, 179, 1

[341] Trump J. R. et al. 2009, ApJ. 706, 797

[342] Trump J. R., et al. 2011, arXiv, 1103.0276

[343] Tsuru T. G., Awaki H., Koyama K., Ptak A. 1997, PASJ, 49, 619

[344] Tsuru et al. 2007, PASJ, 59, 269

[345] Turner T. J., Pounds K. A. 1989, MNRAS, 240, 833

[346] Urry M. C., Padovani P. 1995, PASP, 107, 803

[347] Uttley P., McHardy I. M. 2004, PthPS, 155, 170

[348] Uttley P., McHardy I. M., Vaughan S. 2005, MNRAS, 359, 345

[349] Vaiana G. S., Rosner R. 1978, ARA&A, 16, 393

[350] van Paradijs J., McClintock J. E. 1995, in: 'X-ray Binaries', eds. Lewin W. H. G., van Paradijs J., and ven den Heuvel E. P. J., Cambridge University Press, Cambridge, p. 58

[351] van Straaten S., van der Klis M., Wijnands R. 2005, ApJ, 619, 455

[352] van der Klis M. 1994, ApJS, 92, 511

[353] Vaughan S., Edelson R., Warwick R. S., Uttley, P. 2003, MNRAS, 345, 1271

[354] Vaughan S., Reeves J., Warwick R., Edelson R. 1999, MNRAS, 309, 113

[355] Vaughan S., Uttley P., Pounds K. A., Nandra N., Strohmayer T. E. 2011, MNRAS, 413, 2489

[356] Vignarca F., Migliari S., Belloni T., Psaltis D., van der Klis M. 2003, A&A, 397, 729

[357] Waller, W. H., Gurwell M., Tamura M. 1992, AJ, 104, 63

[358] Wang J. -M., Zhang E. -P. 2007, ApJ, 660, 1072

[359] Wang Z., Helou G., Lu N., COle D. 1995, ASPC, 73, 199

[360] Warwick R. S., Jenkins L. P., Read A. M., Roberts T. P., Owen R. A. 2007, MNRAS, 376, 1611

[361] Watson M. G., Stanger V., Griffiths R. E. 1984, ApJ, 286, 144

[362] Watson M. G., et al. 2009, A&A, 493, 339

[363] Weiss A., Walter F., Neininger N., Klein U. 1999, A&A, 345, 23

[364] Weisskopf M. C. 1999, AAS, 31, 1514

[365] Wilms J., Allen A., McCray R. 2000, ApJ, 254, 914

[366] Wolter A., Trinchieri G. 2004, A&A, 426, 787

[367] Wong et al. 2006, MNRAS, 370, 1607

[368] Worsley M. A., Fabian A. C., Alexander D. M., Bauer F. E., Brandt W. N., Hasinger G., Lehmer B. D. 2005, AIPC, 801, 51

[369] Xue Y. Q., et al. 2010, ApJ, 720, 368

[370] Yuan F., Narayan R. 2004, 612, 724

[371] Yuan F., Taam R. E., Misra R., Wu X. -B., Xue Y. 2007, ApJ, 658, 282

[372] Yun M. S., Ho P. T. P., Lo K. Y. 1994, Nature, 272, 530

[373] Zdziarski A. A., Grove J. E., Poutanen J., Rao A. R., Vasawale S. V. 2001, ApJ, 554, 45

[374] Zel'dovich Y. A., Novikov I. D. 1964, Sov. Phys. Dokl., 158, 911

[375] Zezas A., Alonso-Herrero A., Ward M. 2001, Ap&SS, 276, 601

[376] Zezas A., Fabbiano G., Baldi A. 2007, ApJ, 661, 135

[377] Zezas A., Fabbiano G., Rots A. H., Murray S. S. 2002, ApJ, 577, 710

[378] Zezas A., Fabbiano G., Prestwich A., Murray S., Ward M. J. 2001, ASPC, 249, 425